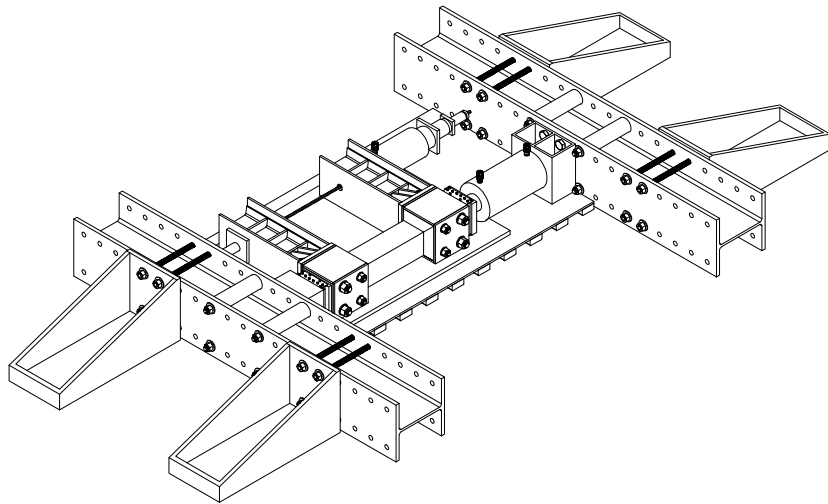




UNIVERSITY OF
ARKANSAS

College of Engineering
Civil Engineering

Stress-Strain Analysis of Belite Calcium Sulfoaluminate Cement Concrete for Structural Applications



Final Report

Gabriel Johnson, Graduate Student
Elizabeth Poblete, Ph.D. Student
Cameron Murray, Ph.D. PE, Principal Investigator

University of Arkansas, Fayetteville
Department of Civil Engineering
4183 Bell Engineering Center
Fayetteville, AR 72701

Project Sponsor:



Executive Summary

The current edition of the ACI 318-19(22) Building Code Requirements for Structural Concrete and Commentary allows the use of alternative cements in design when these materials can be proved to conform to the existing structural design parameters used to estimate performance. Belitic calcium sulfoaluminate (BCSA) cement is an alternative hydraulic cement which exhibits fast setting properties, high sulfate resistance, adequate durability, and low carbon emissions when compared with portland cement. Limited research exists to characterize the performance of BCSA cement concrete in ultimate strength design. This report compares the stress-strain relationship of BCSA cement concrete in both uniaxial compression and flexural compression loading to that of portland cement concrete. Also, guidance is provided on the applicability of current ACI code values for the design of BCSA cement concrete flexural members.

A total of 64 concrete cylinders at various water cement ratios (w/c) and ages were tested uniaxially and strains were measured to determine static modulus of elasticity (MOE). Of the 64 cylinders, 6 control cylinders of portland cement concrete (PC) and 58 BCSA cement concrete specimens were made. From these tests, uniaxial stress-strain relationships were developed, and MOE and maximum strain values occurring at maximum stress were compared with historical data and design code estimations.

14 unreinforced flexural compression specimens at various w/c and ages were fabricated and tested in combined axial compression and bending to evaluate compression zone properties of BCSA cement concrete for reinforced concrete design. Variables in this study included w/c, age at testing, and compressive strength. Results from flexural compression specimen testing were compared with historical results and design code estimates.

Results from uniaxial compression cylinder tests indicated that BCSA cement concrete behaves similarly to PC concrete in compression and has similar MOE and compression strain characteristics. Results from flexural compression specimens suggest that concrete design code equations for estimating design parameters for flexural members are adequate or conservative for BCSA cement concrete flexural members with strengths between 7.8 and 12.4 ksi.

Keywords: belitic calcium sulfoaluminate cement, rapid-setting cement, elastic modulus, uniaxial compression, flexural compression, stress-strain relationship, ultimate strain

Acknowledgements

The work presented in this report was conducted in the Harvell Civil Engineering Research and Education Center (CEREC) at the University of Arkansas. Support was provided by the American Concrete Institute's Foundation Concrete Research Council, under grant P0045. Concrete materials were generously provided by CTS Cement Manufacturing Corporation. This work would not have been feasible without the financial and expert support of these organizations.

Special thanks to Bette Poblete for her help and invaluable input in all aspects of lab work involved in this research. Thanks to Riley Dillard, Behzad Farivar, Andrès Calzacorta, Cai Rivers, Grady Caton, Shuyah Ouoba, and many others for their willingness to make concrete. This research would not have been possible without laboratory technicians David Peachee, Mark Kuss, and Daniel Davidson with their extensive manufacturing experience and lab knowledge. Thank you to the rest of the staff and faculty of the University of Arkansas civil engineering department.

Thank you to the principal investigator Dr. Cameron Murray for his substantial provisions in every aspect of this research. Thank you to Dr. Gary Prinz for his collaboration in this research regarding test setup and data analysis. Thanks to Dr Halit Mertol for the foundational basis for this research and assistance in calculating concrete stresses. Thank you to ACI committee 242 alternative cements and the chair of the committee, Dr. Mary Christiansen for their professional help and support throughout this project. Thanks to Dr. Christopher Ramseyer, Dr. Lisa Burris, Dr. Éric Bescher, Dr. Robert Thomas, and Mr. Ken Vallens for serving in an advisory role on this project. Finally, thanks to the ACI Foundation staff, particularly Ann Masek and Tricia Ladely.

Table of Contents

1	Introduction	1
1.1	General	1
1.2	Problem Statement	2
1.3	Research Objectives	3
1.4	Report Arrangement.....	3
2	Background and Previous Work.....	5
2.1	Materials.....	5
2.2	Digital Image Correlation.....	6
2.3	Uniaxial Compression in Concrete	7
2.3.1	Static Modulus of Elasticity	7
2.3.2	Maximum Uniaxial Compression Strain	9
2.4	Stress and Strain of Concrete Flexural Members.....	12
2.4.1	Strain and Stress Distribution	13
2.4.2	Concrete in Flexural Compression.....	17
2.4.3	Stress Distribution Estimation	21
3	Experimental Methodology.....	33
3.1	Materials.....	33
3.2	Uniaxial Compression Cylinders	36
3.3	Flexural Compression Specimens	40
3.3.1	Specimen Fabrication.....	40

3.3.2	Custom Equipment for Test Loading Setup.....	44
3.3.3	Test Setup.....	47
3.3.4	Testing method.....	52
3.3.5	Stress Calculations	53
4	Experimental Results and Discussion	57
4.1	Uniaxial Compression Cylinders	58
4.2	Flexural Compression Specimens	69
5	Conclusions and Recommendations.....	85
6	References	89
	Appendix A: Historical Data Tables.....	96
	Appendix B: Uniaxial Compression Cylinder Data.....	104
	Appendix C: Uniaxial Compression Cylinder Stress Analysis Code	110
	Appendix D: Flexural Compression Specimen Stress Analysis Code.....	114
	Appendix E: Fabrication Drawings	119

List of Figures

Figure 2.1 – MOE of BCSA cement concrete and code equations.....	9
Figure 2.2 – Lateral restraint in cylinders and cubes from platens.....	10
Figure 2.3 – Historical uniaxial compression strain at corresponding maximum stress for PC...	12
Figure 2.4 – Stage 1 and 2 strain and stress distribution diagram	14
Figure 2.5 – Stage 3 and 4 strain and stress distribution diagram	15
Figure 2.6 – ACI proposed strain and stress distribution in tension controlled flexural beams...	16
Figure 2.7 – Failure mechanisms of different concrete specimens.....	18
Figure 2.8 – Strain and stress distribution in specimen	20
Figure 2.9 – Strain and stress distribution diagram	23
Figure 2.10 – Ultimate strain of concrete flexural members	26
Figure 2.11 – Parameter k_1 values for concrete flexural members	27
Figure 2.12 – Parameter k_2 values for concrete flexural members	28
Figure 2.13 – Parameter k_3 values for concrete flexural members	29
Figure 2.14 – Product of parameters k_1 and k_3 or β_1 and α_1 for concrete flexural members.....	30
Figure 2.15 – Parameter α_1 for concrete flexural members	31
Figure 2.16 – Parameter β_1 for concrete flexural members.....	32
Figure 3.1 – Speckle pattern and density for 4in. diameter cylinders.....	36
Figure 3.2 – Speckle pattern and density for 6in. diameter cylinders.....	37
Figure 3.3 – DIC uniaxial strain camera setup	38
Figure 3.4 – Compressometer MOE method setup per ASTM C469.....	39
Figure 3.5 – Specimen nominal dimensions	42
Figure 3.6 – Wooden cross-section reducing formwork.....	42

Figure 3.7 – Foam insulation cross-section reducing formwork	43
Figure 3.8 – Upright formwork with bottom steel plate	43
Figure 3.9 – Concrete flexural compression specimen.....	44
Figure 3.10 – Moment arms for specimen.....	45
Figure 3.11 – Roller rotational offset.....	46
Figure 3.12 – Isometric view of flexure test setup.....	48
Figure 3.13 – Plan view of flexure test setup.....	49
Figure 3.14 – DIC camera setup for flexural compression specimens	51
Figure 3.15 – Speckle pattern and density for flexural compression specimen.....	52
Figure 3.16 – Loads on flexure specimen.....	56
Figure 4.1 – Compression strength development of BCSA cement mixtures over time.....	58
Figure 4.2 – Visualization of DIC strains in 4 in. diameter cylinder before and after failure	60
Figure 4.3 – Visualization of DIC strains in 6 in. diameter cylinder before and after failure	61
Figure 4.4 – Uniaxial compression strain 0.36 w/c BCSA cement concrete.....	62
Figure 4.5 – Uniaxial compression strain 0.42 w/c BCSA cement concrete.....	63
Figure 4.6 – Uniaxial compression strain 0.48 w/c BCSA cement concrete.....	63
Figure 4.7 – 7 day uniaxial compression stress-strain relationship of various w/c	64
Figure 4.8 – 28 day uniaxial compression stress-strain relationship of various w/c	65
Figure 4.9 – All MOE results.....	66
Figure 4.10 – MOE of BCSA cement concrete at various ages.....	67
Figure 4.11 – MOE of BCSA cement concrete at 28 days or above	68
Figure 4.12 – Uniaxial compression strain results.....	69
Figure 4.13 – Example of DIC strain gauge results prior to specimen failure	71

Figure 4.14 – Diagram of strain distribution in specimen before failure.....	72
Figure 4.15 – Failure modes of flexural compressive specimens.....	74
Figure 4.16 – Ultimate strain results ϵ_{cu}	76
Figure 4.17 – Parameter k_1 results.....	77
Figure 4.18 – Parameter k_2 results.....	78
Figure 4.19 – Parameter k_3 results.....	79
Figure 4.20 – Product of parameter k_1 and k_3 or α_1 and β_1 results.....	80
Figure 4.21 – Parameter α_1 results.....	81
Figure 4.22 – Parameter β_1 results.....	82
Figure 4.23 – Stress-strain relationship for 0.36 w/c BCSA flexural compressive specimens	83
Figure 4.24 – Stress-strain relationship for 0.42 w/c BCSA flexural compressive specimens	83
Figure 4.25 – Stress-strain relationship for 0.48 w/c BCSA flexural compressive specimens	84
Figure 4.26 – Stress-strain relationship for 0.42 w/c PC flexural compressive specimens.....	84
Figure 2.1 – Uniaxial compression strain 0.48 w/c 3 hour BCSA.....	104
Figure 2.2 – Uniaxial compression strain 0.48 w/c 1 day BCSA.....	104
Figure 2.3 – Uniaxial compression strain 0.48 w/c 3 day BCSA.....	104
Figure 2.4 – Uniaxial compression strain 0.48 w/c 7 day BCSA.....	104
Figure 2.5 – Uniaxial compression strain 0.48 w/c 28 day BCSA.....	104
Figure 2.6 – Uniaxial compression strain 0.48 w/c 6 month BCSA.....	104
Figure 2.7 – Uniaxial compression strain 0.42 w/c 3 hour BCSA.....	105
Figure 2.8 – Uniaxial compression strain 0.42 w/c 1 day BCSA.....	105
Figure 2.9 – Uniaxial compression strain 0.42 w/c 3 day BCSA.....	105
Figure 2.10 – Uniaxial compression strain 0.42 w/c 7 day BCSA.....	105

Figure 2.11 – Uniaxial compression strain 0.42 w/c 28 day BCSA	105
Figure 2.12 – Uniaxial compression strain 0.42 w/c 6 month BCSA.....	105
Figure 2.13 – Uniaxial compression strain 0.36 w/c 3 hour BCSA.....	106
Figure 2.14 – Uniaxial compression strain 0.36 w/c 1 day BCSA	106
Figure 2.15 – Uniaxial compression strain 0.36 w/c 3 day BCSA	106
Figure 2.16 – Uniaxial compression strain 0.36 w/c 7 day BCSA	106
Figure 2.17 – Uniaxial compression strain 0.36 w/c 28 day BCSA	106
Figure 2.18 – Uniaxial compression strain 0.36 w/c 6 month BCSA.....	106
Figure 2.19 – Uniaxial compression strain 0.42 w/c 7 day PC.....	107
Figure 2.20 – Uniaxial compression strain 0.42 w/c 28 day PC.....	107
Figure E.1 – Moment arm assembly	119
Figure E.2 – Moment arm assembly (exploded).....	119
Figure E.3 – Moment arm back plate.....	120
Figure E.4 – Moment arm top and bottom plate.....	120
Figure E.5 – Moment arm web stiffeners	121
Figure E.6 – Moment arm back plate stiffeners.....	121
Figure E.7 – Moment arm welding schematics	122
Figure E.8 – Steel box assembly.....	122
Figure E.9 – Steel box front plate	123
Figure E.10 – Steel box side plate	123
Figure E.11 – Roller assembly.....	124
Figure E.12 – Roller assembly (exploded)	124
Figure E.13 – Roller top plate.....	125

Figure E.14 – Roller bottom plate.....	125
Figure E.15 – Roller side plate	126
Figure E.16 – Roller pin.....	126

List of Tables

Table 3.1 – Coarse aggregate properties.....	33
Table 3.2 – Fine aggregate properties.....	34
Table 3.3 – Concrete mix designs.....	35
Table 4.1 – Uniaxial compression cylinder fresh concrete and strength results.....	57
Table 4.2 – Flexural compression specimen fresh concrete and strength results	57
Table 4.3 – Average uniaxial compression cylinder results	59
Table 4.4 – Flexural compressive specimen results.....	70
Table 4.5 – Strains in each specimen before failure	73
Table 4.6 – Flexural compressive specimen stress design parameter results	75
Table A.1 – Historical MOE data for BCSA cement concrete	96
Table A.2 – Historical PC uniaxial cylinder stress-strain data	97
Table A.3 – Historical PC flexural compression specimen data	98
Table 2.1 – All uniaxial compression cylinder data	108

Notation

Acronym Name:

CSA	calcium sulfoaluminate
BCSA	belite calcium sulfoaluminate
PC	portland cement concrete
w/c	ratio of water to cement by weight
ITZ	interfacial transition zone
DIC	digital image correlation
MOE	static modulus of elasticity
HRWR	high range water reducing admixture
DAQ	data acquisition unit
LVDT	linear variable differential transformer
ACI	American Concrete Institute
EC2	Eurocode Concrete Design Code
ASTM	American Standard Testing Methods
CSA A23	Canadian Standards Association Concrete Design Code

1 Introduction

1.1 General

Due to an increasing interest in sustainable infrastructure and rapid construction, engineers and owners are turning to alternative cements due to their improved environmental characteristics and specialty properties. Belitic calcium sulfoaluminate (BCSA) cement has gained interest in the last few years for use in structural applications mainly due to its rapid strength gain and reduced carbon emissions during manufacture.

The most recent edition of the American Concrete Institute (ACI) Building Code Requirements for Structural Concrete (ACI 318-19) allows engineers and designers to specify alternative cement concretes in design if these conform to design parameters for portland cement concrete (PC) and have sufficient data to prove that they are safe [1]. Initial investigation into steel reinforced beams cast with BCSA concrete found that they may exhibit a higher ductility than an equivalent PC beam [2]. This could suggest that the ultimate compression strain of the BCSA cement concrete exceeds the expected 0.003 compressive strain expected for normal strength PC or that the flexural compression stress distribution in the concrete is different because these parameters have a significant influence on ductility [3]. Ultimate compression stress and strain data for BCSA cement concrete are unavailable, and therefore it is necessary to investigate these properties to ensure safe and proper designs using this material. Reinforced beams, columns and prestressed concrete flexural members use the ultimate strength approach and rectangular stress block for design. This rectangular stress block is developed from empirically derived coefficients based on testing performed with PC. No such data currently exists for BCSA cement concrete.

The ultimate flexural compression strain is evaluated using either a two-point loading on a reinforced concrete beam or an eccentrically loaded c-shaped specimen. The c-shaped specimen was first proposed by Hognestad et al. [4] and negates the need to make a few analytical assumptions, making coefficient calculation easier and more accurate as later explained in section 2.4.1. This research used c-shaped specimens based on the design of Mertol et al. [5].

Measurement of uniaxial strain in concrete specimens can be used to create stress-strain relationship models for better predicting stresses at various strain values and for determining modulus of elasticity (MOE) for use in design. This work is also included in this report for BCSA cement concrete.

1.2 Problem Statement

The objective of this research was to verify structural properties or characterize previously untested structural properties of BCSA cement concrete including static modulus of elasticity (MOE), stress-strain response due to uniaxial compression, and uniaxial compression strain. These properties were evaluated and verified using three different w/c: 0.36, 0.42, and 0.48. And six different testing ages: 3 hours, 1 day, 3 days, 7 days, 28 days, and 6 months. Also, the stress-strain behavior of flexural compression BCSA cement concrete members was evaluated to determine if BCSA cement concrete performs similarly to PC in flexure. These properties were evaluated and verified using three different w/c: 0.36, 0.42, and 0.48. And two different testing ages: 7 days and 28 days.

The results from these tests were used to provide recommendations on the effectiveness of ACI 318-19 [1] and other code provisions in characterizing structural properties of BCSA

cement concrete and if any modifications to codes are required to accurately estimate structural properties of this alternative cement concrete.

The experimental research was performed at the Grady Harvell Civil Engineering Research and Education Center (CEREC) at the University of Arkansas, Fayetteville (UARK).

1.3 Research Objectives

Objectives of this research are outlined below:

- i. Evaluate the static modulus of elasticity of unconfined, unreinforced, uniaxially loaded concrete cylinders made from BCSA cement.
- ii. Obtain uniaxial compression strain values corresponding to the maximum stress resisted by BCSA cement concrete cylinders.
- iii. Determine the stress-strain relationship of BCSA cement concrete in uniaxial compression.
- iv. Evaluate code equations accuracy for estimating MOE in BCSA cement concrete.
- v. Determine the ultimate flexural compression behavior of BCSA cement concrete and develop a stress-strain model.
- vi. Determine flexural coefficients and stress block parameters for reinforced concrete design with BCSA cement concrete.
- vii. Evaluate the adequacy of code equations for estimating flexural compression coefficients and ultimate strain in BCSA cement concrete.

1.4 Report Arrangement

The background and previous research is broken into four parts, starting with a literature review on BCSA as an alternative cement material in Section 2.1, followed by background review on strain measurement methods using digital image correlation (DIC) in Section 2.2.

Stress-strain relationships of uniaxial compression specimens, concrete design code equations for MOE estimation, and historical considerations for measurement of uniaxial strain are presented in Section 2.3. Previous research and methods of determining stress and strain relationships and distribution for concrete flexural compression members is reported in Section 2.4.1. Background on historical flexural compression member testing and considerations for testing these specimens is discussed in Section 2.4.2. Data from historical testing of concrete flexural compression specimens and concrete design code equation estimations for stress distribution coefficients are presented in Section 2.4.3.

Materials used in this research, including cement, aggregates, admixtures, etc. are covered in Section 3.1. Experimental methodology of uniaxial compression strain cylinders and measurement of strain and calculation methods for MOE are presented in Section 3.2. Creation of flexural compression concrete specimens, strain gauge attachment, test setup, and loading scenario is covered in section 3.3.

Results and discussion of uniaxial compression cylinder data is presented in section 4.1 with recommendations and comparisons to historical testing data and concrete design code estimations of MOE. Data and results from flexural compression specimens are discussed in section 4.2 including comparisons to historical data and concrete design code estimations for stress distribution coefficients.

Summary of results and conclusions are presented in Chapter 6 along with recommendations for future research.

2 Background and Previous Work

2.1 Materials

BCSA cement is in the family of calcium sulfoaluminate (CSA) rapid setting hydraulic cements containing ye'elemite ($C_4A_3\bar{S}$), an anhydrous crystal first discovered and patented by Alexander Klein in the 1960s at University of California Berkeley [6]. BCSA cement, patented later by Ost et al. in the 1970s contains a much larger portion of belite or dicalcium silicate (C_2S) crystalline structures. BCSA cement consists of around 30-60% belite with 20-30% Ye'elemite, and 5-25% calcium sulfate [7]. Current cement production is estimated to consume roughly 12-15 percent of the total global industrial energy use and contribute about 7% of the global CO_2 emissions [8]. BCSA cement emits up to 30-60 percent less carbon dioxide during production compared to portland cement [9]. This is mainly due to the lower clinkering temperature required to fire belite and calcium sulfoaluminate [10], lower grinding energy due to softer clinker [11], and less calcium oxide in the cement, releasing less carbon dioxide chemically [8]. Due mainly to its high early strength, low shrinkage, and fast setting properties, BCSA cement concrete has been used as a rapid repair material for airfields and pavement surfaces, along with many other non-structural applications for over 40 years [12], [13].

BCSA cement concrete may carbonate more readily than PC [14] due to its differing chemistry and porosity. CSA cement concretes in general can show a high resistance to freeze thaw conditions [15] as well as high resistance to sulfate attack [16], [17]. BCSA cement also expands during hydration at early ages which can cancel out the effects of drying shrinkage at later ages [11], [18], [19]. However, some work has shown that BCSA cement may exhibit higher autogenous shrinkage than portland cement at an early age [20].

Literature suggests that it is important to add retarding admixtures to extend setting time and high range water reducing (HRWR) admixtures to increase workability when placing BCSA cement concrete [21]. Any typical set retarding admixture designed for hydraulic cements can be effective [22], however, citric acid is most commonly implemented for mix designs due to its cost effectiveness, ability to increase slump, reduce fresh concrete temperature and minimally effect later age strength [23]–[25].

Abundant research regarding the chemical and material characteristics of BCSA cement has been conducted over the past 50 years, however, the feasibility of using this cement in structural applications has only recently been explored. Recent experiments using BCSA cement in prestressed concrete beams and repair applications show promising results including the reduction of prestress losses [20], [26]–[30].

2.2 Digital Image Correlation

Traditional strain and displacement measurement techniques generally rely on contact-based measurements such as wire potentiometers, linear voltage differential transducers (LVDTs), or resistance-based strain gauges. These methods only provide measurements at a single point, and in the case of most strain gauges, are destroyed during tests to failure. Non-contact measuring devices are becoming more common and can overcome some of the disadvantages of traditional structural measurement techniques. Using one or multiple cameras and a random painted pattern of dots on a specimen, digital image correlation (DIC) software can analyze output from the cameras and track the absolute movements (displacement) and relative movements (strain) of an object. Through further analytical computation and multiple cameras to create a diffraction grating or three-dimensional images, shear strain, principal strains, curvature, velocity, acceleration, and more can be computed based on absolute and relative movement of

dots on the surface of a specimen. DIC was first used in the United States by W. H. Peters and Ranson in the early 1980s [31]. This technology has a wide range of applicability to countless scientific and engineering disciplines and for materials ranging from metals and polymers to biological materials [32]. DIC can be applied to specimens of nearly any size and is only limited to the capability of camera lenses and speckle patterns, allowing for specimen sizes ranging from the microscale and nanoscale to macroscale, including using satellite imaging [32], [33].

DIC has seen increased use in concrete research over the past decade, mostly relating to crack mapping, fracture analysis, and fatigue of structural specimens [34]–[36]. For measurement of fatigue cracking and fracture analysis in concrete specimens, it is recommended to use a picture capture sample rate of 8-12 hertz to properly map crack propagation [35]. However, for applications of measuring Lagrange strain or shear strain, in slow loading applications, 0.5-2 hertz sample rate is acceptable [37]. Strain measurements using DIC systems are shown to provide adequate strain values compared to traditional foil gauges provided that out of plane movement of the specimen is accounted for [38].

2.3 Uniaxial Compression in Concrete

2.3.1 Static Modulus of Elasticity

MOE values are important for structural design with concrete as it allows designers to estimate deflection behavior. MOE is the slope of the uniaxial stress-strain curve of the concrete below the elastic limit. This is traditionally evaluated with a MOE compressometer and linear variable differential transformer (LVDT) following ASTM C469 [39]. MOE in PC is difficult to estimate without performing a physical test as it is highly dependent on mix proportions and the strength, type, and MOE of the coarse aggregate used in the mix. Specifically, aggregates are found to greatly affect the slope and initial tangent modulus of the stress-strain graph or MOE

[40]. Also, with high strength concretes, the type of rock will influence the composite compressive strength and the strength of the interfacial transition zone (ITZ), affecting the expected MOE [41], [42]. Design code equations can be used to estimate MOE; ACI 318-19 [1] estimates that measured MOE will be within +/- 20% of equation 2-1. Canadian concrete design code (CSA 23.3:19) [43] defines MOE as shown in equation 2-2. European concrete design code (EC-2) [44] defines MOE as shown in equation 2-3.

ACI 318-19:

$$E_c = 57000\sqrt{f'_c} \quad \text{Equation 2-1}$$

Where E_c and f'_c are in psi

CSA 23.3:19:

$$E_c = 4500\sqrt{f'_c} \text{ [8.6.2.3]} \quad \text{Equation 2-2}$$

Where E_c and f'_c are in MPa

EC-2:

$$E_c = 22 \left[\frac{f'_c}{10} \right]^{0.3} \quad \text{Equation 2-3}$$

Where E_c and f'_c are in MPa

When a concrete specimen is loaded in pure uniaxial compression with linearly increasing load, a stress-strain graph can be made. From the slope of the beginning of the stress-strain graph, the MOE (E_c) can be calculated. There has not been much testing on BCSA cement concrete to determine typical MOE values or develop relationships between compressive strength and MOE. One study concluded that ACI-318 code values for estimating MOE based on compressive strength overestimates MOE for BCSA cement concrete at early ages (up to 28 days) and underestimates MOE at later ages (over 300 days) [45] as shown in Figure 2.1.

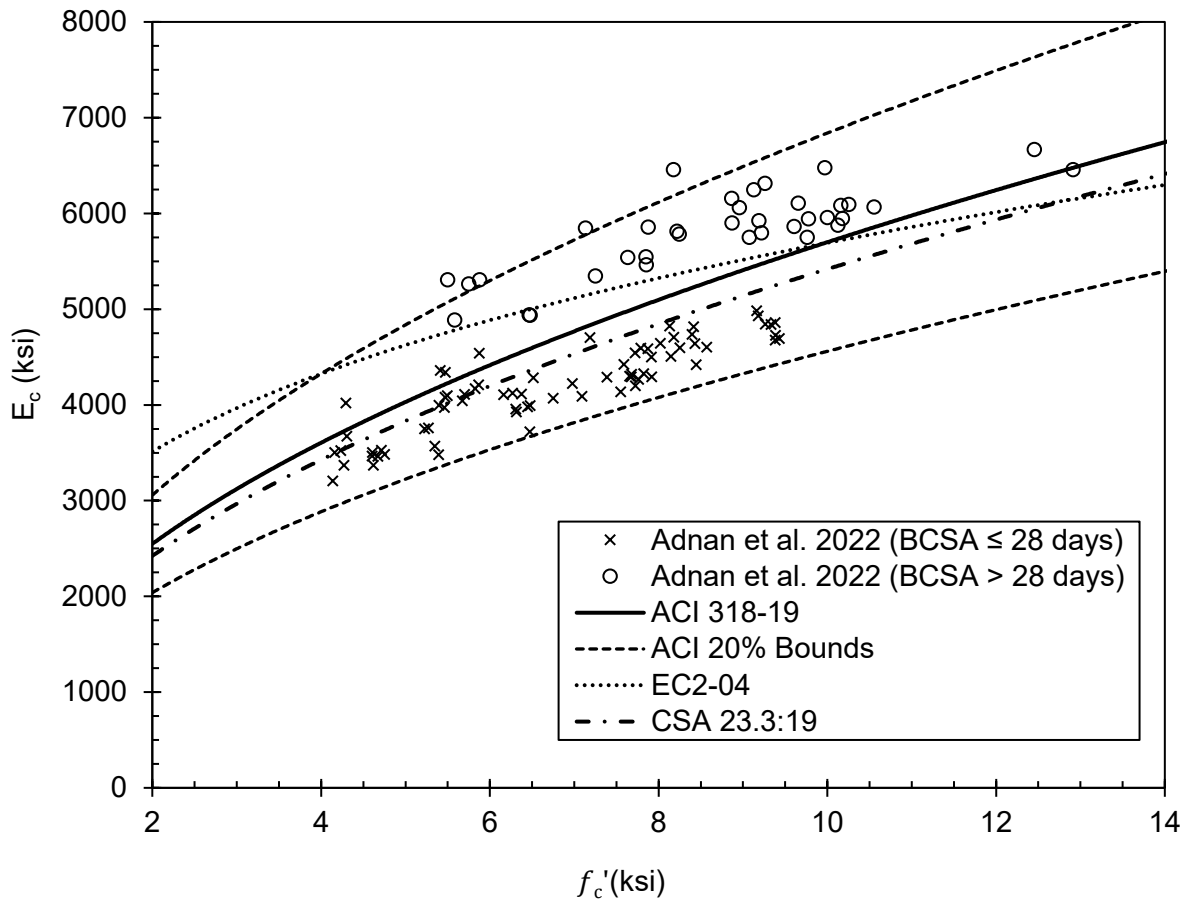


Figure 2.1 – MOE of BCSA cement concrete and code equations.

2.3.2 Maximum Uniaxial Compression Strain

This research sought to determine the maximum uniaxial compression strain (ϵ'_c) which corresponds with the maximum compressive stress (f'_c) for BCSA cement concrete using 4 in. diameter 8 in. tall concrete compression cylinders. A cylinder shape was selected over a cube or rectangle shape for measuring strain of specimens for three reasons. First, the entirety of a cube shape is affected by lateral stresses from the platens of a testing machine, where a cylinder with a height to diameter ratio of two or higher has a central section that is unaffected by lateral friction stresses and confined compression zones [46] as shown in Figure 2.2.

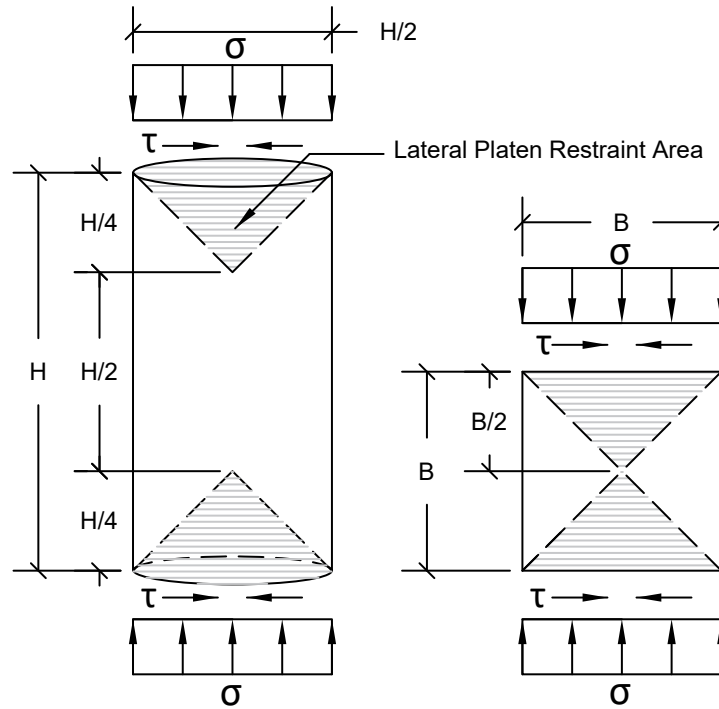


Figure 2.2 – Lateral restraint in cylinders and cubes from platens

It is uncommon and difficult to have true, unrestrained uniaxial loading in concrete specimens, because of platen restraint. This is due to increasing frictional force as normal force on the testing machine platens increases as load increases and lateral strains of the concrete increase. Platen restraint can be reduced through grease, Neoprene, Teflon, or other low friction bearing interfaces [47]. Platen restraint has the most effect on the stress strain shape after failure of the concrete has occurred [47]. This research only deals with the shape of the stress-strain graph prior to failure. There is little to no effect of platen restraint on compressive strength when height to diameter ratio equals or exceeds two [48]. Second, with a cylindrical shape, strain is more uniform from any side of the specimen. Finally, cylinder shapes allow comparison with more traditional MOE, compression strength, and strain measuring method results.

Other factors effecting measurement of ϵ'_c include size of aggregates in the cylinder relative to the specimen size [49], and strain gauge length relative to specimen length [50]. Also, measurement can be effected by a potentially weaker top of cylinder due to segregation of aggregates, bleed water, or finishing [50].

Historical maximum uniaxial strain values (ϵ'_c) at maximum stress (f'_c) for PC cylinders are shown in Figure 2.3 and includes data from five different sources [4], [51]–[55]. These data are traditionally obtained by rigidly attaching a compressometer to the top and bottom of the concrete cylinder, and using 2-3 displacement measurement devices (LVDTs, or dial gauges) to measure relative displacements between the two compressometer collars attached to the cylinder and relate the relative movement to strains in the concrete. Values for ϵ'_c typically range from 0.0015 to 0.0025, and in 1985 Carreira and Chu [50] published a correlation between ϵ'_c and f'_c through regression analysis of historical data. This correlation equation is show in equation 2-4. Both Carreira and Chu [50] and Hognestad et al. [4] recommend using a design value of 0.002 for concrete up to 7 ksi strength.

$$\epsilon'_c = (4.88f'_c + 168) * 10^{-5} \qquad \text{Equation 2-4}$$

Where f'_c is in ksi.

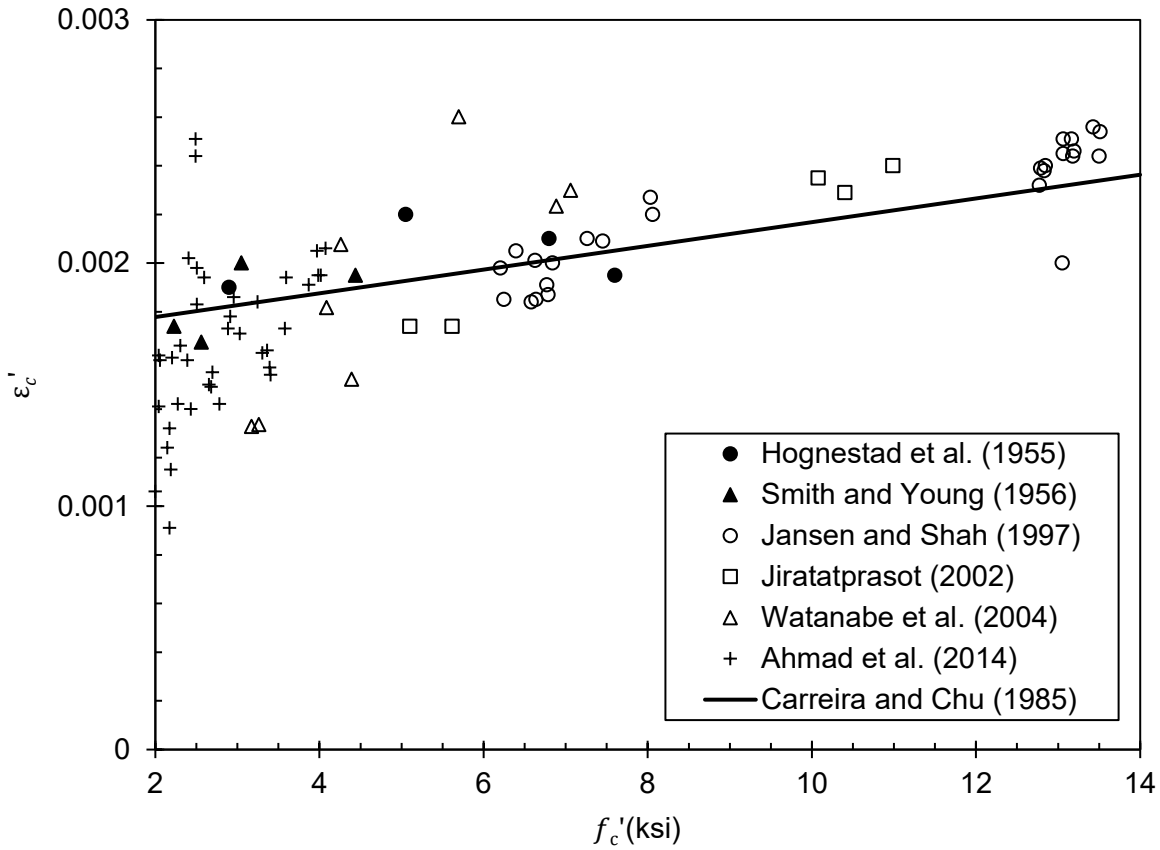


Figure 2.3 – Historical uniaxial compression strain at corresponding maximum stress for PC

2.4 Stress and Strain of Concrete Flexural Members

When designing reinforced concrete beams, columns or prestressed beams, designers use ultimate strength design principles. This approach assumes the ultimate strains and stresses at failure to determine equilibrium in the concrete and steel and predict total strength and deformations. Concrete behavior in flexural compression differs from that of uniaxial compression and concrete design codes account for these differences using design code parameters. In flexural compression, PC is assumed to experience a maximum compressive strain of 0.003 when the concrete crushes [56]. This is a higher strain value than what is commonly seen with specimens tested in uniaxial compression (Figure 2.3). For an under-reinforced concrete member, the tension steel is designed to yield before the maximum

compression strain is reached. Most concrete members in practice are designed to be under-reinforced to avoid premature crushing of the concrete and failure of the structural member before sufficient yielding, deflections, and cracking.

2.4.1 Strain and Stress Distribution

A concrete member with tension side reinforcing steel goes through four stages of strain and stress distribution as flexural load increases. In the first stage, with a relatively small load, no part of the beam has cracked and the tensile stress in the extreme tension fiber of the concrete has not exceeded its rupture strength. Strain and stress distribution is linear throughout the whole height of the member and the total compression resistance of the concrete equals the tensile force in the steel plus the tensile forces in the uncracked concrete. Tensile stress in the reinforcing steel can be calculated using the product of MOE in the steel and strain in the steel. The neutral axis in stage one can be determined using uncracked transformed section properties including any steel.

In the second stage as the load increases, the tensile stress at the extreme tension fiber of the member exceeds the rupture strength of the concrete, and the neutral axis moves further away from the tension steel as concrete is generally assumed to no longer resist any tensile force below the neutral axis (although in reality, tensile forces from concrete still exist some small distance below the neutral axis). Tensile stress in the reinforcing steel can be calculated in the same way as with stage one loading. The reinforcing steel has not yet yielded in stage two loading, so the load-deflection relationship for the member is still linear, albeit with a lower load-deflection slope or stiffness than in the uncracked stage. At this stage, the stresses and strains can be related using transformed cracked section properties. Strain and stress in stage one and two can be seen in Figure 2.4.

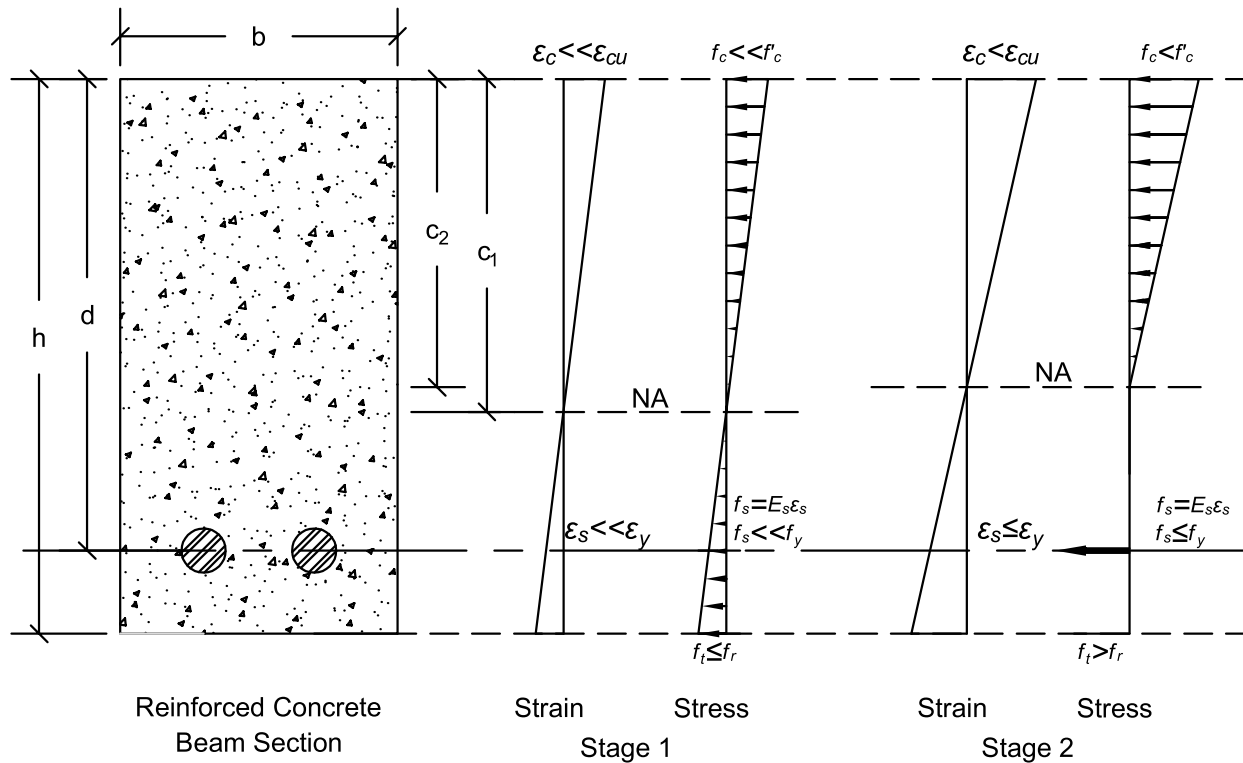


Figure 2.4 – Stage 1 and 2 strain and stress distribution diagram

In stage three loading, the reinforcing steel exceeds its yield strain and the stiffness of the member decreases. At this stage, strains and deflections increase with small increases in load and the stress in the concrete and steel can no longer be assumed to be proportional to their elastic moduli. It is more difficult to relate stresses and strains across the section at this stage since the behavior is nonlinear and the global deformation is dominated by the plastic deformation of the reinforcing steel. Stress of the reinforcing steel at this stage is determined by the unique stress-strain relationship of the steel used, determined through empirical means. In design, this stress is usually conservatively simplified to be equal to the yield stress and strain hardening is not considered.

In stage four, the reinforcing steel has a much higher strain than its yield strain if the beam is under-reinforced, but it has not yet reached rupture strain, and the top compression fiber

of concrete has reached its ultimate compression strain. Stress in the reinforcing steel behaves similarly as described for stage three loading. The strain distribution is assumed to remain linear in the cross section throughout all stages of loading; however, the stress distribution in the concrete in compression is no longer linear at ultimate loads as shown in Figure 2.5. This stage is the basis for ultimate strength design, or the strength limit state in many design codes.

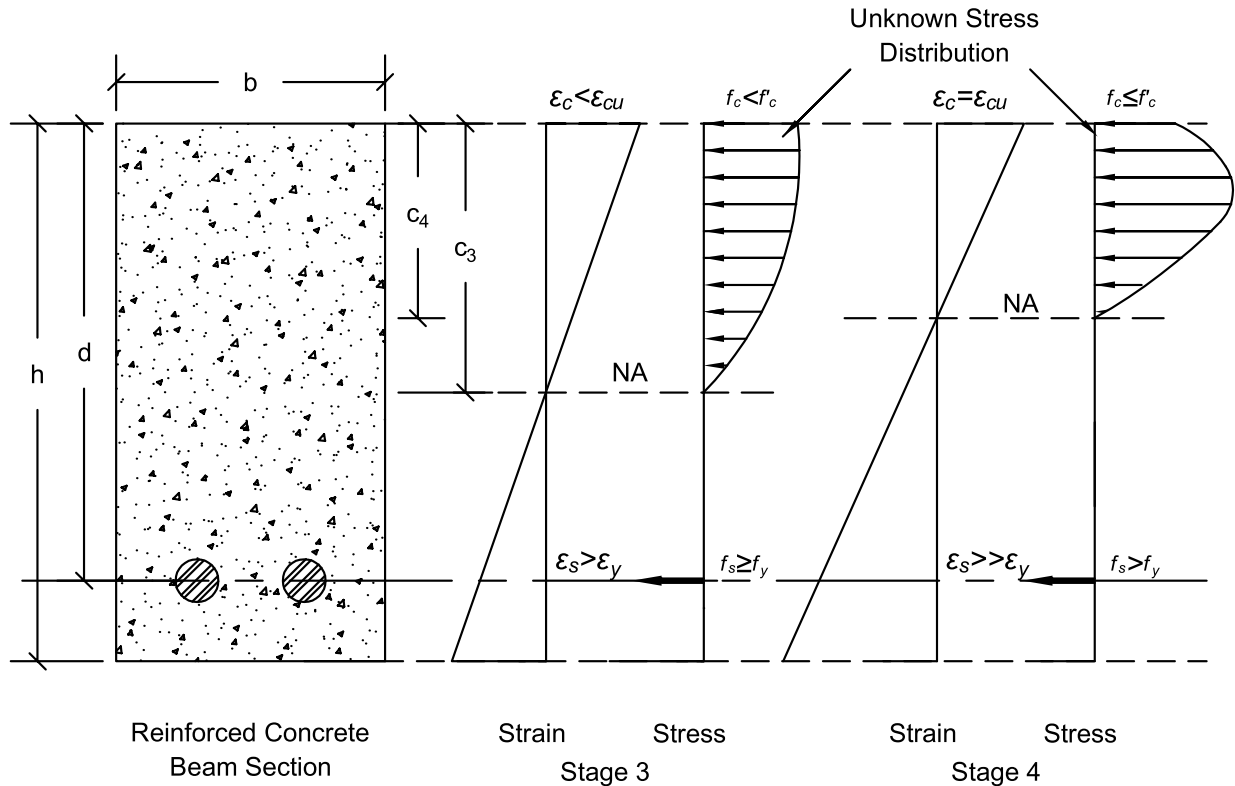


Figure 2.5 – Stage 3 and 4 strain and stress distribution diagram

In design, the nonlinear compression stress at ultimate compression failure is typically approximated by an equivalent stress block with dimensions found through empirically derived relationships developed in historical research and published in design codes. The stress in the steel is conservatively assumed to be equal to its nominal yield stress, so strain hardening is not considered.

Four other assumptions are made in this design: strains remain linear throughout all stages (plane sections remain plane after deformation), tensile stress in the concrete is neglected, forces can be calculated using assumed MOE, and there exists a perfect bond between steel and concrete.

At stage four limit state with tension-controlled beam behavior, ACI 318-19 [1] proposes a value for ultimate concrete strain (ϵ_{cu}) of 0.003, modifier to depth of concrete compression (β_1) based on cylinder strength (f'_c), magnitude of stress (α_1) as 0.85 times f'_c , and stress in tension steel (f_s) as equal to yielding stress of steel (f_y). Strain in tension steel is calculated using known depth of reinforcement and assuming a linear strain distribution. For tension-controlled beams, strain in tension steel (ϵ_s) should be greater than or equal to 0.005. ACI 318-19 [1] proposed strain and stress distribution diagrams and equations are shown in Figure 2.6.

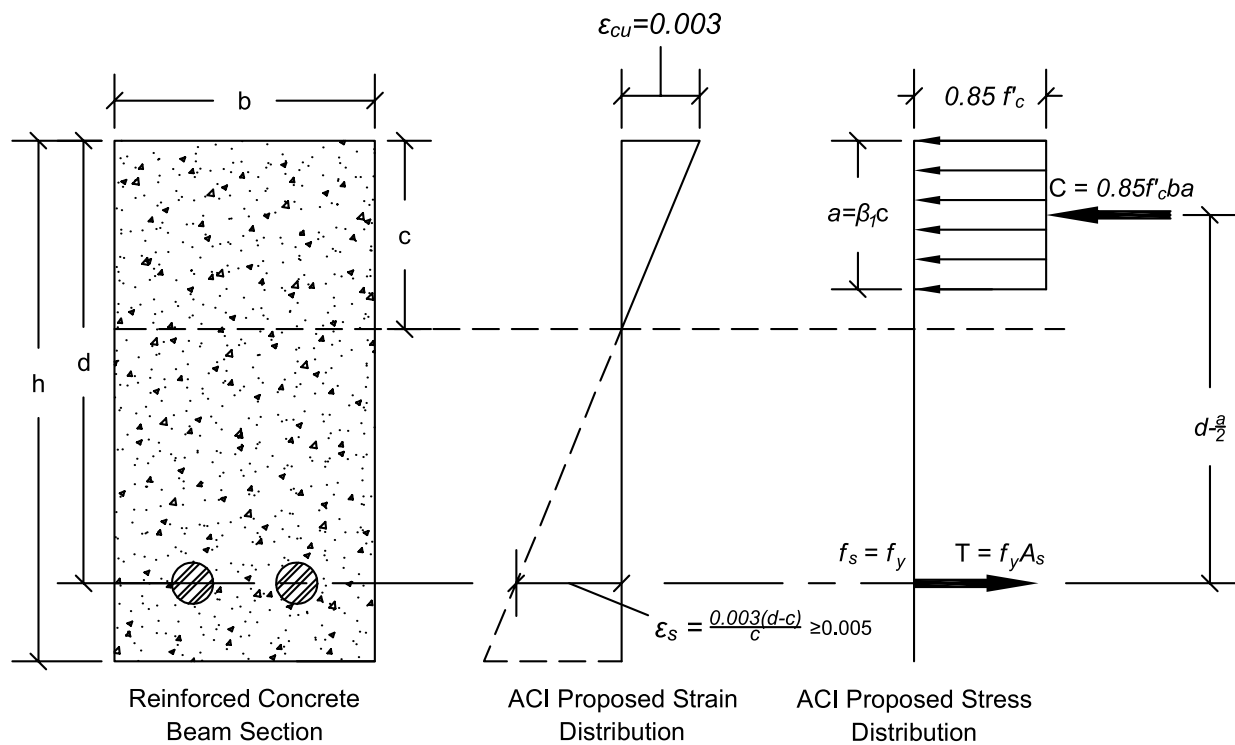


Figure 2.6 – ACI proposed strain and stress distribution in tension controlled flexural beams

2.4.2 Concrete in Flexural Compression

Concrete flexural members such as beams and columns behave in a non-uniform manner at failure loads. The strength design procedures in the ACI Code are developed based on the assumption that cracked concrete below the neutral axis carries no stress (all tension carried by tension steel) and the concrete above the neutral axis is subjected to a combination of axial and flexural compression stress. It is generally understood that the stress-strain relationship for a concrete cylinder in axial compression differs from that of the concrete subjected to combined flexure and compression, particularly after microcracking has occurred. Due to the non-uniform compression stress distribution in flexural compression members, some of the concrete has little to no compressive stress and does not experience microcracking to the same degree as a uniaxial compression specimen. Also, it has been observed that in flexural compression members there is a “sliding planes phenomenon” of concrete. The mechanism of sliding planes is similar to shear-bond cracking seen in uniaxial specimens and is caused by the strain gradient in the compressed concrete. It is theorized that this failure mechanism is the cause of the post peak stress behavior of concrete in flexure allowing it to exhibit higher strains [57].

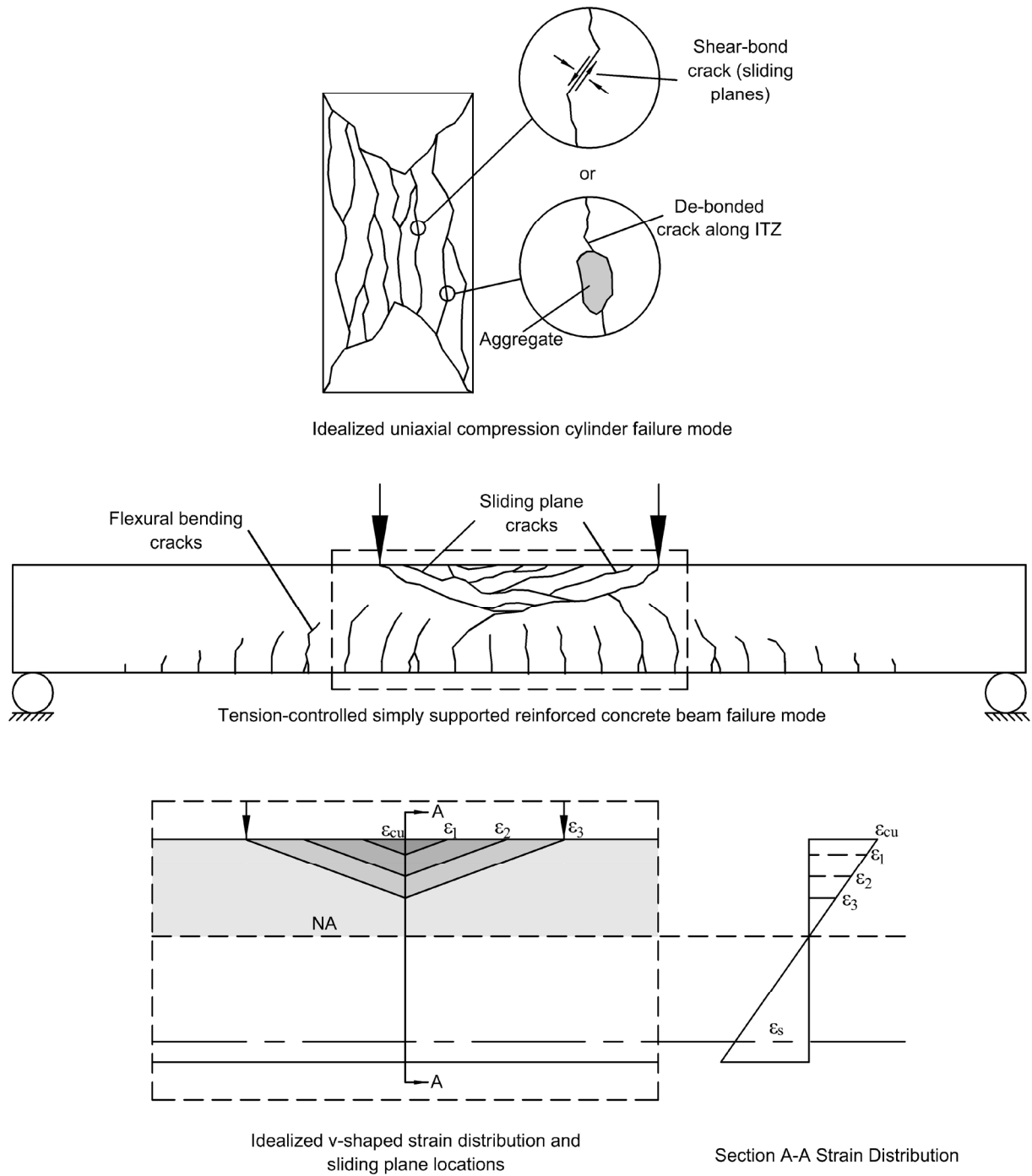


Figure 2.7 – Failure mechanisms of different concrete specimens

To develop a stress-strain relationship for flexurally loaded concrete, and to find the maximum compression strain the concrete can resist, some form of “eccentric bracket” specimen has historically been tested. This specimen is often “C” shaped and has a main axial load and an

additional eccentric load which results in a moment on the sample. Through the combination of these two loads, a linear distribution of strain from zero strain on one member face to the ultimate compression strain on the opposite face can be achieved in the middle of the “C” shape. The first example of this type of testing was Hognestad in 1955 [4]. The test setup and equations Hognestad developed have evolved over the years, resulting in improved testing methods and equations. The current strength design assumptions in the ACI Code are based on these historical tests.

To attempt to control some of these assumptions through experimental setup, the C-shaped flexure specimen can be used to replicate the compression side of the neutral axis at stage four loading of a reinforced concrete beam. Figure 2.8 shows how, through the balancing of a pure compression load and an eccentric “moment” load, the middle unreinforced concrete section of the specimen can represent the portion of strain or stress distribution above the neutral axis. This eliminates the need for steel reinforcement, negating the assumption of perfect bond between concrete and reinforcement. Also, this testing method attempts to ensure no concrete is in tension throughout the test, so no assumptions have been made regarding tensile strength of concrete.

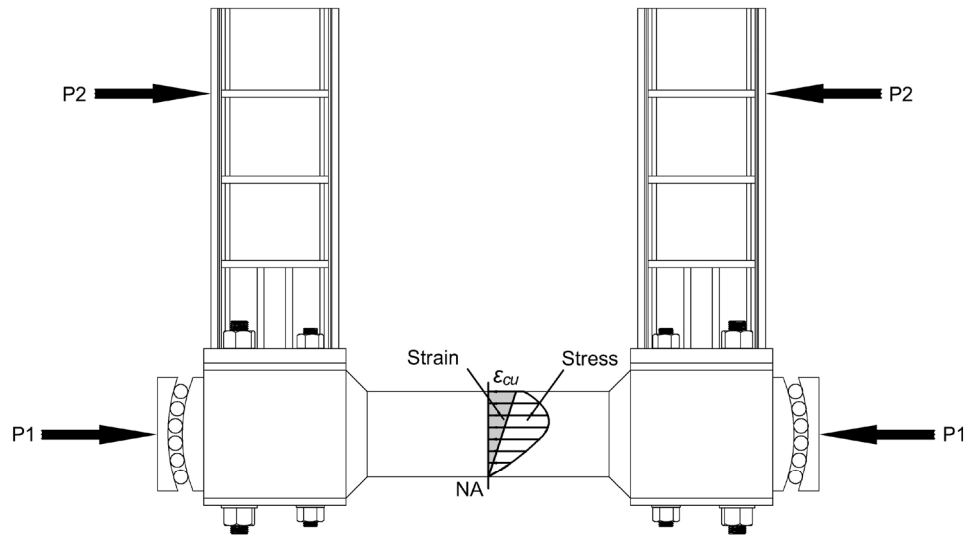


Figure 2.8 – Strain and stress distribution in specimen

Mertol et al. at North Carolina State University [58] performed eccentric bracket tests to determine the stress block parameters for high strength concretes since higher compressive strengths (>8000 psi) were becoming more widely used. These researchers developed a method for evaluating the ultimate compression strength of high strength PC, eliminating some of the issues that appeared in previous iterations of these bracket tests. Mainly, the design of the Mertol et al. eccentric bracket specimens consisted of simple geometry and easy to construct formwork. Removable moment arms allowed the specimens to be stored upright during curing and required less internal reinforcement. The methods proposed by Mertol et al. were followed in this research to ensure compatibility with past work.

Historical results compiled from 18 studies using eccentric bracket specimens spanning from the original research by Hognestad et al. in 1955 to Khadiranaikar and Awati in 2012, found that ultimate compression strain values for concrete range from .002 strain to over .005 strain, with the majority of values falling between .0025 and .0035 strain [3]. There is also little

correlation between compressive strength and strain, and the 5th percentile statistical best fit of values is 0.00267 strain which is 11 percent lower than ACI code provisions [3].

The size of the test section also seems to have an impact on the flexural performance. Researchers Kim J. et al [59], using the same C-shaped specimen developed by Hognestad but scaled at three different sizes found that as the size of specimen increases, the compressive failure stress in the concrete decreases. This follows the original findings by Gonnerman in 1925 with uniaxial stress tests using cylinders of different volumes, maintaining the same diameter to height ratio [60]. In C-shaped specimens, this is a more apparent phenomenon than in uniaxial compression cylinders at different sizes [61]. These findings are important to consider for this research when comparing them to results from other research studies.

2.4.3 Stress Distribution Estimation

Although strain is linear in a flexural member at locations sufficiently far from discontinuities, stress is nonlinear and difficult to estimate. Stress is often idealized into an arbitrary, equivalent “stress block” where there is an established equation for the shape of the stress block based on empirical values. The area under the stress curve of the shape can be used to calculate compression force in the flexure member. Historically, there have been many shapes proposed by researchers to describe the compression and tension stress distribution in concrete flexural members including rectangular, triangular, trapezoidal, parabolic, cubic parabolic, sine wave with cubic parabolic, elliptical, hyperbolic, and compound shapes [62]. Most popular among these being the rectangular stress distribution with its adoption into many modern reinforced concrete design guides and code books. Estimation of the stress distribution into an “equivalent rectangular stress block” was first proposed by Von Emperger in 1908 and E. Suenson in 1912 [62] which was later revised and popularized in 1937 by Whitney [63]. Within

the compression region of a flexural member, there are three main coefficients used to describe the shape of stress distribution. Whitney adopted the coefficients k_1 , k_2 , and k_3 from the original author F. Stussi [64] for the rectangular stress block, as shown in Figure 2.9 [65]. Coefficient k_1 is the ratio of the average stress to the maximum stress. Coefficient k_2 is the ratio of the depth to the resultant of the compressive stress to the depth to the neutral axis. Coefficient k_3 is the ratio of the maximum stress to the compressive strength of an uniaxially loaded concrete cylinder (empirically assumed to be 0.85 for PC). Parameter k_3 accounts for all the differences in stress-strain behavior between concrete in uniaxial compression and concrete under combined flexure and compression; differences caused by the strain gradient effect, shape and size effects, slower loading rate, and higher achieved strains in flexure. For ease of design, this “equivalent stress block” and the strength design method is now used by designers to calculate nominal ultimate moment capacity for flexural members. The “k” coefficients are used to describe the shape parameters of the actual stress distribution curve and an equivalent stress block, but in common practice and in the ACI Code, the factors α_1 and β_1 are used to describe the equivalent stress block shape. These factors can be used to describe any shape function of stress distribution, but most commonly they describe rectangular distribution and are defined as follows: β_1 is typically a reduction factor applied to the height of the concrete above the neutral axis (c) that is in compression and α_1 describes the width of the stress block generally as a reduction to cylinder compression strength (f'_c). A visual representation of these factors can be seen in Figure 2.9 where b is the width of a concrete beam in flexure, d is the depth to center of tension reinforcing steel from extreme compression fiber of concrete, c is the depth to the neutral axis, ϵ_{cu} is ultimate compression strain, ϵ_s is strain in the tension steel, f'_c is the compression strength of concrete, f_y is the yield strength of reinforcing tension steel, A_s is the area of reinforcing tension

steel, C is total compression force in concrete, T is total tension force in tension reinforcing steel, and all other factors are as described previously.

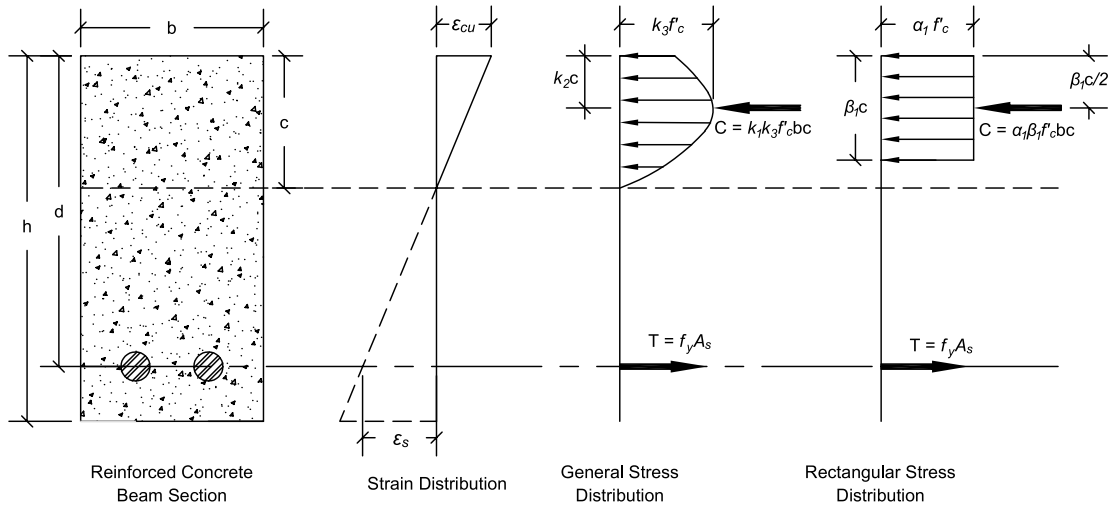


Figure 2.9 – Strain and stress distribution diagram

Mathematical relationships between general stress distribution parameters and equivalent distribution parameters when simplified as a rectangular distribution as developed by Whitney are as follows:

$$\frac{\beta_1 c}{2} = k_2 c \rightarrow \beta_1 = 2k_2 \quad \text{Equation 2-5}$$

$$C = k_1 k_3 f'_c bc = \alpha_1 \beta_1 f'_c bc \quad \text{Equation 2-6}$$

$$\alpha_1 (2k_2) f'_c bc = k_1 k_3 f'_c bc \rightarrow \alpha_1 = \frac{k_1 k_3}{2k_2} \quad \text{Equation 2-7}$$

$$M = C \left(d - \frac{\beta_1 c}{2} \right) = k_1 k_3 f'_c bc (d - k_2 c) \rightarrow k_2 = \frac{d}{c} - \frac{M}{Cc} \quad \text{Equation 2-8}$$

Most researchers using eccentric bracket testing developed their own mathematical models for determining k_1 , k_2 , and k_3 coefficients and subsequently β_1 and α_1 . These coefficients provide a baseline for comparison with other researchers to contrast results with

different tested eccentric bracket shapes. The stress-strain relationships used to calculate stresses in the flexure specimen are often based on a stress-strain relationship developed through testing uniaxial cylinders. Mattock et al [66], building off Hognestad's work, helped develop a mathematical model for calculating these coefficient values from C-shaped eccentric bracket testing and further refined the rectangular stress block using the ultimate strength design method.

The American Concrete Institute (ACI 318-19) [1] assumes a value of 0.003 for concrete of any cylinder strength (f'_c). For the ratio of cylinder strength to flexural strength (α_1), ACI assumes a value of 0.85 for concrete of any f'_c . Parameter β_1 is estimated to be 0.85 when strengths do not exceed 4 ksi, then decreases linearly between 0.85 and 0.65 for strengths between 4 and 8 ksi, and concrete over 8 ksi is assumed to have a β_1 value of 0.65. Mathematical representations of these values are show in Equation 2-9 through 2-11

Canadian Standards Association (CSA23.3:19) [43] estimates ultimate concrete strain to be 0.0035 for concrete of any strength (f'_c). Parameter α_1 is assumed to be linearly decreasing from 0.85 to 0.67 between 0 and 17.4 ksi (f'_c). Parameter β_1 is estimated to be linearly decreasing from 0.97 to 0.67 between 0 and 17.4 ksi. Both α_1 and β_1 assume a value of 0.67 for any concrete strength exceeding 17.4 ksi. These values are included in equations 2-12 through 2-14.

European Code Standards (EC2-04) [44] assumes a value of 0.0035 ultimate strain for concrete below 7.25 ksi and decreases logarithmically to 0.0026 for concrete exceeding 12.8 ksi. Parameter α_1 is assumed to be 1.0 for concrete strengths less than 7.25 ksi, decreasing linearly from 1.0 to 0.8 for strengths between 7.25 and 13 ksi. Parameter β_1 is estimated to be 0.8 for concrete strengths less than 7.25 ksi and decreases linearly from 0.8 to 0.56 for strengths between 7.25 and 13 ksi. Mathematical representations of EC2-04 code estimations can be seen

in Equations 2-15 through 2-17 and graphical representations in Figure 2.10 for ultimate strain, Figure 2.15 for α_1 , and Figure 2.16 for β_1 .

ACI 318-19:

$$\varepsilon_{cu} = 0.003 \text{ [22.2.2.1]} \quad \text{Equation 2-9}$$

$$\alpha_1 = 0.85 \text{ [22.2.2.4.1]} \quad \text{Equation 2-10}$$

$$\beta_1 = \begin{cases} 0.85 & \text{for } f'_c \leq 4 \text{ ksi} \\ 0.85 - 0.05(f'_c - 4) \geq 0.65 & \text{for } f'_c > 4 \text{ ksi} \end{cases} \text{ [22.2.2.4.3]} \quad \text{Equation 2-11}$$

Where f'_c is in ksi.

CSA 23.3:19:

$$\varepsilon_{cu} = 0.0035 \text{ [10.1.3]} \quad \text{Equation 2-12}$$

$$\alpha_1 = 0.85 - 0.0015 * f'_c \geq 0.67 \text{ [eq. 10-1]} \quad \text{Equation 2-13}$$

$$\beta_1 = 0.97 - 0.0025 * f'_c \geq 0.67 \text{ [eq. 10-2]} \quad \text{Equation 2-14}$$

Where f'_c is in MPa.

EC2-04:

$$\varepsilon_{cu} = \begin{cases} 0.0035 & \text{for } 12 < f'_c \leq 50 \text{ MPa} \\ 0.0026 + 0.035 \left[\frac{(90-f'_c)}{100} \right]^4 & \text{for } 50 < f'_c \leq 90 \text{ MPa} \end{cases} \text{ [Table 3.1]} \quad \text{Equation 2-15}$$

$$\alpha_1 = \begin{cases} 1.0 & \text{for } f'_c \leq 50 \text{ MPa} \\ 1.0 - \frac{f'_c-50}{200} & \text{for } 50 < f'_c \leq 90 \text{ MPa} \end{cases} \text{ [eq. 3.21-22]} \quad \text{Equation 2-16}$$

$$\beta_1 = \begin{cases} 0.8 & \text{for } f'_c \leq 50 \text{ MPa} \\ 0.8 - \frac{f'_c-50}{400} & \text{for } 50 < f'_c \leq 90 \text{ MPa} \end{cases} \text{ [eq. 3.19-20]} \quad \text{Equation 2-17}$$

Where f'_c is in MPa.

Ultimate strain data compiled from 11 sources using flexure specimen tests range from 0.002 to over 0.0055 with most ultimate strain data falling between 0.0025 and 0.0035 [1], [5],

[72]–[75], [43], [44], [62], [67]–[71]. There is no well-established correlation between cylinder strength (f'_c) and ultimate strain, however, Eurocode (EC2-04) estimates strain at 0.0035 for strengths up to 7.25 ksi and adjusts to lower strains for concrete exceeding 7.25 ksi. Historical ultimate strain data from eccentric bracket specimens and code estimations can be seen in Figure 2.10.

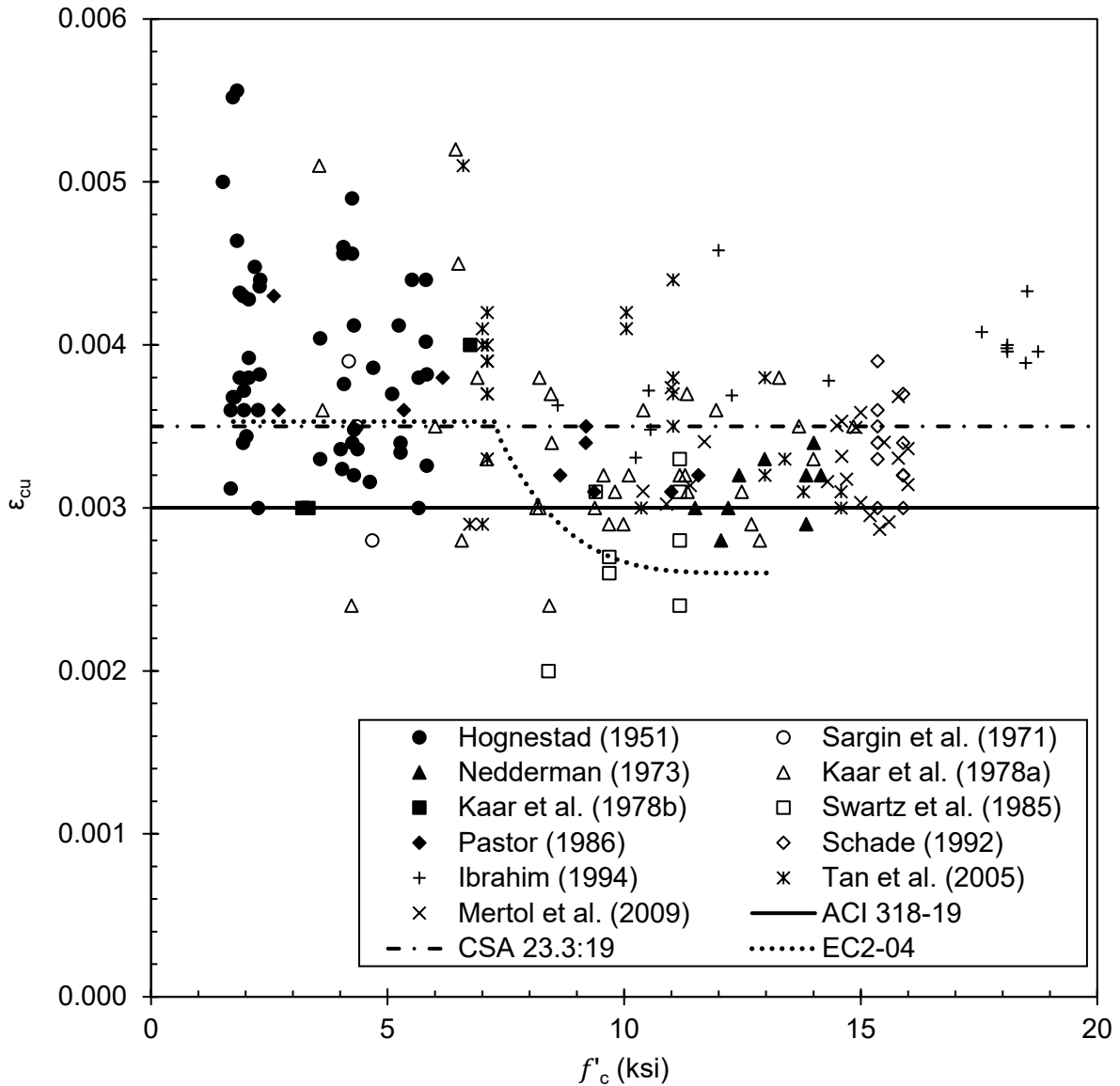


Figure 2.10 – Ultimate strain of concrete flexural members

Parameter k_1 or the ratio of the average stress in the section to the maximum stress is represented in Figure 2.11 and includes results from 7 sources [5], [69]–[73], [76]. There is no established correlation between concrete strength and parameter k_1 . Values typically range from 0.5 to 0.8.

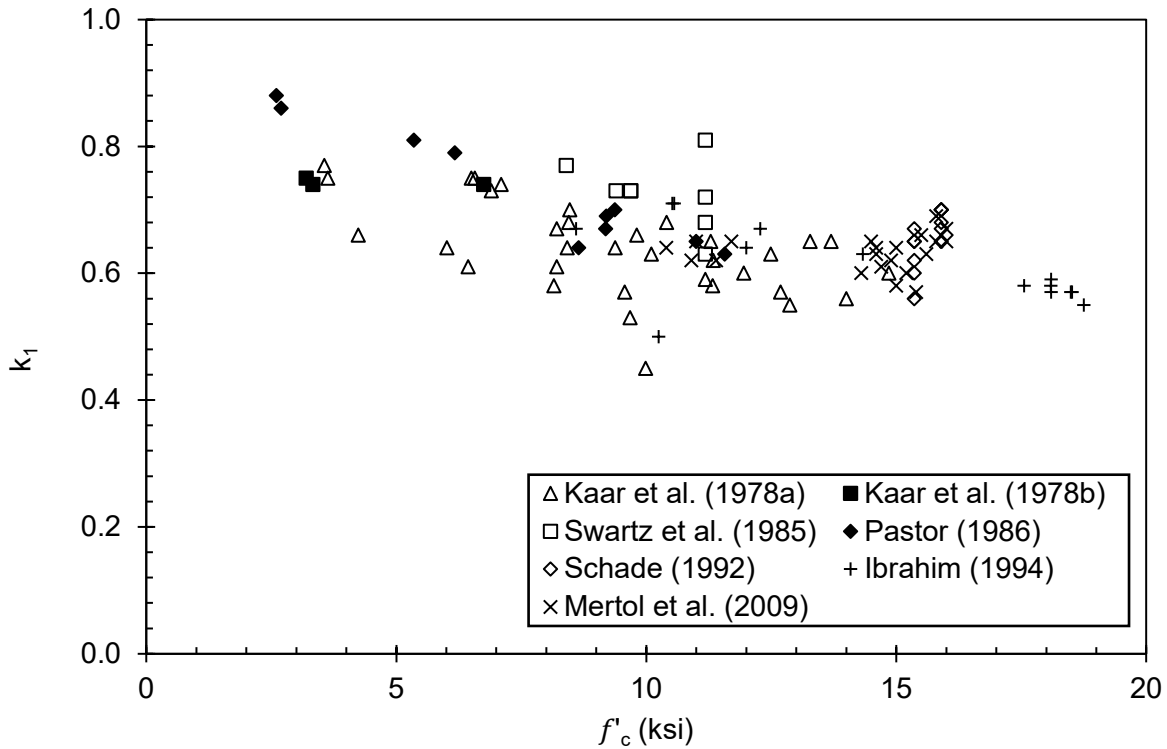


Figure 2.11 – Parameter k_1 values for concrete flexural members

Parameter k_2 or the ratio between the depth of the resultant compression force and the depth of the neutral axis is directly correlated to β_1 . As strength increases, this ratio decreases, meaning the center of compression force moves further from the neutral axis. For normal strength concrete ($f'_c < 8$ ksi), values for k_2 range from 0.38 to 0.49 and for strength values over 8 ksi, k_2 can typically range from 0.32 to 0.42 based on historical data as shown in Figure 2.12 compiled from 10 sources [4], [5], [68]–[73], [75], [76].

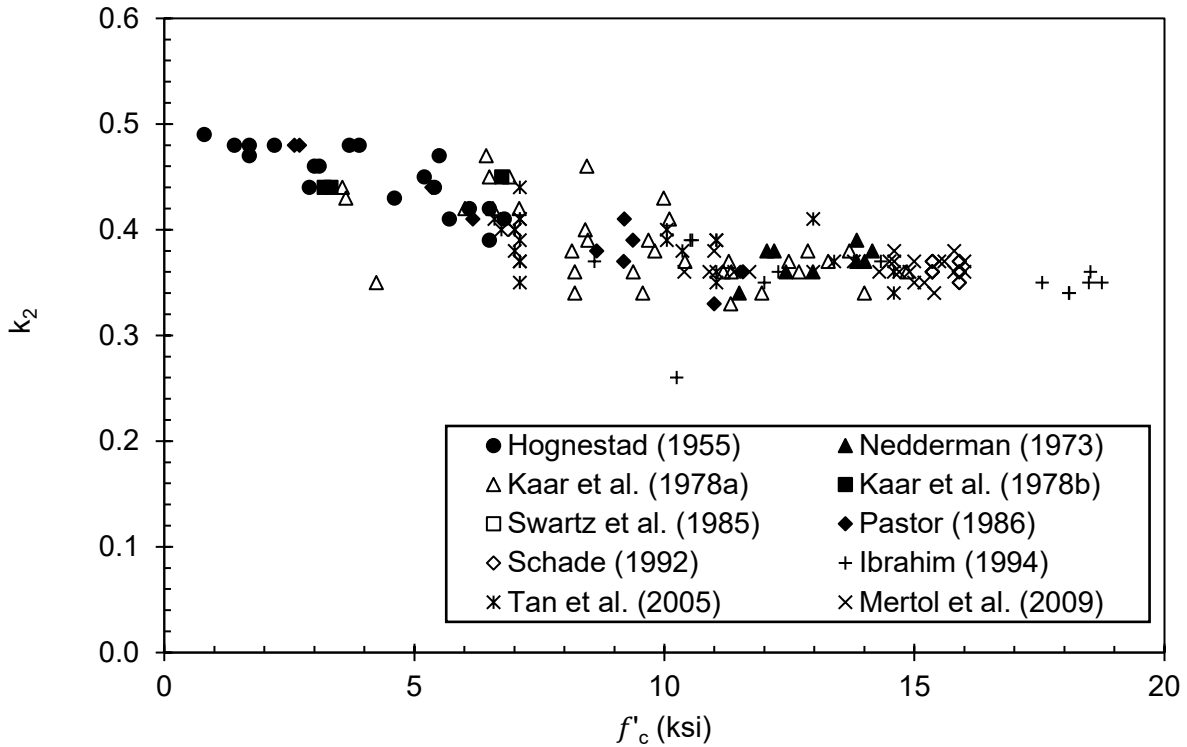


Figure 2.12 – Parameter k_2 values for concrete flexural members

Historical values for parameter k_3 or the ratio of maximum compression stress in the flexure specimen to the compression strength of a uniaxial cylinder (f'_c) can be seen in Figure 2.13. This data includes 8 sources [5], [67], [69]–[73], [76]. k_3 has little to no correlation with concrete strength. Values for this ratio typically fall between 0.8 and 1.2 based on historical values.

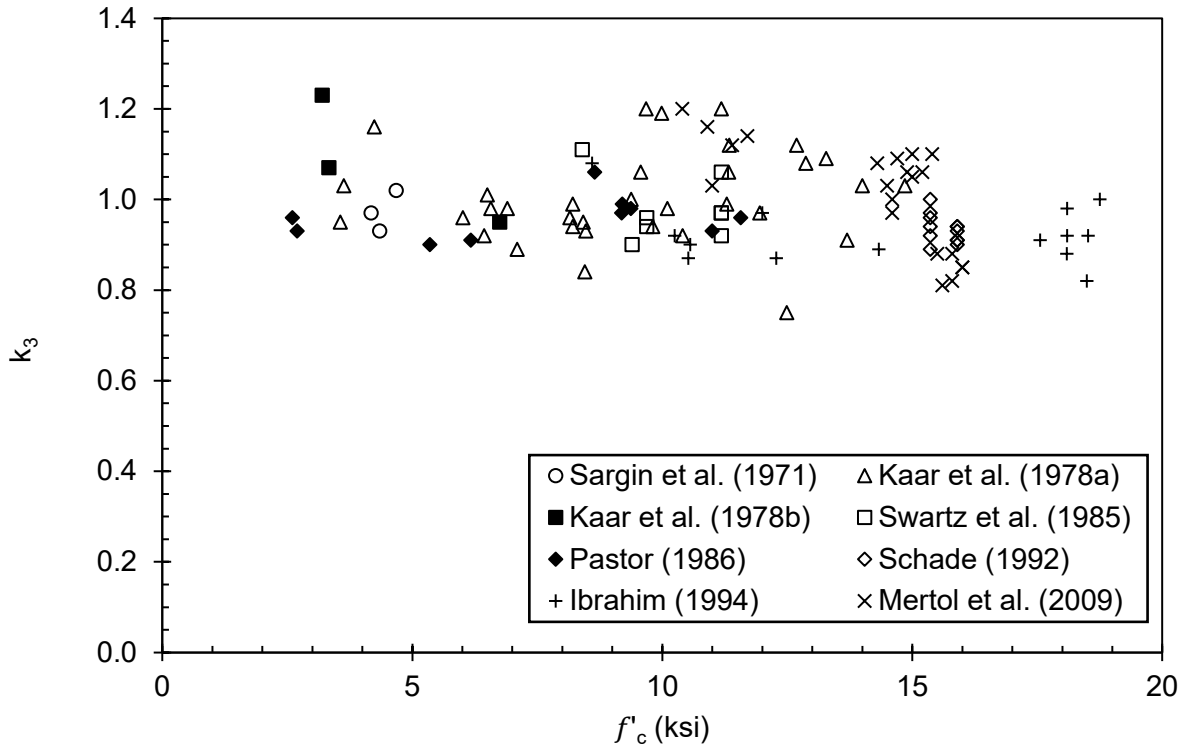


Figure 2.13 – Parameter k_3 values for concrete flexural members

The product of parameters k_1 and k_3 which equals the product of α_1 and β_1 , is shown in Figure 2.14 and represents historical data from 10 sources as well as 3 code estimates [1], [4], [73]–[75], [5], [43], [44], [68]–[72]. These parameters effectively reduce the quantity of f'_c when calculating the total compression force in flexural members. As f'_c increases, the product of these parameters is reduced. The product of ACI 318-19 estimates of α_1 and β_1 is conservative and falls below many of the historical data. CSA 23.3:19 estimation falls in the center of historical data and EC2-04 overestimates early age historical parameter values for normal strength concrete ($f'_c = 4\text{--}8$ ksi). Ranges for this product for normal strength concrete range from 0.5 to 0.8 and for high strength concrete range from 0.4 to 0.7 based on typical historical data.

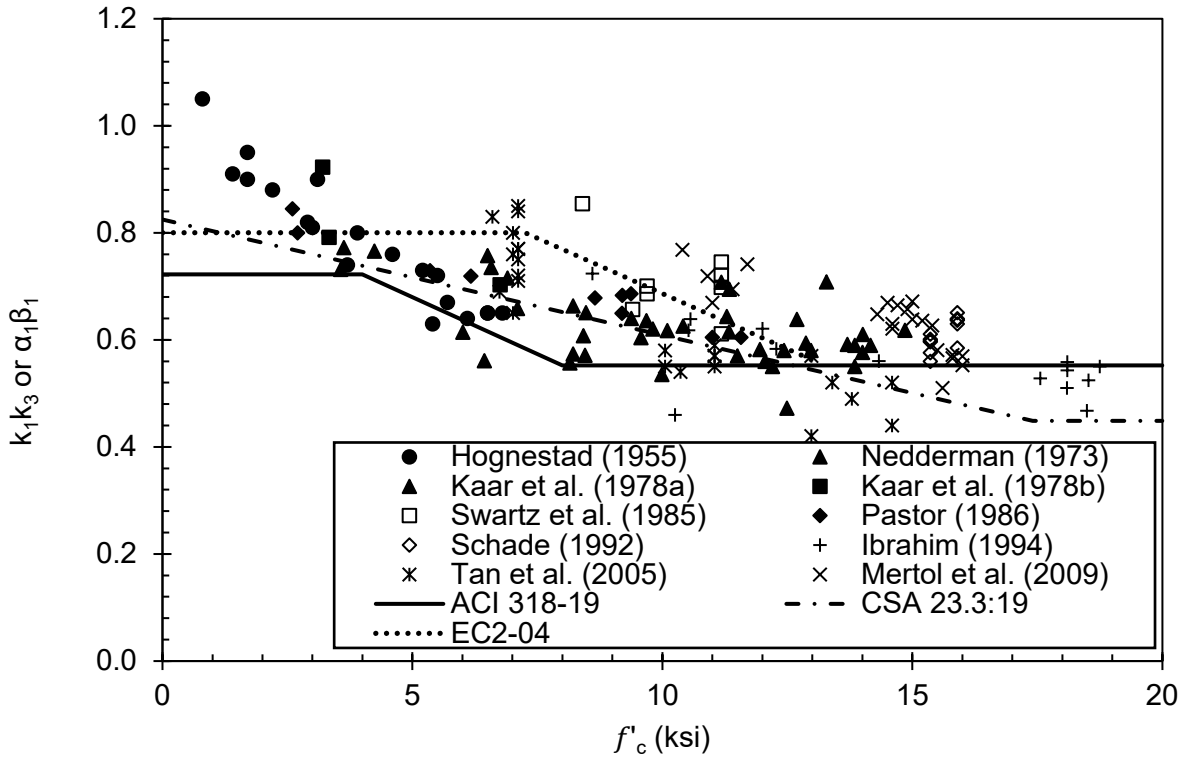


Figure 2.14 – Product of parameters k_1 and k_3 or β_1 and α_1 for concrete flexural members

Parameter α_1 or the modification to f'_c for concrete in flexural compression, is represented by historical data compiled from 10 sources and 3 code equations in Figure 2.15 [1], [4], [73]–[75], [5], [43], [44], [68]–[72]. As f'_c increases there is a slightly decreasing linear correlation between f'_c and α_1 as established by EC2 for concrete strengths over 7.25 ksi and by CSA A23.3:19 for concrete less than 17.4 ksi and by historical data. ACI 318:19 assumes no correlation between α_1 and f'_c . Typical historical values for this parameter range from 0.6 to 1.1.

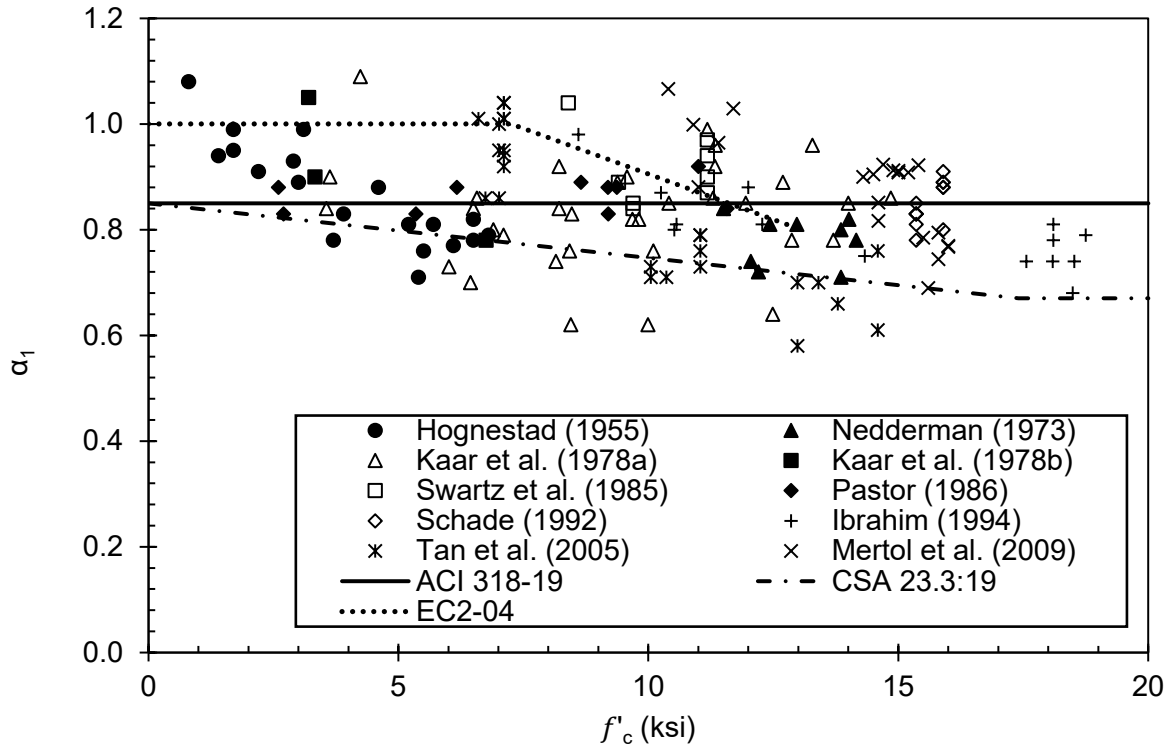


Figure 2.15 – Parameter α_1 for concrete flexural members

Parameter β_1 or the ratio of the depth of the rectangular compression stress block to the depth of the neutral axis in a flexural member is tied directly to parameter k_2 . Historical data for parameter β_1 from 10 sources and 3 code estimates is shown in Figure 2.16 [1], [4], [73]–[75], [5], [43], [44], [68]–[72]. Based on historical data and code equations, it is understood that as f'_c increases, β_1 decreases. ACI 318-19 is conservative in this estimation, falling below most historical data, EC2-04 is conservative when f'_c is less than roughly 7 ksi and falls in the middle of historical data for all other strengths. CSA A23.3:19 falls within the center of historical data for estimating β_1 for all strengths. The typical range for concrete with a strength lower than 8 ksi is 0.65 to 1.0. For concrete with strength over 8 ksi, β_1 is between 0.65 and 0.9.

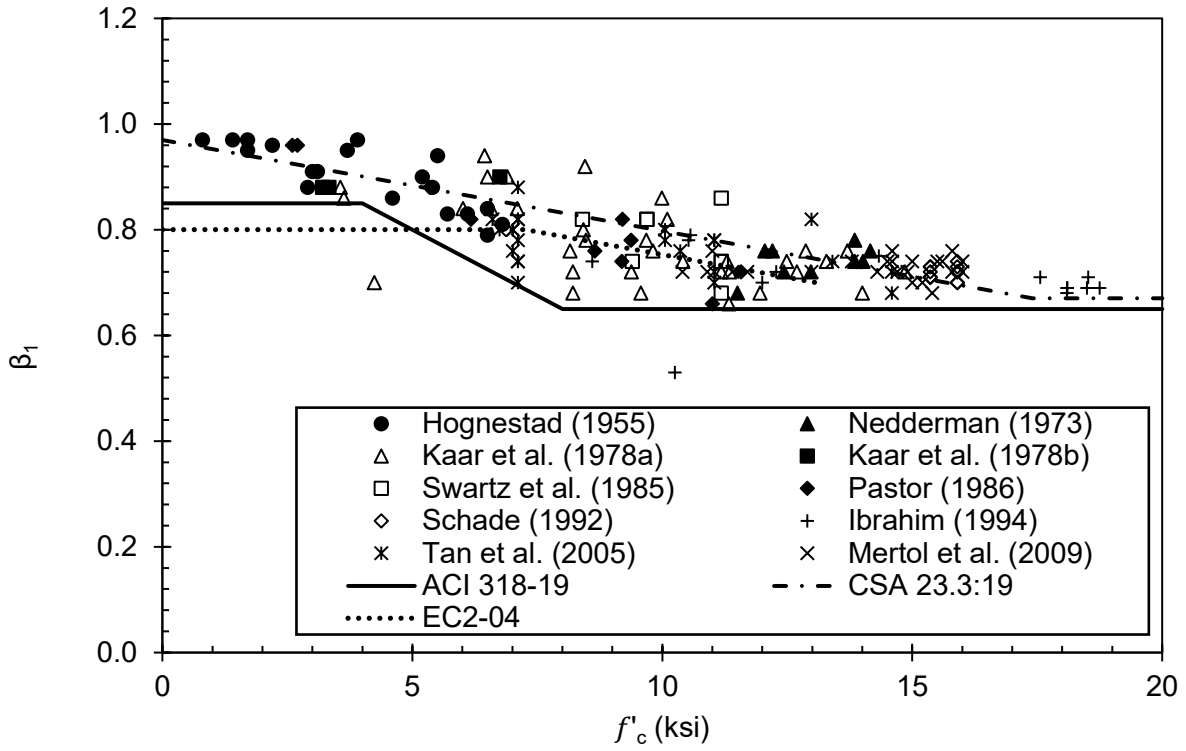


Figure 2.16 – Parameter β_1 for concrete flexural members

3 Experimental Methodology

3.1 Materials

All coarse aggregates used in this research were 1 in. nominal maximum size crushed limestone sourced from Hindsville Quarry located in Hindsville, AR. Density, specific gravity, and absorption (ASTM C127) [77] tests were performed for each bulk batch of coarse aggregate used and are listed in Table 3.1. Fine aggregate was Arkansas river sand quarried in Van Buren, AR. Density, specific gravity, fineness modulus, and absorption (ASTM C128) [78] were performed for each bulk batch and shown in Table 3.2.

Table 3.1 – Coarse aggregate properties

Sieve	Batch #1		Batch #2	
	% Retained	% Passing	% Retained	% Passing
1.5"	0.0	100.0	0.0	100.0
1"	1.4	98.6	0.8	99.2
3/4"	13.3	85.3	22.1	77.1
1/2"	49.1	36.2	38.3	38.8
3/8"	16.0	20.2	19.1	19.8
#4	17.0	3.2	18.7	1.0
#8	1.5	1.7	0.5	0.5
Pan	1.7	0.0	0.5	0.0
Specific Gravity	2.67		2.62	
% Absorption	0.46		0.48	

Table 3.2 – Fine aggregate properties

Sieve	Batch #1		Batch #2	
	% Retained	% Passing	% Retained	% Passing
#4	2.4	97.6	0.0	100.0
#8	4.7	93.0	4.9	95.1
#16	9.6	83.4	9.3	85.9
#30	20.0	63.4	20.1	65.8
#50	46.3	17.1	52.0	13.8
#100	16.2	0.9	13.4	0.4
#200	1.1	0.2	0.3	0.1
Fineness Modulus	2.45		2.39	
Specific Gravity	2.64		2.64	
% Absorption	0.30		0.45	

The concrete mix designs used in this research can be seen in Table 3.3. Three w/c were tested for the BCSA cement concrete samples and were compared to PC concrete at a w/c of 0.42. A 1.0 fluid oz per 100 pounds of cement dose of 0.039 lbs/fl oz. (0.598g/ml) concentration citric acid solution was added to prevent rapid premature setting of BCSA cement concrete mixes. This is equivalent to 0.03% citric acid by cement weight. The citric acid solution was prepared by mixing 5 pounds of solid citric acid per gallon of water. Euclid Chemical Plastol SPC (for BCSA cement) and ADVA Cast 575 (for PC) high range water reducing admixture (HRWR) was added in various amounts depending on w/c to attempt to achieve consistent workability between mixtures and help produce smooth concrete surfaces required by DIC imaging. Ice was used on warm days (greater than 75 degrees Fahrenheit ambient temperature) to ensure consistency in fresh concrete temperature between mixtures.

Table 3.3 – Concrete mix designs

Cement Type	BCSA			portland
w/c	0.36	0.42	0.48	0.42
Cement (lbs./yd ³)	889	714	625	611
Fine Aggregate (lbs./yd ³)	1001	1137	1274	1306
Coarse Aggregate (lbs./yd ³)	1700	1773	1700	1700
Water (lbs./yd ³)	320	300	300	257
HRWR*	1.0	0.5	0.4	1.0
Citric Acid*	1.0	1.0	1.0	0.0
Targeted 28 day strength (ksi)	12	11	10	7

* Fluid ounces per 100 pounds of cementitious material

Concrete for both uniaxial compression cylinders and flexural compression specimens were prepared by using a modified version of ASTM C685 [79]. Because of the rapid setting nature of BCSA cement, the specified mixing time of 8 minutes was reduced to 6 minutes for this research: 3 minutes mixing, 2 minutes resting (covered), 1 minute mixing. Slump (ASTM C143) [80], and temperature (ASTM C1064) [81] were performed for every mixture and air content using the pressure method (ASTM C231) [82] was performed for every initial trial batch. Companion cylinders for compression strength and modulus of elasticity testing were made according to ASTM C192 [83]. Cylinders for all tests in this research were left covered in the lab for at least 24 hours before being demolded and placed in a moist room at 73±3 degrees Fahrenheit and 100 percent humidity until the day of testing. Curing temperature is shown to have a large effect on strength gain in CSA type cements [84]. Moist room curing was preferred to limewater or tank curing for these materials as research has suggested that CSA specimens in limewater or other pore solutions showed a decreases in strength at later ages [85]. On testing day, cylinder ends were ground plane on an end mill grinder to ensure uniformity of the ends and to avoid needing to use neoprene end caps or sulfur caps per ASTM C39 [86]

3.2 Uniaxial Compression Cylinders

For each proposed w/c, 21 cylinders were fabricated and prepared for compression testing following the method described in section 3.1: 3 cylinders for each testing age (3 hours, 1 day, 3-day, 7-day, 28-day, and 6 month) and 3 extras. At least one 6 in diameter cylinder was made for each of the three w/c to be tested at 28 days. On each day of testing, three cylinders were removed from the controlled curing environment, dried of excess moisture, and one half of the cylinder wall for each cylinder was painted with 1-2 layers of matte white enamel spray paint. A 0.007 in. dot size random speckle pattern was printed onto each 4in. diameter cylinder in 2-3 overlapping layers using a custom inkpad and black ink as shown in Figure 3.1. Each 6 in. diameter cylinder received a 0.026 in. dot size random speckle pattern applied in the same manner as shown in Figure 3.2.

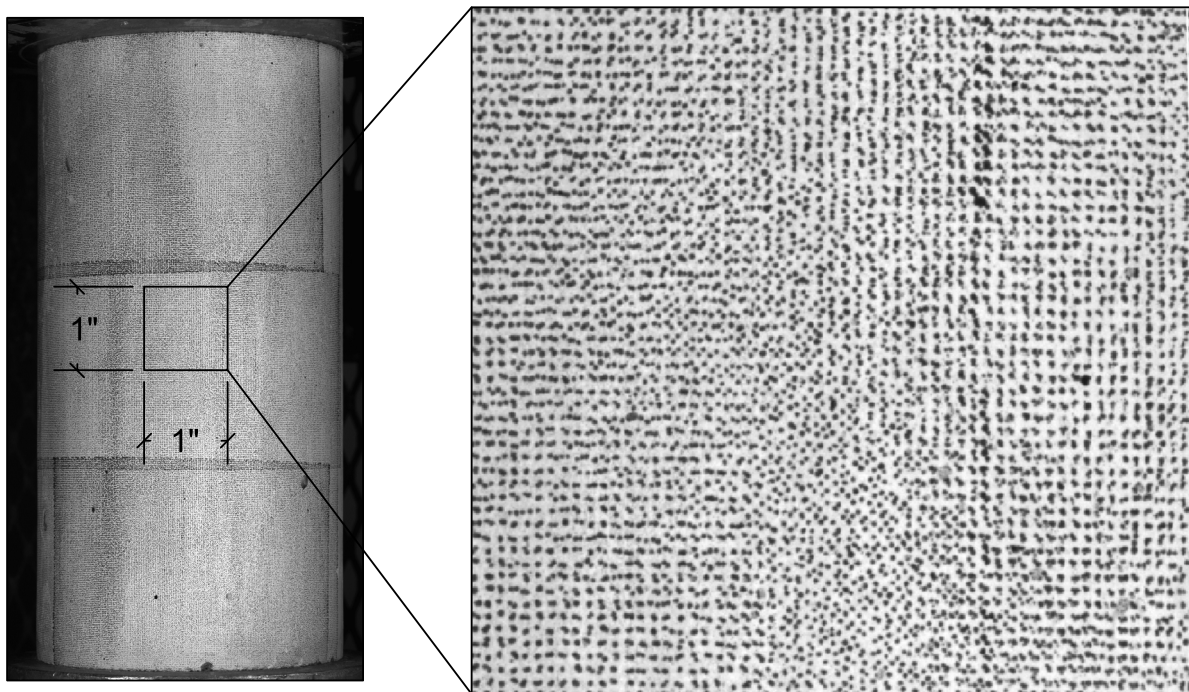


Figure 3.1 – Speckle pattern and density for 4in. diameter cylinders

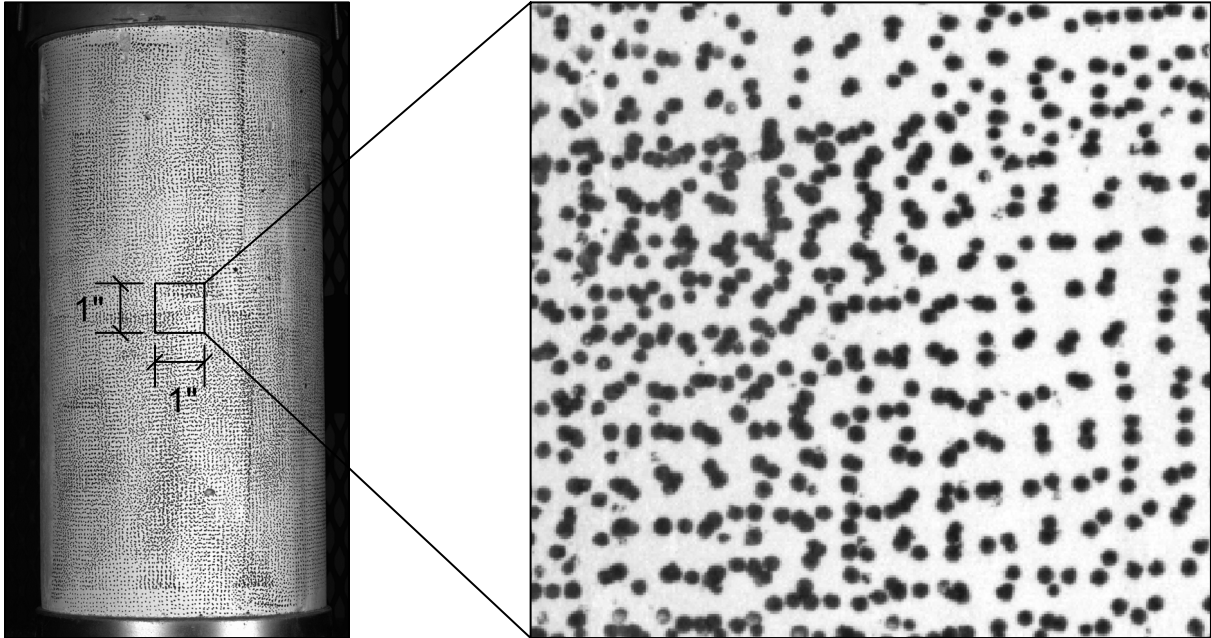


Figure 3.2 – Speckle pattern and density for 6in. diameter cylinders

Each cylinder was then placed into the center of a Forney axial compression testing machine. The DIC system cameras were outfitted with 35 mm lenses, situated roughly 6 in. apart and 3 ft from the cylinders. No significant out of plane movement was expected to occur, therefore, the lens apertures were opened to roughly 5.6 stops to allow more light to enter the camera lenses. Two large 120 W LED studio lamps were placed as close as possible to the cylinder without impeding camera view. Ample, diffused, and consistent lighting is required to increase the contrast of the speckle image and reduce the shutter speed of the cameras, producing sharper images for post processing. Higher contrast of speckling and sharper images, results in less projection error in post processing [87]. The camera setup can be seen in Figure 3.3. Cameras were always calibrated once prior to testing the first cylinder on any given testing day. DIC pictures were taken at a frequency of two Hz and started recording data a few seconds before the start of compression testing. The cylinder was loaded at a constant 35 ± 7 psi per

second with a preload of 1000 lbs. (ASTM C39) [86]. Load data from the Forney was recorded at a variable sample rate of roughly 33 hertz.



Figure 3.3 – DIC uniaxial strain camera setup

Due to the different frequency rates of data supplied by the two recording computers, the Forney data had to be truncated and resampled to match the DIC dataset using a MATLAB script as shown in Appendix C. This script also smoothed the strain dataset and reported maximum compression strain, compression strain limits used for calculating MOE and MOE based on the combined datasets. The script used a running mean of five values to smooth the strain dataset and remove some of the noise introduced from the cameras. This modified dataset was only used to give a more accurate estimation of MOE. All graphs and max strain values used the raw, unmodified data output from the DIC software. Additional details of this script are included in Appendix B.

An additional set of nine 0.42 w/c 4x8 in. cylinders were made to be able to compare calculated MOE values from DIC results with values obtained from a traditional MOE compressometer for concrete cylinders and a LVDT (ASTM C469) [39]. Cylinders were first cleaned, painted, and speckled as previously described and were first tested in accordance with ASTM C469 using a compressometer and LVDT to find an average MOE, then were broken without the ring following standard compression testing procedure to find MOE with DIC software. This was done to ensure results from DIC software closely followed results from traditional methods.



Figure 3.4 – Compressometer MOE method setup per ASTM C469

3.3 Flexural Compression Specimens

3.3.1 Specimen Fabrication

A modified version of a flexural compression specimen utilized by Mertol et. al.[58] was used for this research. For feasibility of testing using available equipment, a specimen with a smaller cross-sectional area was fabricated: reducing a proposed 9 in. square section size, down to 5.5 in. square and later 6 in. square.

Following Mertol et. al., 10 in. square steel tubes confine the top and bottom of the specimen and allow for the transfer of moment from the steel moment arms to the center of the concrete specimen. These steel tubes or boxes are made with 10 in. wide 1/4 in. thick A36 steel plate. Front and back plates were 10 in. square and had four 1-1/4 in. bolt holes drilled with a magnetic drill and annular bit (Figure E.9) in a pattern that mirrored the moment arm back plate bolt hole orientation (Figure E.3). Side plates were 10 in. tall and 9 in. wide (Figure E.10). All plates were welded together using 1/4 in. fillet welds and E70 electrode along the interior edges of the box as shown in Appendix C Figure E.8.

Using prefabricated 10 in. by 10 in. by 4 ft beam molds, two steel boxes were placed with 20 in. of clear space between, and in the same orientation with the opening of the box coincident with the centerline of the beam molds as shown in the nominal dimensions represented in Figure 3.5. Eight 10 in. long 1-1/4 in. nominal PVC pipes were cut and placed concentric with the centerline of each bolt opening of the two steel boxes. These plastic pipes were used to pre-form a duct for a threaded rod to pass through when attaching the moment arms. To prevent the plastic pipes from moving, eight 10 in. long 1 in. nominal diameter wooden dowel rods were placed inside the pipes, which forced the pipes to keep concentricity with the holes in the steel box plates. After fabricating six specimens, it was determined that removing the wooden dowel rods

after placing the concrete posed a risk of damaging the specimen. Therefore, a change was made to increase the size of holes in the steel boxes to 1-5/16 in. diameter. This allowed for a 10 in. long PVC pipe to pass completely through both holes as shown in Figure 3.9. This method resulted in a compression fit of the pipe around the steel holes, however it also required that every PVC pipe be turned on the lathe to remove roughly 1/32 in. material to fit properly.

Four 20 in. wooden blocks were used to reduce the section size of the specimen from 10 in. (width of the beam molds) to 5.5 in. These wood pieces were cut from a nominal 2 in. by 10 in. board and fastened to nominal 3/4 in. plywood board. The top and bottom edges of the section-reducing wood pieces were beveled at a 45-degree angle with the intention of reducing high stress areas at the sharp intersection with the steel boxes and unreinforced section (Figure 3.6). The wood faces of the formwork exposed to fresh concrete was sanded several times with 80 and 180 grit sandpaper and received 5-6 coats of polyurethane wood sealant. After using the wooden spacers several times, it was determined that there was too high of a risk of damaging either the wooden forms or the concrete specimen during demolding. An alternative section reducing method was developed using 2 in. thick foam insulation which was cut off the specimen during demolding. Foam sections were attached using wood screws, used the same 45-degree angle to reduce corner stresses and all seams were covered with masking tape prior to placing concrete. Foam formwork can be seen in Figure 3.7. All formwork surfaces exposed to fresh concrete other than the steel boxes were prepared with 5-6 coats of concrete release agent at least 24 hours before fresh concrete placement. Beam formwork was set vertical and leveled using bubble levels and a 1/8 in. steel plate was fastened to the bottom of the formwork using 1/4 in. carriage bolts as shown in Figure 3.8.

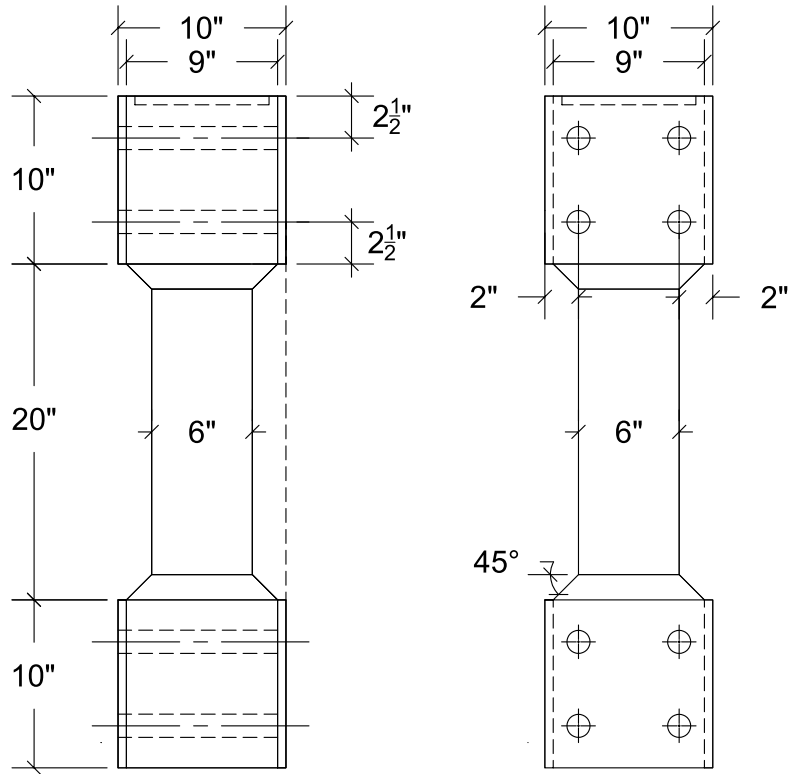


Figure 3.5 – Specimen nominal dimensions



Figure 3.6 – Wooden cross-section reducing formwork



Figure 3.7 – Foam insulation cross-section reducing formwork



Figure 3.8 – Upright formwork with bottom steel plate

Concrete was mixed as described in Section 3.1 and was placed into the upright formwork in four equal lifts of 10 in. per lift. Each lift was vibrated for 5-10 seconds with an 1800 W vibrator. It was found after making several specimens that it was more effective to achieve proper consolidation by using eight lifts of roughly 5 inches per lift. On the top surface of the specimen the concrete was finished 1/2 in. below the top edge of the steel box and an 8.5 in. by 8.5 in. by 1/2in. A36 steel plate was placed on the top surface of the concrete to make a smooth interface for applying axial force to the specimen. Specimens were left to set in ambient temperature conditions for 20-24 hours and demolded from the formwork to be placed in a controlled curing environment until testing. The controlled curing environment was the same as described in Section 3.1.

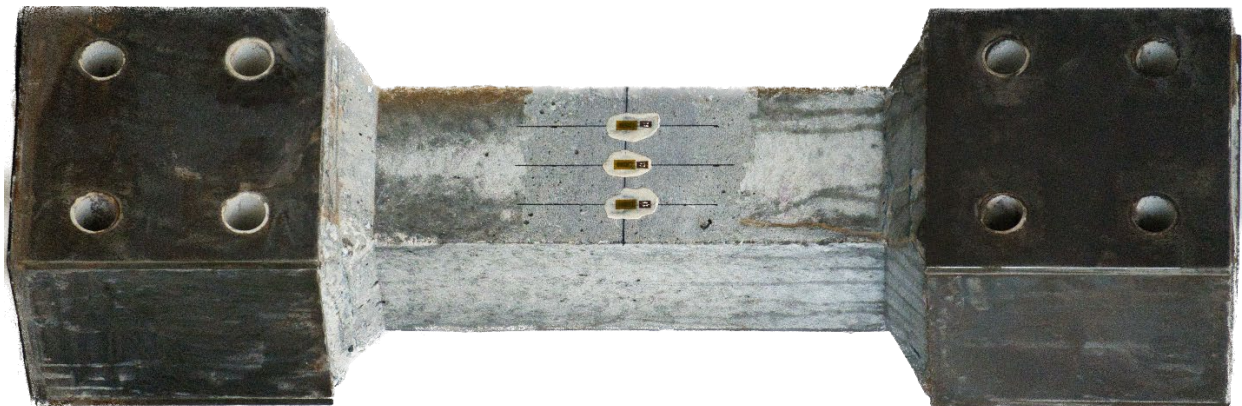


Figure 3.9 – Concrete flexural compression specimen

3.3.2 Custom Equipment for Test Loading Setup

3.3.2.1 Moment Arms

Two moment transfer arms were manufactured that closely resemble those described in Mertol et. al. with some minor changes. These two steel beams transfer and transform axial compression force from a through hole ram and prestressing strand into an eccentric loading condition to apply constant moment to the unreinforced concrete specimen as described in Section 2.4.2. Each arm consisted of two 24 in. long C8X11.5 steel A992 sections separated by 1

in. Two, 24 in. long, 10 in. wide 1/2 in. thick steel plates were welded to the top and bottom of the channel sections (Figure E.4). The webs of the channels were stiffened by three 1/2 in. steel plates spaced at 6 in. on center (Figure E.5). On the back edge of the arm a 10 in. square 1 in. thick base plate (Figure E.3) was welded to all terminal exterior edges of the channel and plates as shown in Figure E.7. This back plate was modified from Mertol et. al. to only have four bolt holes instead of six. It was determined that the middle two threaded rods were negligent in the transfer of forces since they lie on or near the neutral axis of bending.

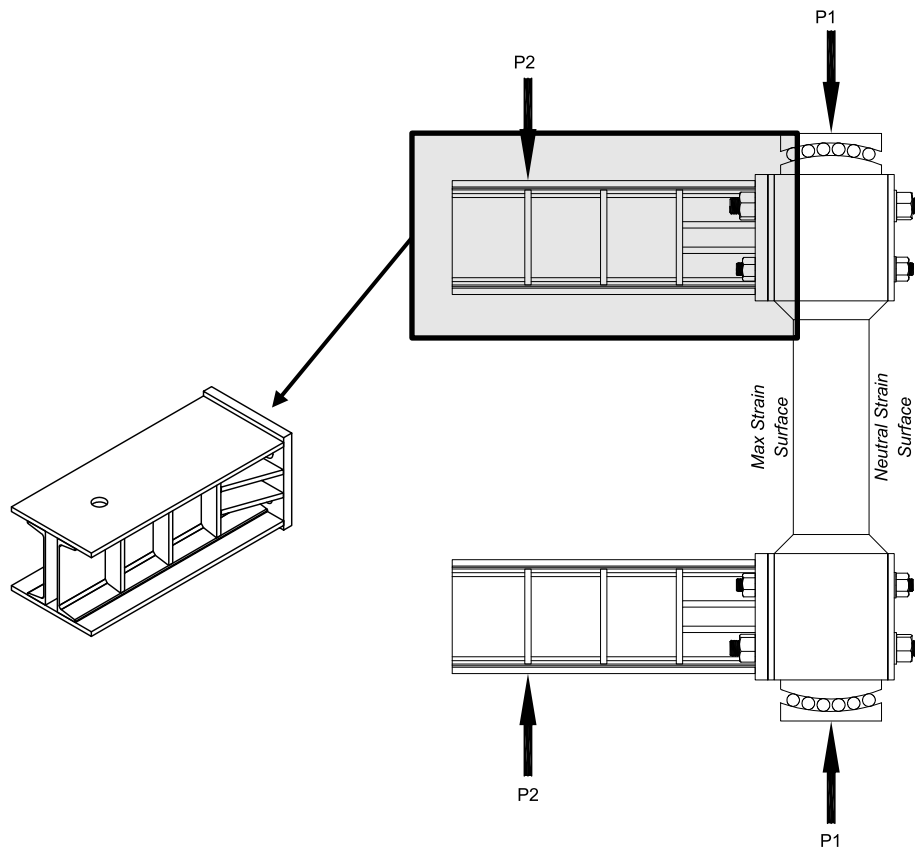


Figure 3.10 – Moment arms for specimen

3.3.2.2 Rollers

Specialized rollers were manufactured to similar specifications as in Mertol et. al. These rollers were placed at the top and bottom of the concrete section to transfer the full axial (P1)

load without inhibiting the rotation of the specimen caused by load P2 and the moment arms.

These rollers were made from S7 tool steel and were completed to the dimensions and specifications shown in Figure E.11 through Figure E.16. The radius of curvature to the rollers is 13 in. which shifts the center of rotation of the specimen to the start of the unreinforced concrete section as shown in Figure 3.11. The curved roller plates were not hardened and had minor deformations over the course of testing due to the high, concentrated loads.

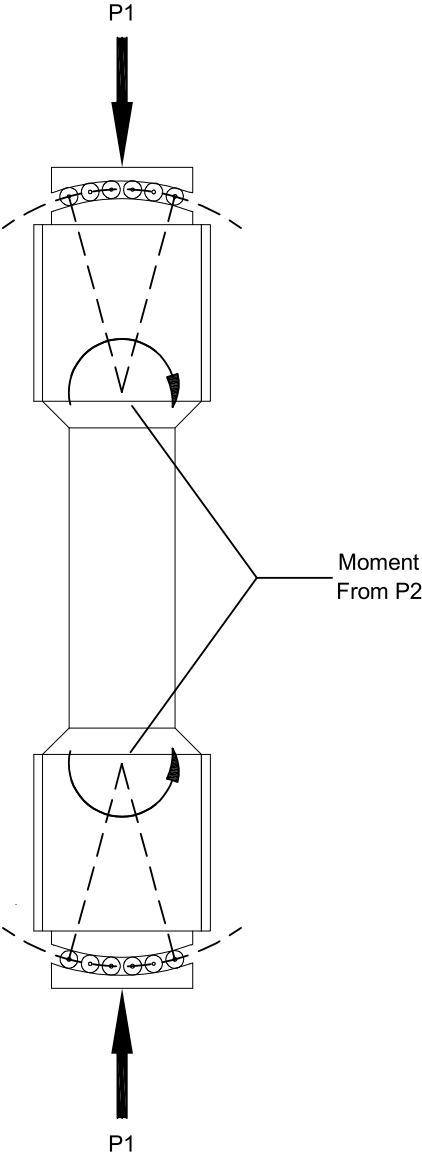


Figure 3.11 – Roller rotational offset

3.3.3 Test Setup

To resist the axial and flexural loads applied to the specimen, a specialized system of floor restraints intended to resist shear, moment, compression, and tension loads was used. On either side of the specimen, the axial force was resisted by two 8 ft long W14X120 A992 steel beams each bolted to two triangular shear resisting fixtures. Each fixture was post tensioned to the floor using two 1.75 in. diameter 150 ksi all-thread rods with a post tensioning force of roughly 109.1 kips per rod. This achieved an estimated effective shear resisting system of 361 kips assuming a coefficient of static friction of 0.8. Each shear block was attached to the spreader beam using four 1 in. diameter all-thread rods with the intention of resisting rotation in either flange of the beam. The web and flanges of each beam were reinforced with two 3.5 in. dia. by 12.5 in. long steel pipes placed between the flanges on either side of the web at the location of load application.

The two spreader beams were placed 8 ft apart to provide adequate room for the 40 in. specimen, rollers, hydraulic ram, and expected specimen rotation. Two additional 10 in. long A36 steel spacers were fabricated to make up for the remaining distance between floor restraint locations. Between the spreader beams, a 2 in. thick wooden flooring system was erected to lift the specimen high enough for the center of axial force through the specimen to act through the center of the webs of the spreader beams. The main axial ram used to apply load “P1” was a 300 kip double acting Enerpac ram attached rigidly to a custom spacer which was attached to the spreader beam. To prevent lateral movement of the ram, two custom made eyebolts were attached to the sides of the ram and fastened to the floor using 8 in. turnbuckles. A HBM P3MB pressure transducer was attached in-line with the extension hydraulic line of the ram to determine force P1.

The top and bottom section of the specimen, encased in a steel box, were attached to the custom manufactured moment arms previously described in Section 3.3.2. Each moment arm was attached using two 1-1/4 in. diameter 80ksi threaded rods and two 1 in. diameter 60ksi threaded rods. The larger diameter rods were positioned on the very top and bottom of the section because they transferred a tension force from the moment arms into the concrete specimen. Between the ram and lower spacer, one roller was placed on either end of the specimen with the center radius point of curvature of the roller acting through the specimen.

A 120 kip through hole single acting Enerpac hydraulic ram was rigidly attached to the top moment arm. Using a 6 ft long 0.6 in. diameter prestressing strand, two chucks, and a 100 kip through hole Geokon load cell the arms were coupled together, and the chucks were set.

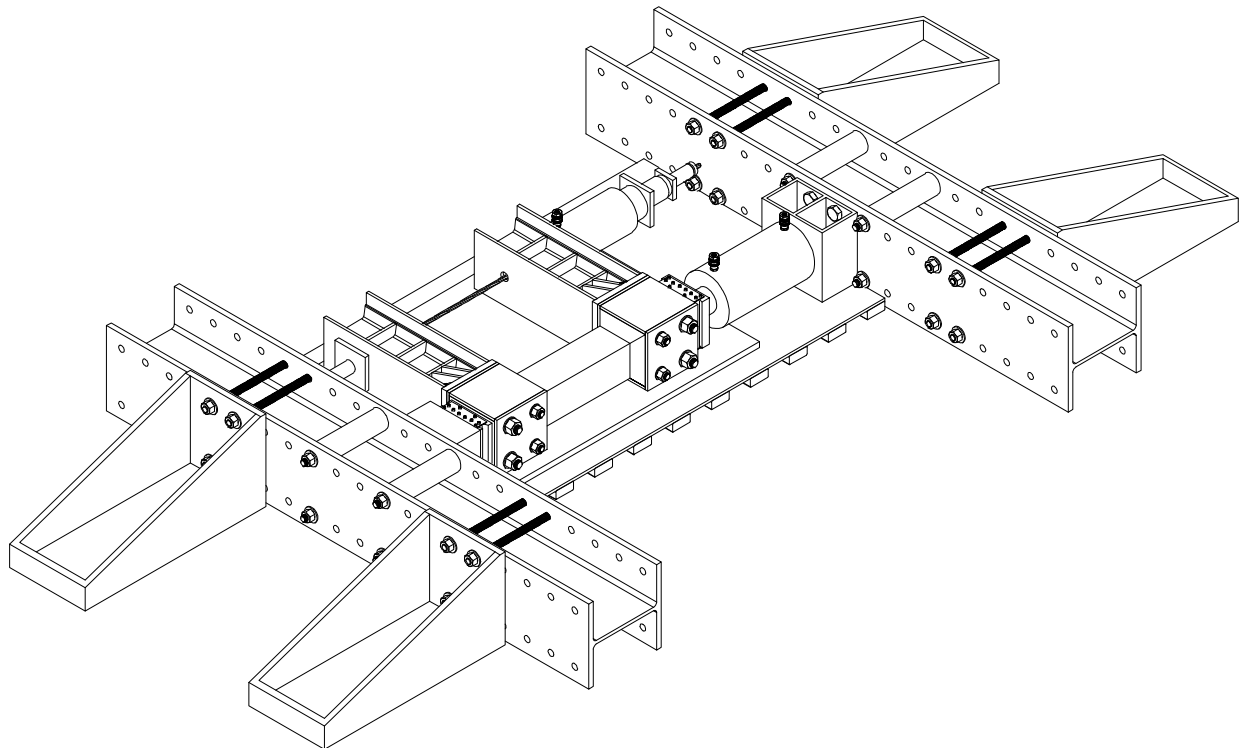


Figure 3.12 – Isometric view of flexure test setup

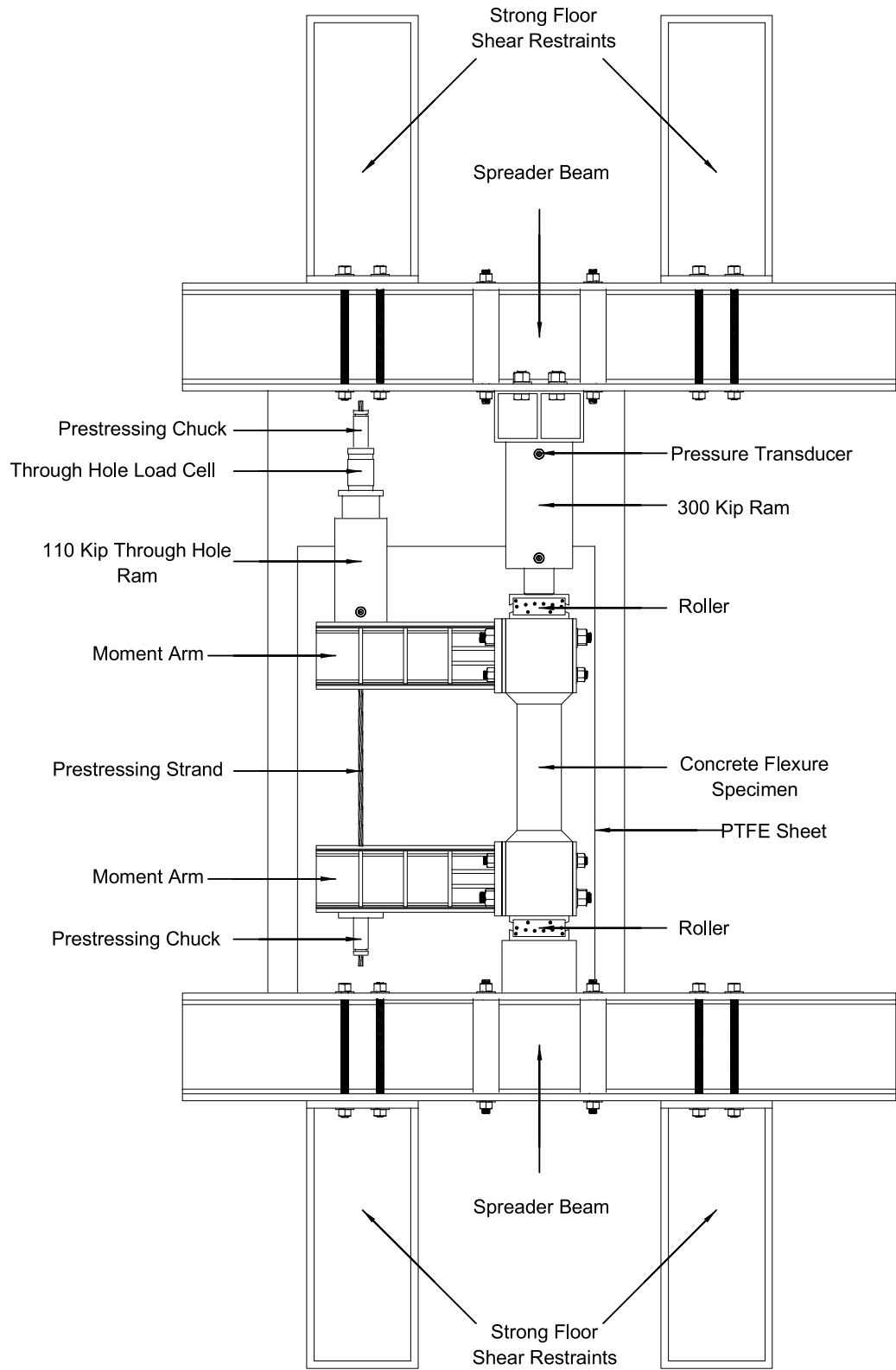


Figure 3.13 – Plan view of flexure test setup

The specimen was prepared for strain gauge attachment by lightly grinding the surface of the “neutral strain” and “maximum strain” faces with a diamond cup angle grinder wheel. These surfaces were then cleaned with compressed air, a damp cloth and finally with isopropanol alcohol. Two Bridge Diagnostics strain gauges were attached to the middle of the “max strain” face and two on the “zero strain” face of the specimen using 410 Loctite Glue and 7452 Loctite Accelerator on the top and bottom edges of the pads and Devcon wet surface repair two-part epoxy on the middle two thirds of the pads. Verification of the gauge factor calculation, and attachment method of the Bridge Diagnostics strain gauges was obtained by comparing the values output by four of these gauges with four HBM 10mm foil strain gauges placed underneath the bridge gauges using HBM X60 compound epoxy all on the same specimen. This specimen was loaded in compression axially and values between the two gauges were evaluated. It was determined that results from the Bridge Diagnostics were unreliable either due to the gauge factor, attachment method used, or some other factor. The final 14 specimens included in Section 4.2 only include data from specimens outfitted with HBM 10mm foil gauges, and the attachment method described above. Three foil strain gauges on the maximum strain side and three on the neutral strain side. Linearly variable differential transformers (LVDTs) were placed at the top and bottom of the specimen in the center of the steel plate opposing the moment arms to detect any significant unwanted lateral movement of the specimen during testing and to help establish the location of force (P1 and P2) application relative to the specimen.

The pressure transducer, load cell, and LVDTs were wired to a HBM MX840B data acquisition unit (DAQ) and data was recorded using Catman software. Strain gauges were recorded through a separate HBM MX1615B DAQ and logged using the same Catman software. Data from all sensors recorded in Catman were sampled at 20 hertz.

To prepare the specimen for DIC analysis, the top “variable strain” face of the specimen was cleaned with a damp washcloth and compressed air to be prepared for paint and spray painted with a matte white enamel paint in two layers. After the white enamel layer, this face was painted with a speckle pattern of 0.026 in. size dots in 2-3 overlapping layers using a prepatterned rubber stamp and black ink. Speckle pattern and density is shown in Figure 3.15. A tripod with an inverted head and cameras facing downward toward the specimen was used with the cameras situated 8 in. apart and roughly 20 in. directly above the specimen. 16 mm camera lenses were used. The scene was adequately lit using two large 120 W LED studio lamps. Data from the cameras was monitored across the section in real time during testing to determine when to increase moment from load P2. Data from the DIC system was monitored in real time at 2 hz and saved at the same frequency.

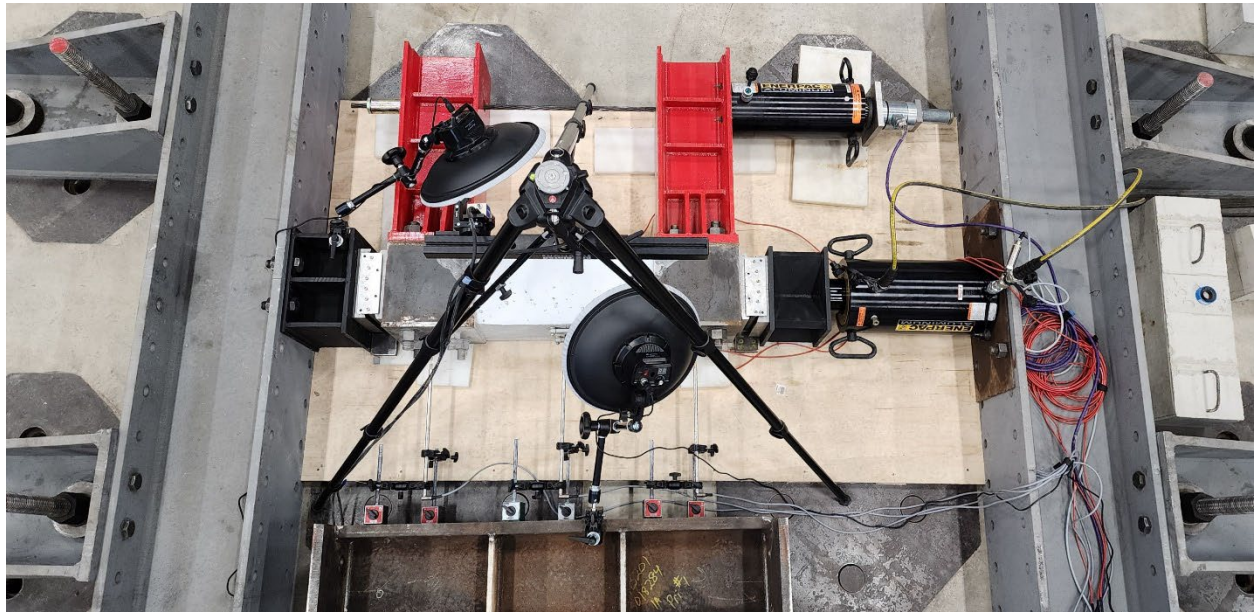


Figure 3.14 – DIC camera setup for flexural compression specimens

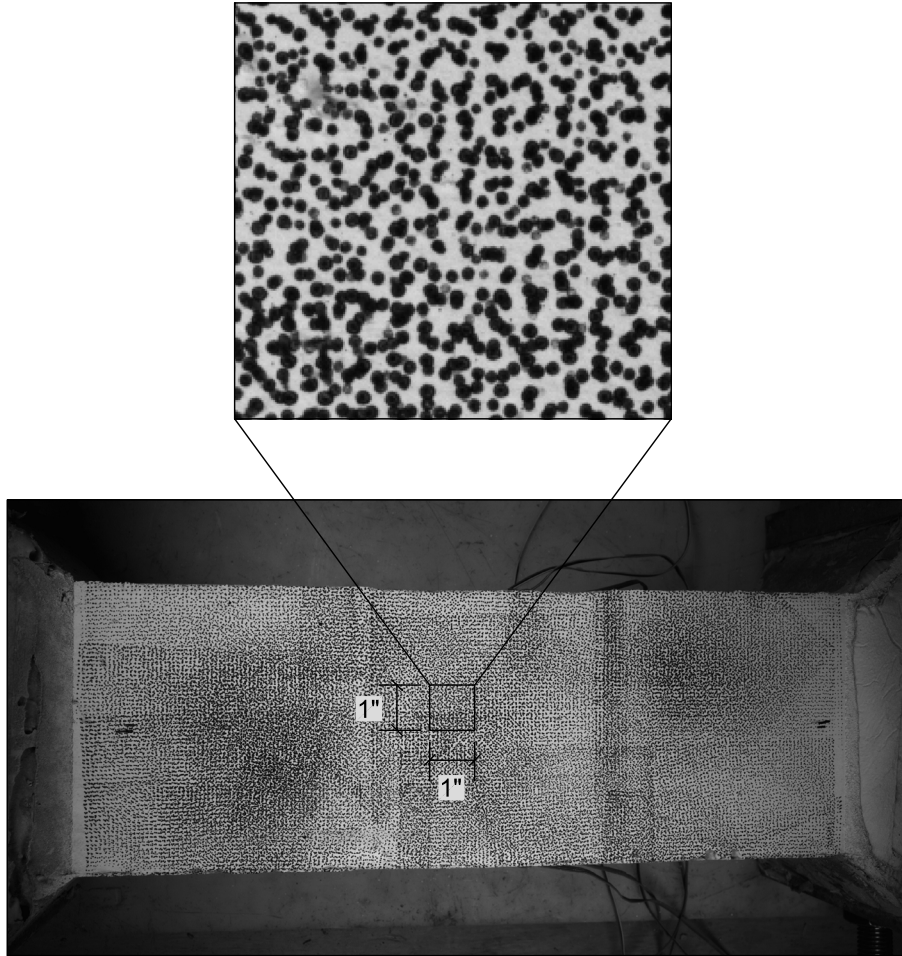


Figure 3.15 – Speckle pattern and density for flexural compression specimen

3.3.4 Testing method

Prior to testing the flexure specimens, three 4 in. diameter companion cylinders were tested for compression strength (ASTM C39 2018). The specimen width and depth were measured in three locations and averaged. For the flexure specimen, Catman recording software and DIC software were started at the same time using verbal cues. A 30 kip compression preload (P1) was applied to the specimen while blocks and screws inhibiting rotation of the rollers were removed. Compression load, P1, was applied using a hydraulic hand pump. Load P1 was increased slowly throughout the test generally around 20 kip per min. During loading, real-time data from both strain gauges on the “zero strain” face, and digital strain gauges in the DIC

software were used to determine when to increase load P2 to reduce the compression strain on the zero-strain face.

3.3.5 Stress Calculations

Each flexural compression specimen has unique strength characteristics, dimensions, and loading rates that will alter the way stress calculations are performed. Due to nonuniform stress distribution in the specimen, stress calculations were performed by calculating the area under the generalized stress curve described in Figure 2.9 for each time iteration in testing. Parameters k_1 , k_3 , and k_2 were calculated for each specimen using equilibrium equations established by Hognestad [4] as shown below:

$$C = k_1 k_3 f'_c A_c \rightarrow k_1 k_3 = \frac{C}{f'_c A_c} = \frac{P_1 + P_2}{f'_c A_c} \quad \text{Equation 3-1}$$

$$\sum M_o = 0 = P_1 a_1 + P_2 a_2 - C(c - k_2 c) \quad \text{Equation 3-2}$$

$$\rightarrow \frac{P_1 a_1 + P_2 a_2}{c} = (P_1 + P_2)(1 - k_2)$$

$$\rightarrow k_2 = 1 - \frac{P_1 a_1 + P_2 a_2}{(P_1 + P_2)c}$$

To calculate total average internal stress in the specimen, two assumptions were made as theorized by Hognestad [4]. First, strain remains linear across the test section. And all compressive concrete fibers throughout the specimen can be represented by the same equation, where stress is a function of strain. Applied stresses from axial and moment loading to the concrete section are as follows:

$$C = \frac{A_c}{\epsilon_c} \int_0^{\epsilon_c} F(\epsilon_x) d\epsilon_x = P_1 + P_2 = f_{oc} A_c \quad \text{Equation 3-3}$$

$$M = \frac{A_c c_c}{\varepsilon_c^2} \int_0^{\varepsilon_c} F(\varepsilon_x) \varepsilon_x d\varepsilon_x = P_1 a_1 - P_2 a_2 = m_{oc} A_c c_c \quad \text{Equation 3-4}$$

Where compression stress from axial and moment loads are represented as follows:

$$f_{oc} = \frac{C}{A_c} = \frac{P_1 + P_2}{A_c} \quad \text{Equation 3-5}$$

$$m_{oc} = \frac{M}{c_c A_c} = \frac{P_1 a_1 + P_2 a_2}{c_c A_c} \quad \text{Equation 3-6}$$

And tension stress from axial and moment loads are represented as follows:

$$\sigma_{ft} = \frac{T}{A_t} \quad \text{Equation 3-7}$$

$$\sigma_{mt} = \frac{T a_3}{c_t A_t} \quad \text{Equation 3-8}$$

Differentiating and rearranging equations Equation 3-3 and Equation 3-5 and including Equation 3-7, total stress response from axial force can be simplified as:

$$\sigma_f = \varepsilon_c \frac{df_{oc}}{d\varepsilon_c} + f_{oc} - \sigma_{ft} \quad \text{Equation 3-9}$$

Differentiating and rearranging equations Equation 3-4 and Equation 3-6 and including Equation 3-9, total stress response from moment force can be simplified as:

$$\sigma_m = \varepsilon_c \frac{dm_{oc}}{d\varepsilon_c} + 2m_{oc} - \sigma_{mt} \quad \text{Equation 3-10}$$

Where $\frac{df_{oc}}{d\varepsilon_c}$ and $\frac{dm_{oc}}{d\varepsilon_c}$ can be closely approximated by finite differences of each timestep of data

collected: $\frac{\Delta f_{oc}}{\Delta \varepsilon_c}$ and $\frac{\Delta m_{oc}}{\Delta \varepsilon_c}$

P1, P2, and ideal locations of a₁, a₂, and c are shown in Figure 3.16. Distances a₁ and a₂ are the distances between load points P1 and P2 perpendicular to the neutral axis. Distance c_c is the perpendicular distance between the most extreme compression fiber of concrete and the

neutral axis. The angle and location of the neutral axis was determined by plotting the linear strain distribution along the three faces of the sample where strains were measured and interpolating the zero points. A_c is the area of concrete in compression corresponding to the total area with negative (compression) strain. A_t is the area of concrete in tension, calculated as the total concrete area minus A_c . Distance c_t is the perpendicular distance between the most extreme tension fiber and the neutral axis. Distance a_3 is the perpendicular distance between the resultant tensile force and the neutral axis. Because tensile forces expected in the specimen are relatively small, and do not exceed the rupture stress of concrete, the resultant tensile stress was calculated using the product of the measured tensile strain values and the previously measured MOE value. This method assumes that concrete exhibits the same stress-strain slope in tension as it does in compression which is a conservative assumption for concrete at an early age [88]. Finite difference methods used to calculate total stress in the concrete section are greatly influenced by accuracy and consistency of data collection methods. Compounding experimental sources of error can be caused by discontinuous application of load or large changes in a_1 , a_2 , and c_c [4]. To produce reasonable stress-strain graphs for flexural compressive specimens, an average of 30 data points (3 seconds) was used in the finite differences model. Stress values were then smoothed with an exponential smoothing with a damping factor of 0.91. If there were any significant spikes in the stress after exponential smoothing, each individual spike was replaced with an average value of the data points before and after. Total compression stress calculated in the concrete section was an average of the total stress from axial load and total stress from moment loads.

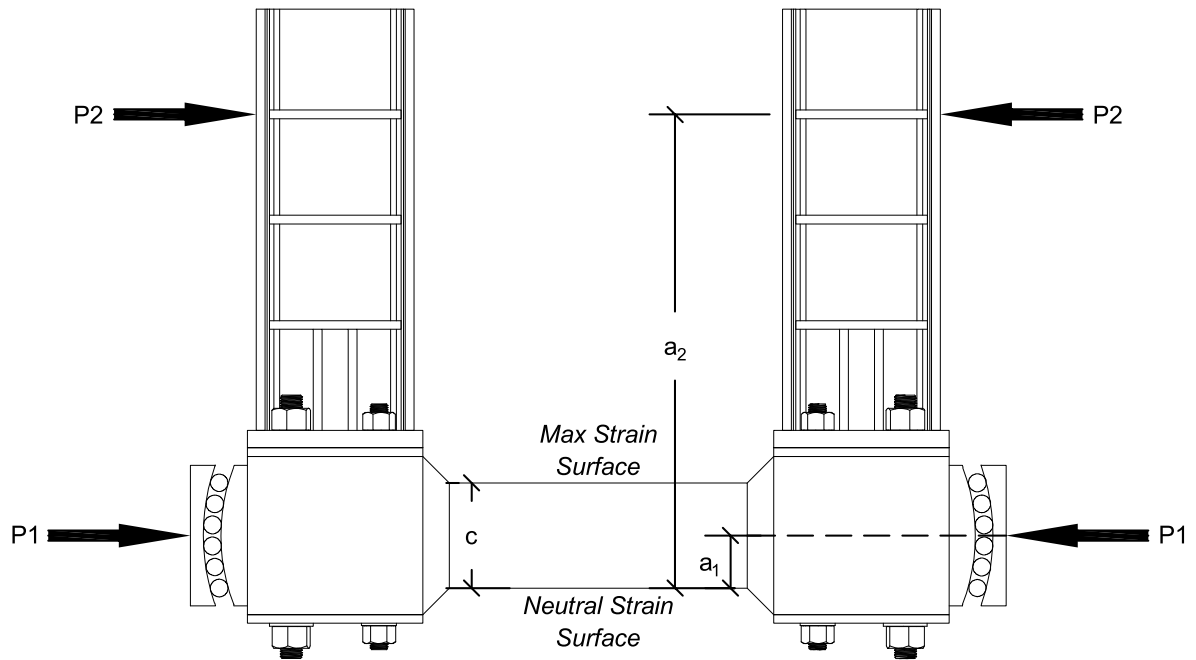


Figure 3.16 – Loads on flexure specimen

4 Experimental Results and Discussion

All concrete was made in accordance with the methods described in Section 3.1. Fresh concrete property results for uniaxial compression cylinders can be seen in Table 4.1. 0.36 and 0.42 w/c PC and BCSA cement concrete DIC cylinder specimens as well as all trial batch mixes were made using bulk batch #1 coarse and fine aggregates. The flexural compression specimens and 0.48 w/c DIC cylinder specimens were made using bulk batch #2 coarse and fine aggregates and associated properties from Table 3.1 and Table 3.2. Ambient lab temperatures ranged from 40-80 degrees Fahrenheit, and ice was used as partial replacement to water on warm days to obtain a mix temperature range of 55.3 to 76.2 °F with the average temperature of mixes being 65.9 °F. The average slump was 5 in. with a range of 2-7.

Table 4.1 – Uniaxial compression cylinder fresh concrete and strength results

Batch Name	Cement	w/c	Citric Acid (oz/100lb cm)	HRWR (oz/100lb cm)	Slump (in)	Mix Temp (°F)	7 day Strength (ksi)	28 day Strength (ksi)
B3-36	BCSA	0.36	1.0	1.0	5	76.2	9.51	10.61
B2-42	BCSA	0.42	1.0	0.5	6.25	67.3	7.75	8.78
B4-48	BCSA	0.48	1.0	0.4	6.5	64.2	5.56	6.03
PB2	PC	0.42	0.0	2.0	5.5	69.3	5.98	6.90

Table 4.2 – Flexural compression specimen fresh concrete and strength results

Batch Name	Cement	w/c	Citric Acid (oz/100lb cm)	HRWR (oz/100lb cm)	Slump (in)	Mix Temp (°F)	7 day Strength (ksi)	28 day Strength (ksi)
B10-36	BCSA	0.36	1.0	1.0	2	69.3	11.32	12.36
B14-36	BCSA	0.36	1.0	1.0	7	62.3	11.54	12.09
B13-42	BCSA	0.42	1.0	0.5	4	69.2	10.56	11.37
B15-42	BCSA	0.42	1.0	0.5	2.75	65.4	10.68	11.57
B11-48	BCSA	0.48	1.0	0.4	6	61.2	7.80	9.53
B12-48	BCSA	0.48	1.0	0.4	7	55.3	7.84	9.48
PB3	PC	0.42	0.0	2	3.25	65.2	7.53	8.93

Measured maximum stress (f_c') for uniaxial compression specimen batches ranged from 3.1 to 11.3 ksi with measured MOE between 2239 to 4901 ksi. Increasing the w/c by 0.06 between mixes resulted in a 1.5 to 2 ksi increase in compression strength regardless of testing age as seen in Figure 4.1. All three w/c mixes of BCSA cement concrete gain similar proportions of their 28 day strength with 52-59 percent of strength gained within the first three hours, 69 to 72 percent strength gained in the first day and 71 to 78 percent strength gained in the first three days. Six-month strength is 100 to 110 percent of 28 day strength.

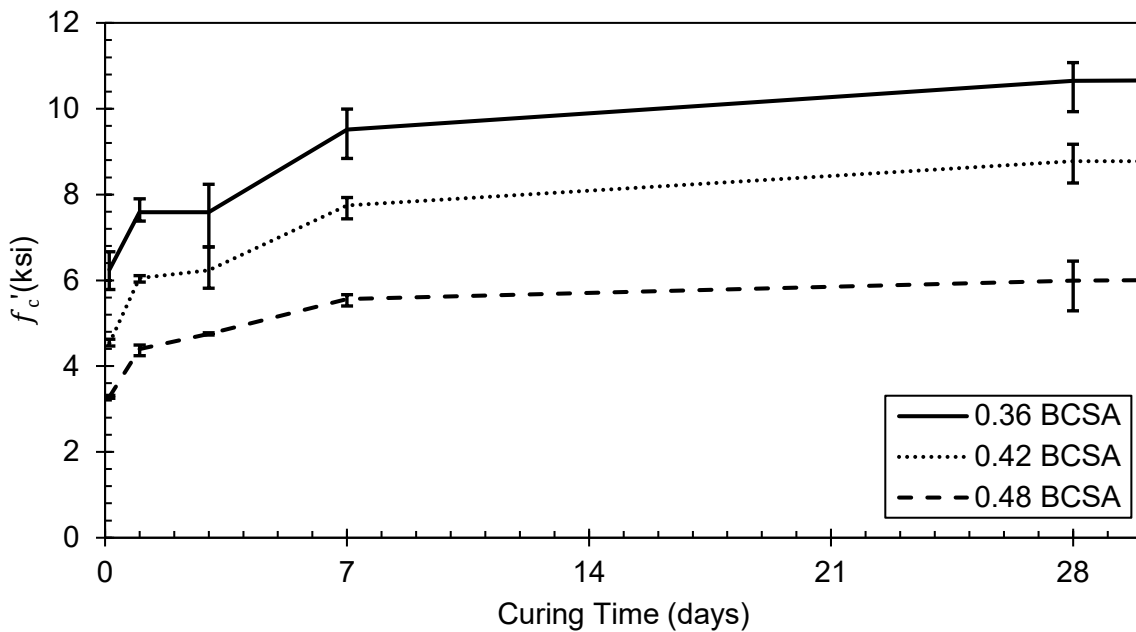


Figure 4.1 – Compression strength development of BCSA cement mixtures over time

4.1 Uniaxial Compression Cylinders

A total of 64 uniaxial compression concrete cylinders were made and tested for stress-strain testing. Of those, 59 specimens had usable data. Three of the cylinder specimens had unusable data because the DIC camera system stopped recording images during the test. The other two specimens had surface buildup that affected the results of DIC analysis. Of the 64 total

specimens, 6 were PC and the rest were BCSA cement concrete at various w/c. All cylinders for each w/c were cast from one batch of concrete to ensure consistency of results. Cylinders were tested with the methodology previously described in section 3.2. Table 4.3 includes data for each testing age as an average of three specimens, including the maximum stress (f'_c), uniaxial compression strain (ϵ'_c) correlating with f'_c , predicted MOE from ACI using equation 2-1 (E_{ACI}) and tested MOE (E_c).

Table 4.3 – Average uniaxial compression cylinder results

w/c	Age	f'_c (psi)	ϵ'_c	E_{ACI} (ksi)	E_c (ksi)
0.36 BCSA	3 Hour	6249	0.0024	4504	3475
	1 Day	7586	0.0022	4964	3402
	3 Day	7585	0.0018	4960	4253
	7 Day	9513	0.0023	5558	4178
	28 Day	10654	0.0024	5882	4713
	6 Month	11296	0.0024	6057	4901
0.42 BCSA	3 Hour	4536	0.0021	3839	2932
	1 Day	6053	0.0019	4435	3783
	3 Day	6234	0.0018	4498	3770
	7 Day	7746	0.0021	5016	4366
	28 Day	8775	0.0021	5339	3928
	6 Month	8738	0.0022	5328	4036
0.48 BCSA	3 Hour	3285	0.0016	3267	3254
	1 Day	4396	0.0018	3779	3217
	3 Day	4749	0.0018	3928	3133
	7 Day	5561	0.0017	4251	3995
	28 Day	5991	0.0017	4409	3795
	6 Month	6775	0.0017	4692	3867
0.42 PC	7 Day	5984	0.0018	4409	4590
	28 Day	6895	0.0022	4733	4133

DIC analysis of the uniaxial compression strains in 4 in. diameter cylinder specimens one half second prior to (left) and after failure (right) and an example of 6 in. long virtual strain gauge orientation and locations can be seen in Figure 4.2. Both virtual strain gauges and average

strain within a polygonal area were used to measure the compressive strain in the cylinder specimens.

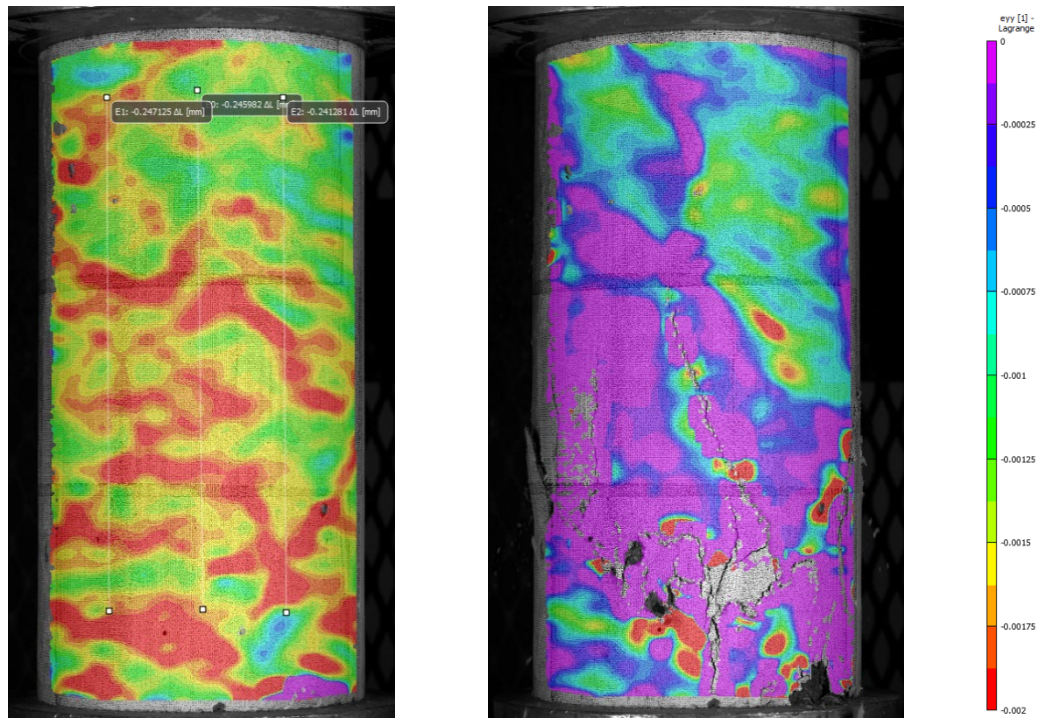


Figure 4.2 – Visualization of DIC strains in 4 in. diameter cylinder before and after failure

DIC uniaxial strain analysis of 6 in. diameter cylinder specimens was performed in the same manner as with 4 in. diameter specimens. Virtual strain gauges for 6 in. diameter cylinders were 10 in. long. An example of strain visualization before failure (left) and after failure (right) for 6 in. diameter specimens can be seen in Figure 4.3.

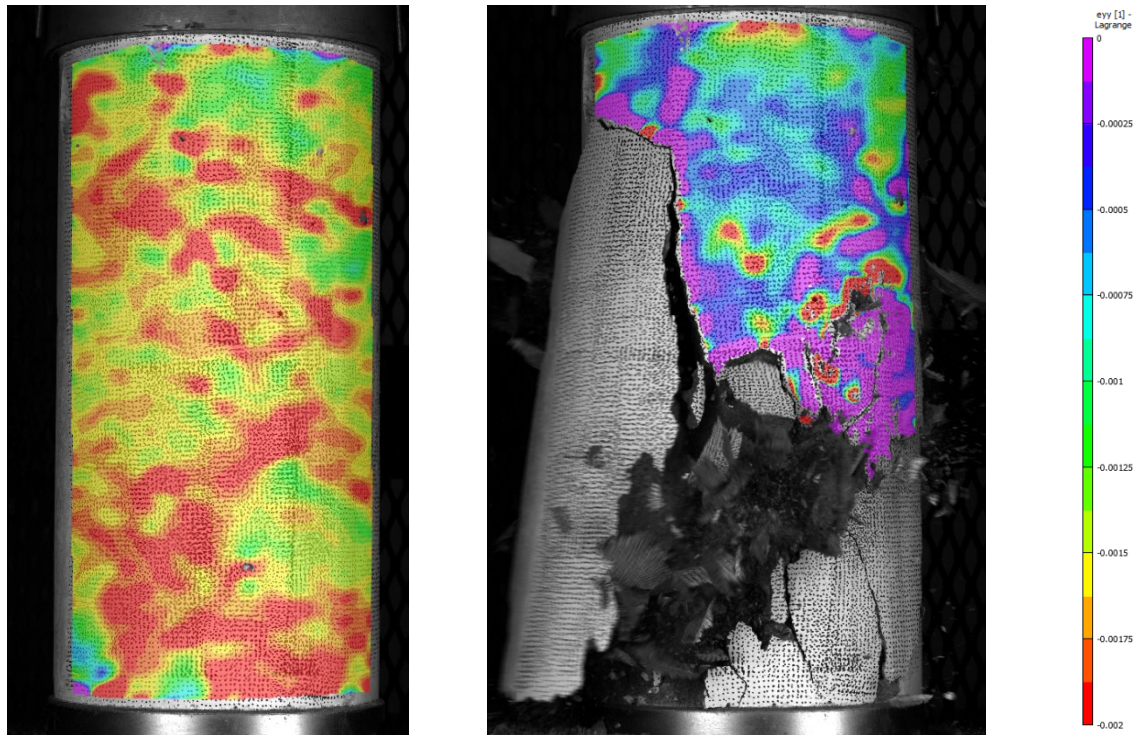


Figure 4.3 – Visualization of DIC strains in 6 in. diameter cylinder before and after failure

Representative stress-strain relationships at testing ages of 3 hours, 1 day, 3 days, 7 days, 28 days and 6 months were plotted for each of the three w/c and can be seen in Figure 4.4 through Figure 4.6. At earlier ages and at lower strengths, the slope of the portion of the stress-strain graph prior to 60% stress is lower than at older ages and higher strengths. Cylinders with maximum strengths over 6 or 7 ksi maintained linearity of the initial stress-strain slope for longer and often resulted in a brittle failure shortly after peak load with post peak strains of 0.00005 to 0.0001. Cylinders with lower strengths can experience up to 0.0005 additional strain after maximum stress before failure. The failure mode of cylinders stronger than 7 ksi often showed similarity to ASTM C39 fracture type 1. This suggests that the confining friction from the high normal force on the top and bottom of the specimen resisted lateral expansion of the cylinder ends as expected with end ground high strength concrete specimens. Cylinder strengths between 5 and 7 ksi often showed failure type 1 or 2 and cylinders weaker than 5 ksi had a type 3 failure

mode. Lower strength cylinders with type 3 failure modes suggest concrete internal lateral stresses exceeded the tensile strength of the concrete matrix causing failure.

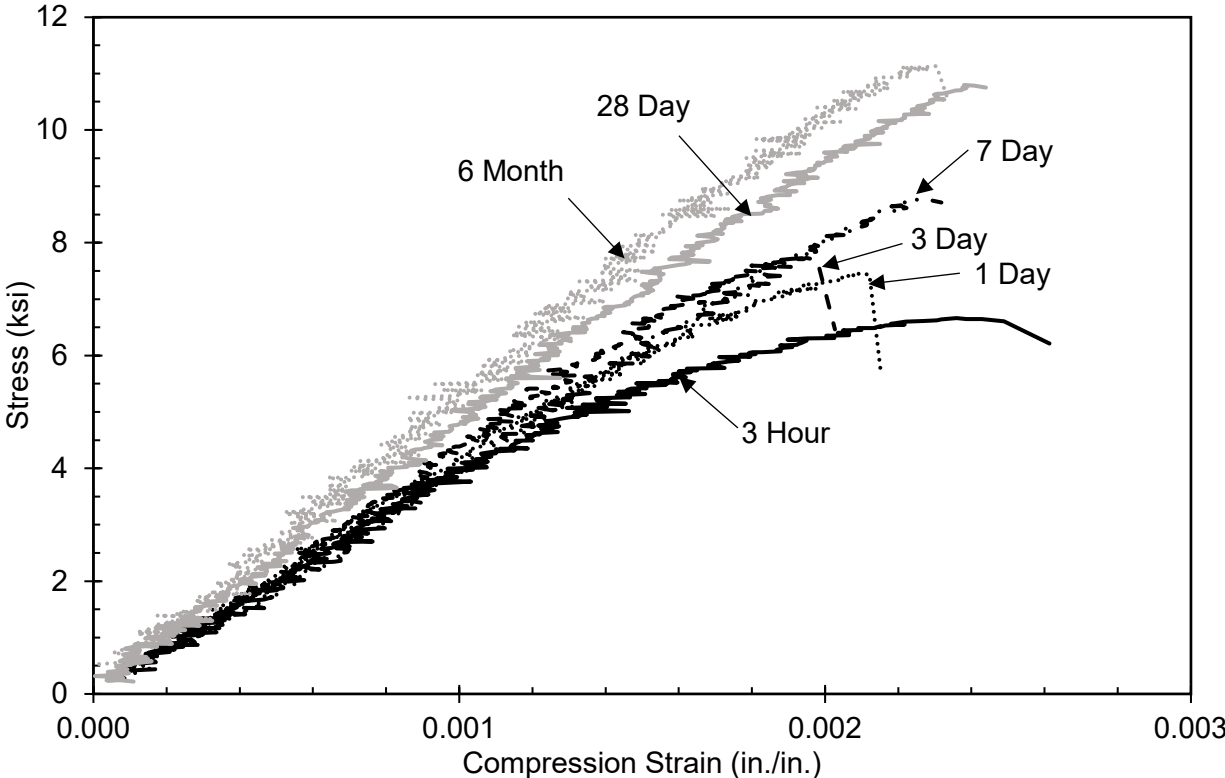


Figure 4.4 – Uniaxial compression strain 0.36 w/c BCSA cement concrete

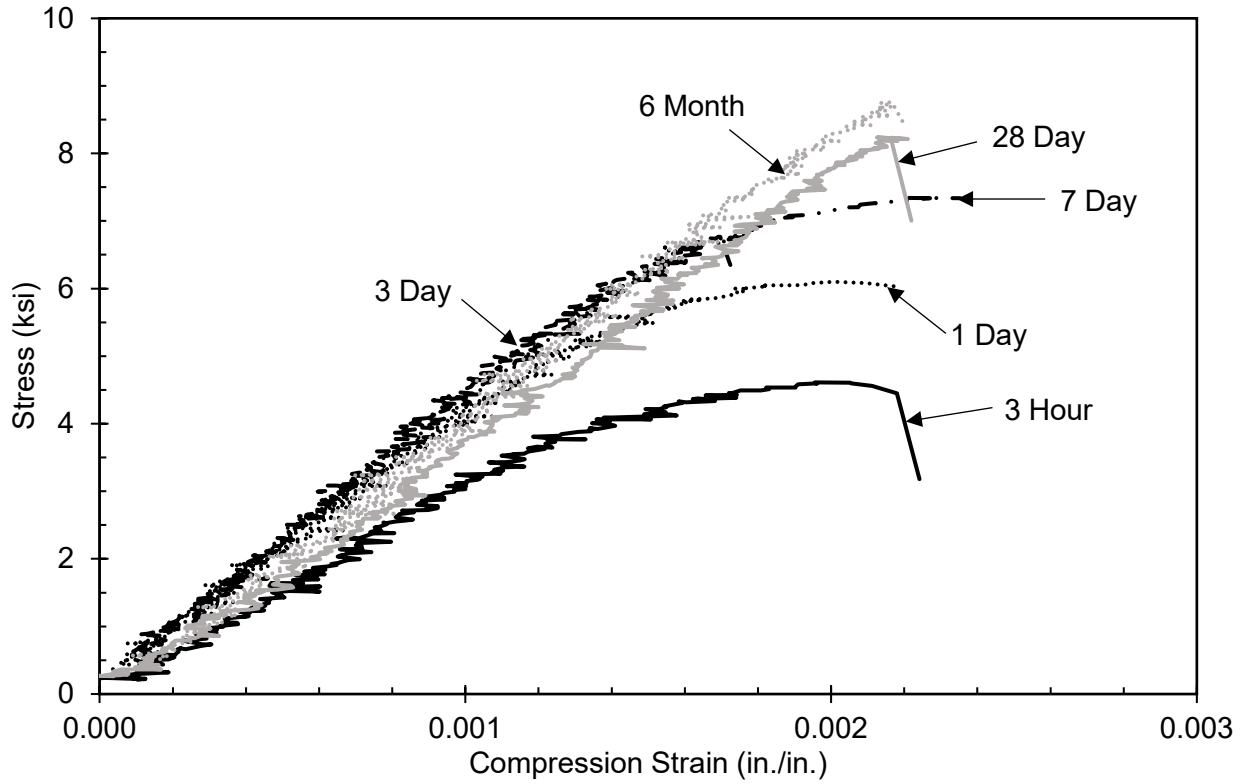


Figure 4.5 – Uniaxial compression strain 0.42 w/c BCSA cement concrete

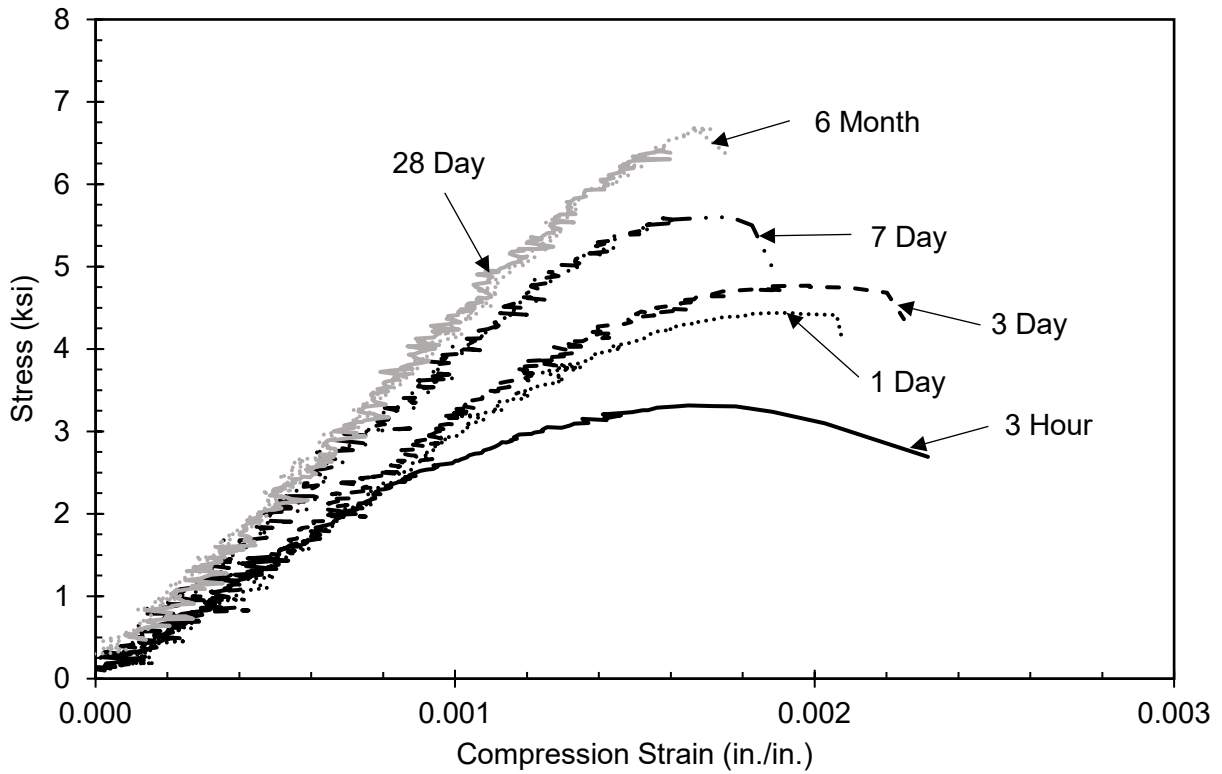


Figure 4.6 – Uniaxial compression strain 0.48 w/c BCSA cement concrete

Representative stress-strain graphs at 7 days for each w/c BCSA cement concrete specimens compared with 7 day PC specimens are shown in Figure 4.7. BCSA cement concrete strength increases with a decrease in w/c, linearity of the stress-strain graph is maintained closer to failure.

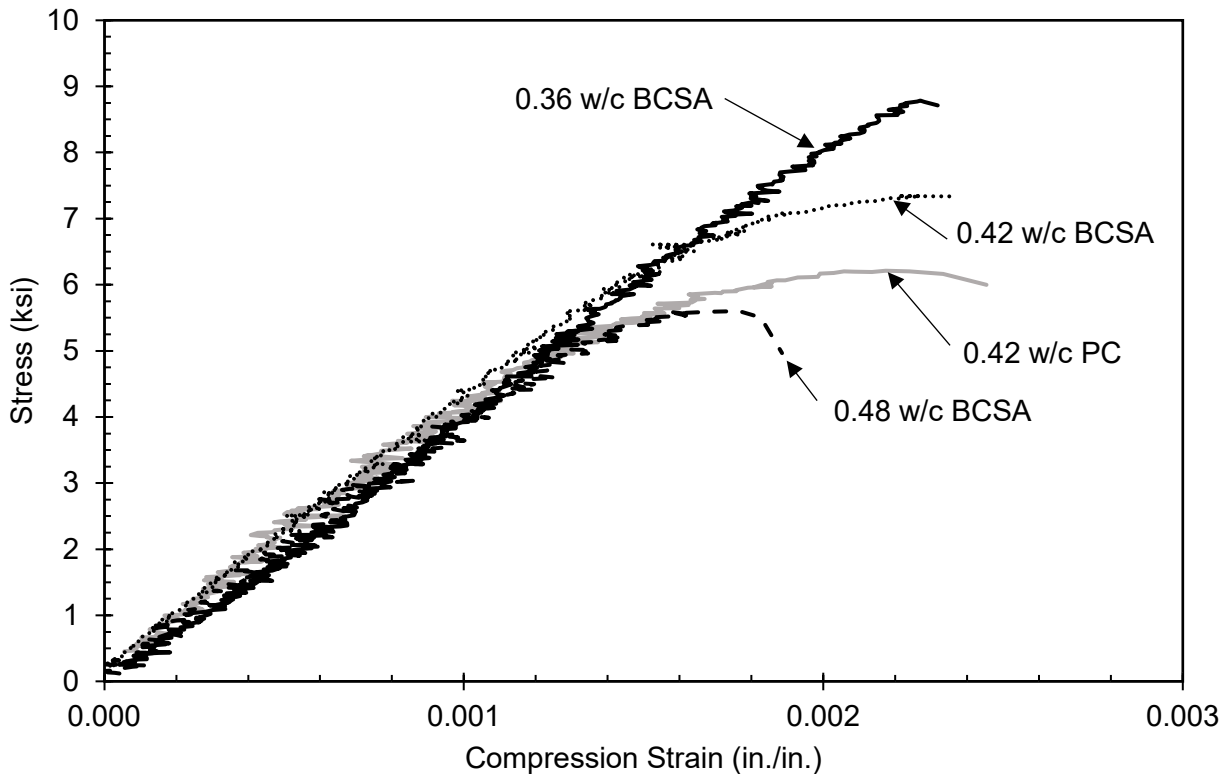


Figure 4.7 – 7 day uniaxial compression stress-strain relationship of various w/c

Stress-strain relationships of various w/c and cement types for 28 days are shown in Figure 4.8. 0.36 w/c BCSA cement concrete shows the most linear relationship between stress and strain with 0.42 PC showing the least amount of linearity. BCSA at both 7 and 28 days shows a linearity in the stress-strain relationship up to a higher percentage of max load when compared to PC. This could be caused by the different crystalline structures found within the cement matrix of BCSA allowing for microcracking to occur closer to ultimate failure.

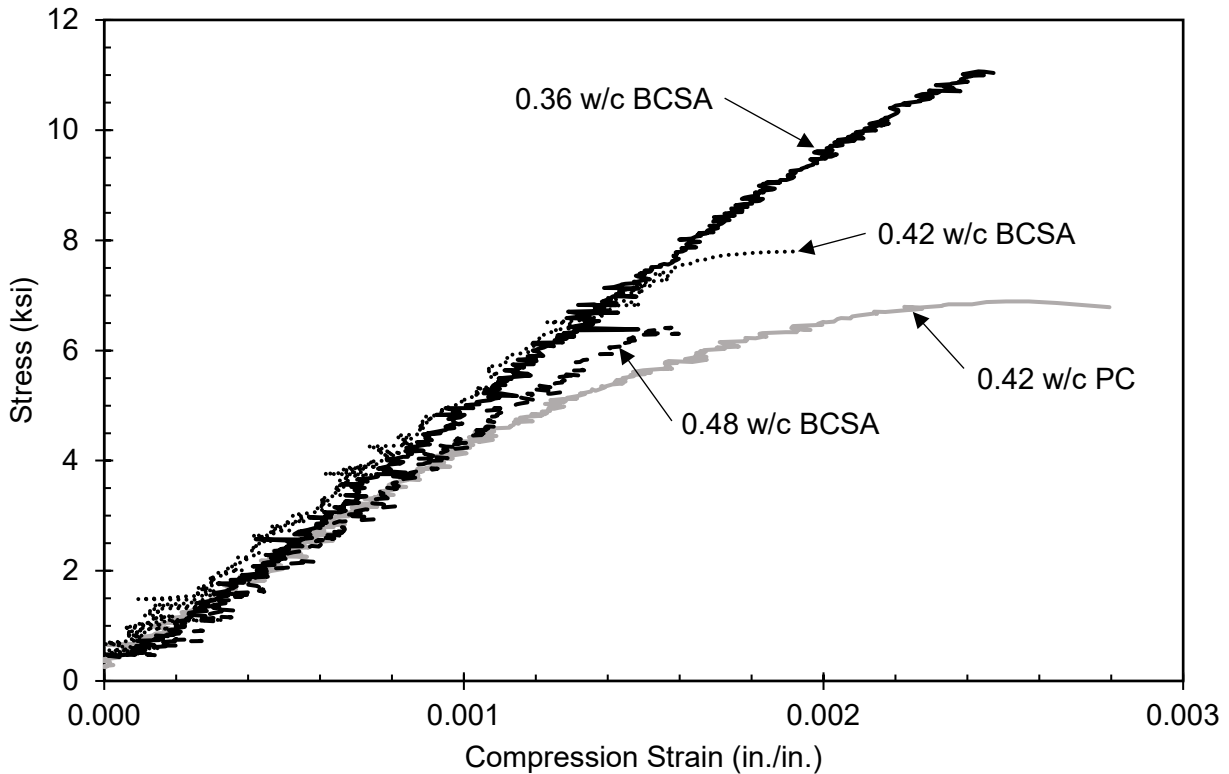


Figure 4.8 – 28 day uniaxial compression stress-strain relationship of various w/c

Some measured MOE results were slightly lower than the code equation estimates and comparable tests by Adnan et al. [45], although most of the data is inside the 20% bounds of the ACI 318 equation estimates for MOE. Coarse aggregate with a lower strength or lower MOE is shown to have a large effect on the MOE of concrete as previously described in section 2.3.1. Research by Adnan et al. used AASHTO M43 #67 crushed limestone coarse aggregate and this research used #57 crushed limestone. BCSA cement concrete cylinder results fall within the same range as PC cylinder results in this same research and they use the same w/c ratio and coarse aggregate and the same coarse aggregate. Results from both BCSA cement concrete, PC specimens and data from Adnan et al. can be seen in Figure 4.9.

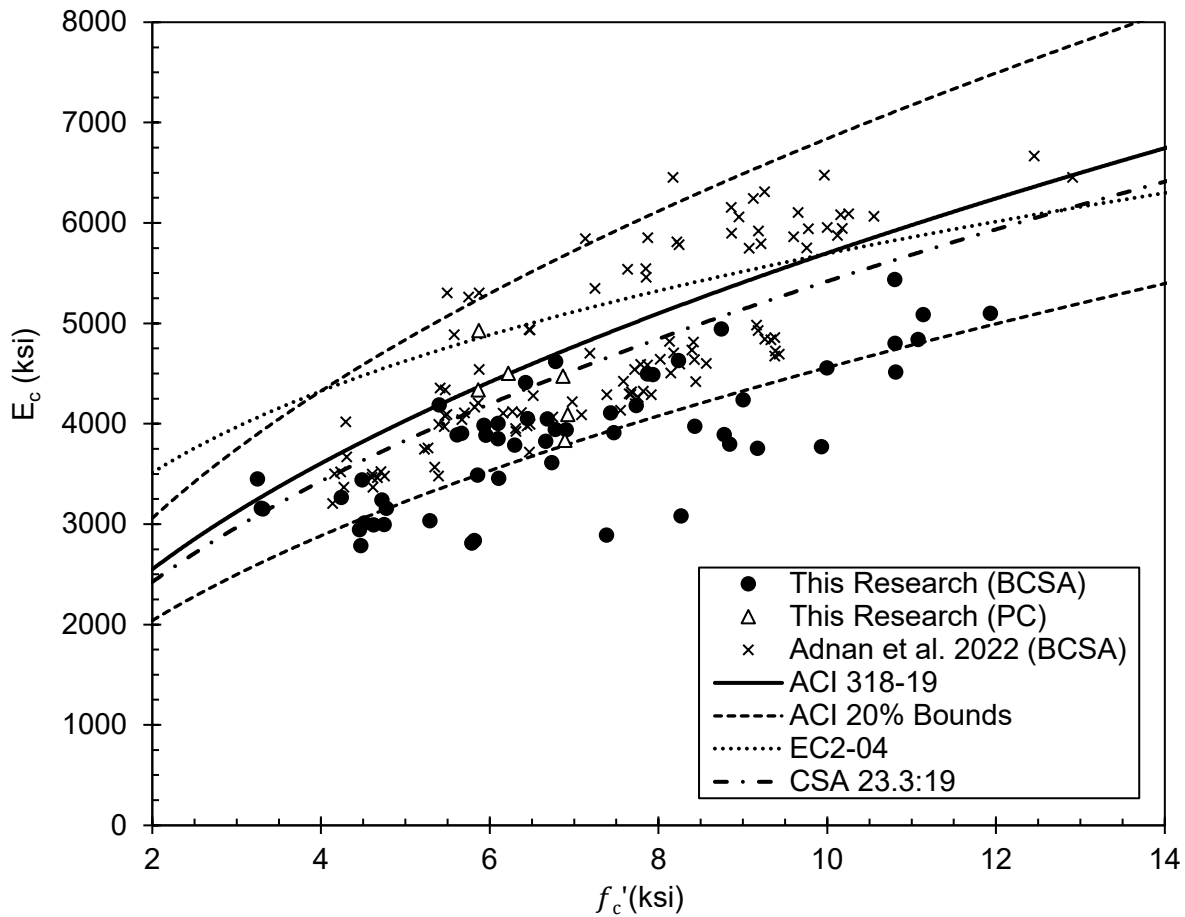


Figure 4.9 – All MOE results

Testing age seems to have little effect on the MOE of BCSA cement concrete as shown in Figure 4.10. This is contrary to the findings of Adnan et al. who stated that the code equations overestimated the MOE of BCSA cement concrete at early ages and underestimated the MOE at later ages (28 days and above). CSA 23.3:19 code equation seems to have a better fit to MOE of BCSA concrete because it estimates a slightly lower MOE than ACI 318-19 with EC2-04 being the worst fitting code equation of the three, overestimating the MOE for all BCSA cement concrete specimens.

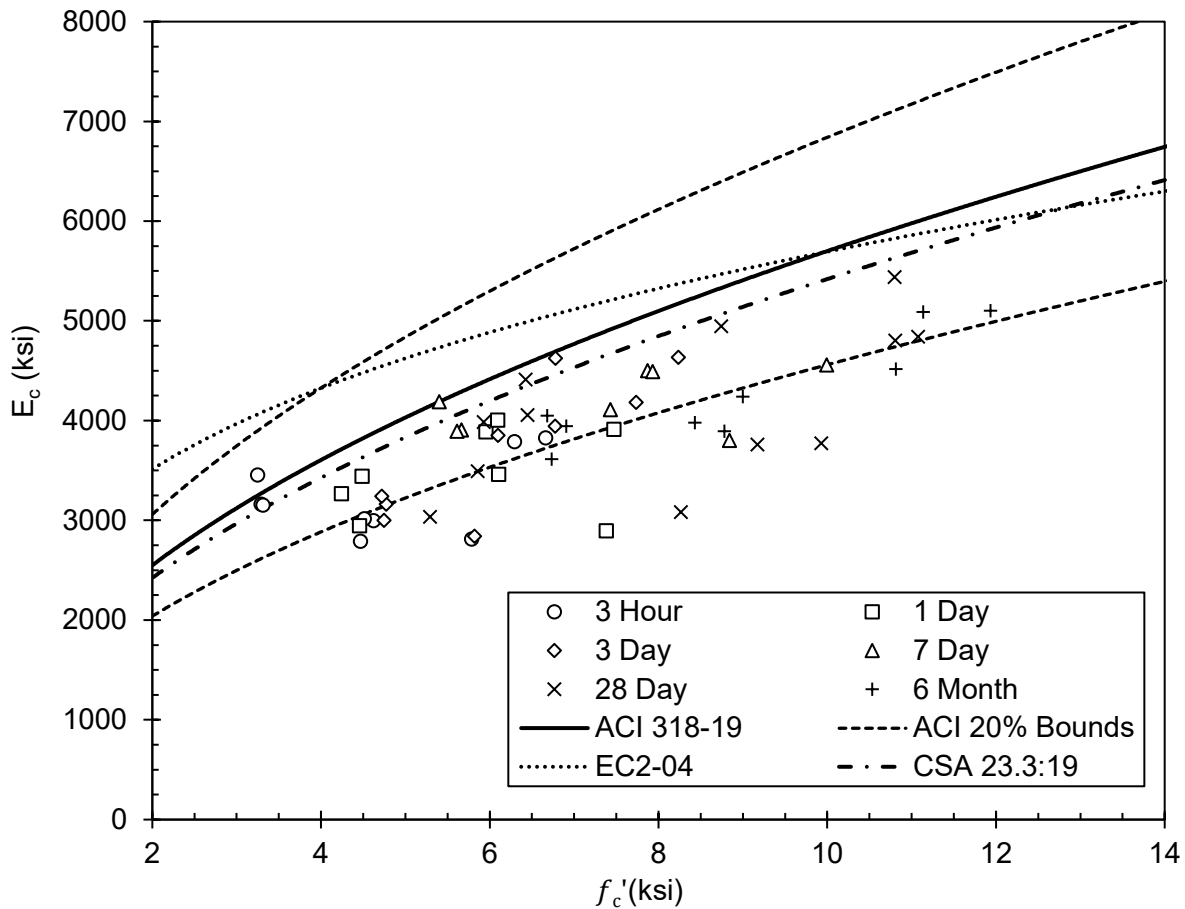


Figure 4.10 – MOE of BCSA cement concrete at various ages

The effect of w/c on MOE seems tied to compressive strength. Figure 4.11 shows 28 day and 6 month results of the three w/c tested. Each 0.06 increase in w/c corresponds with both a decrease in strength and MOE as would be expected with PC. From Figure 4.10, many later age, 0.48 w/c MOE data overlap with early age MOE data from 0.42 and 0.36 w/c cylinders of the same strength, indicating a better correlation between strength and MOE than w/c or age and MOE.

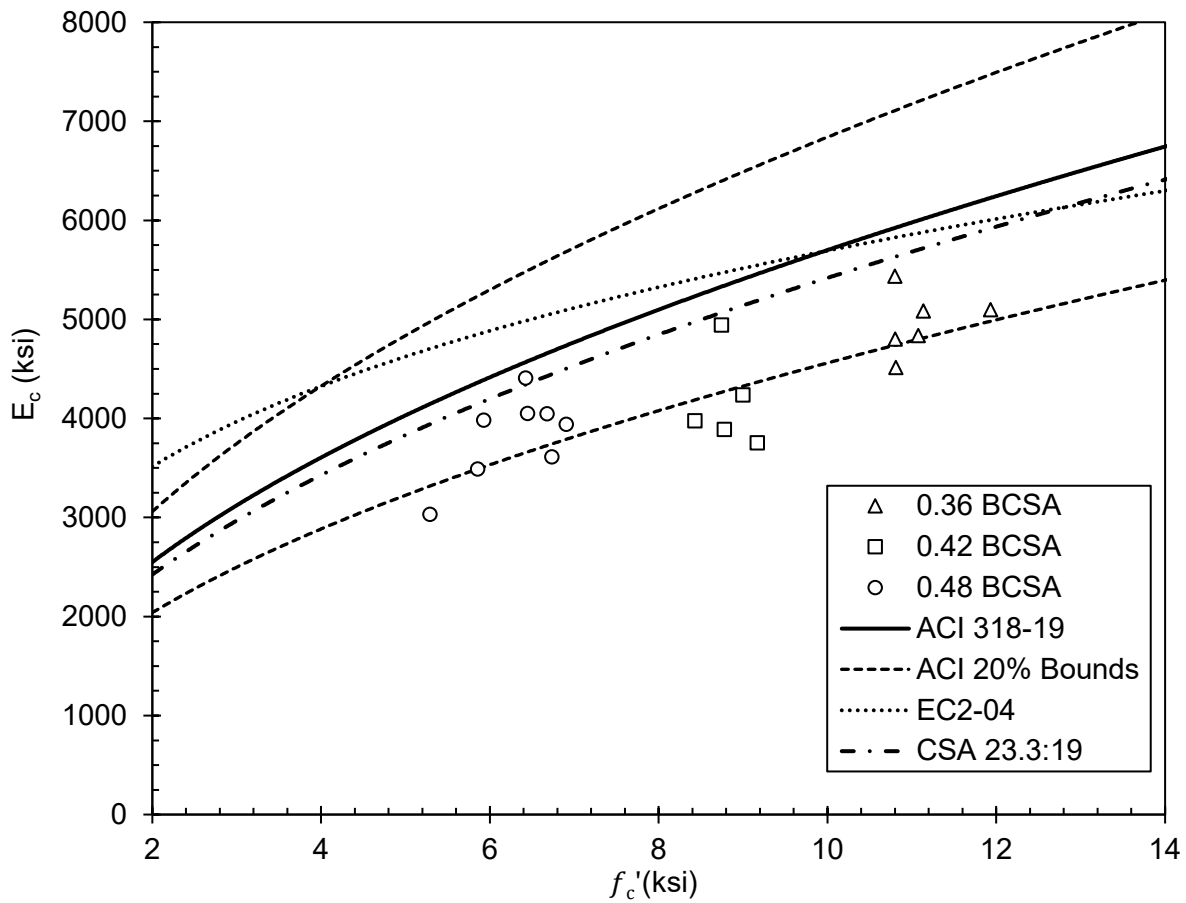


Figure 4.11 – MOE of BCSA cement concrete at 28 days or above

In Figure 4.12, uniaxial strain (ϵ'_c) values corresponding to maximum stress (f'_c) results for all ages of BCSA cement concrete of each w/c mixes and PC mixes are plotted alongside the same data as in Figure 2.3. Strain values ranged from 0.0014 to 0.0026 and stress values ranged from 3.1 to 11.9ksi. Uniaxial strain values for both BCSA cement concrete and PC mixes are comparable to historical values and are within the expected range as previously described in Section 2.3.2.

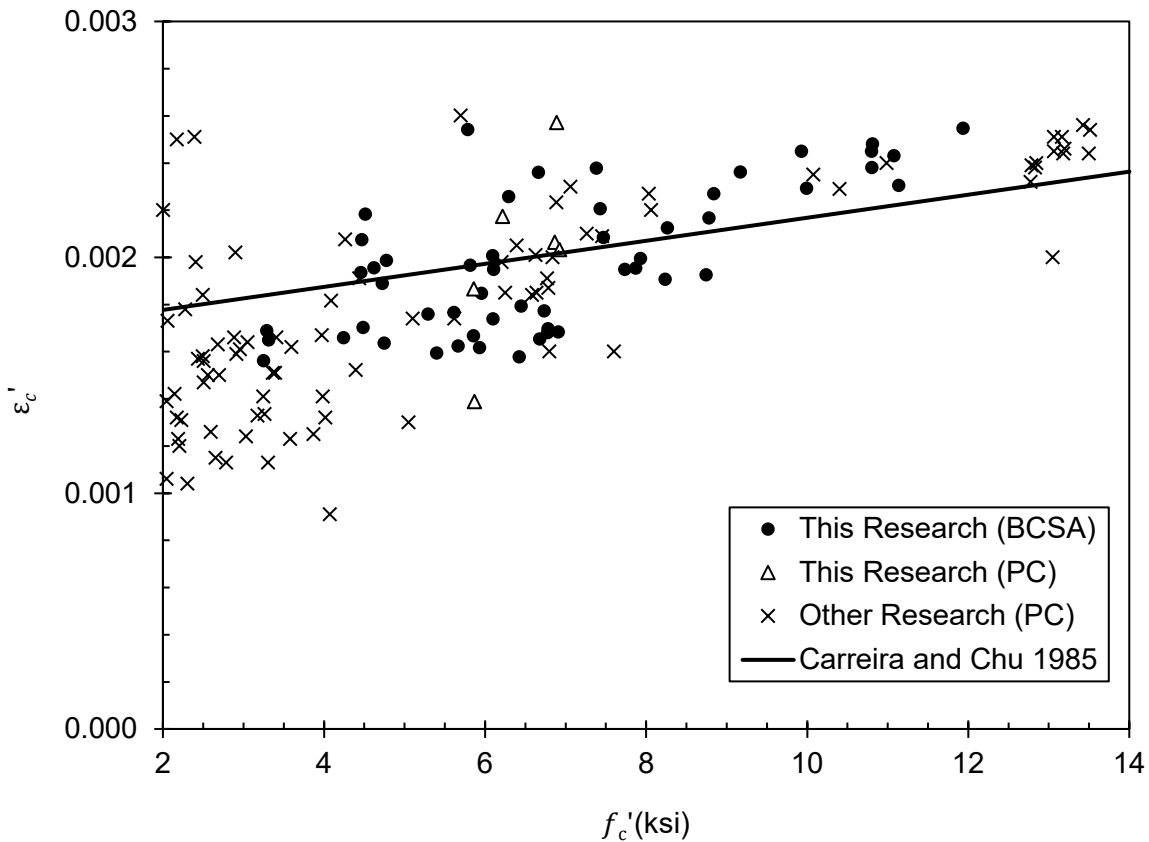


Figure 4.12 – Uniaxial compression strain results

4.2 Flexural Compression Specimens

A total of 26 flexural compressive specimens were made as described in Section 3.3.1. 14 of those specimens have results included here. Of the 12 specimens not included in the results, two specimens were left untested due to a section size that was too large (10 in. square and 7 in. square) to test with available testing equipment. Six specimens developed tension cracks prior to testing or completely broke and had to be discarded. This was due to improper removal of formwork or handling of specimens during demolding or test setup. Due to the specimens being unreinforced, it was found that extreme care had to be taken while demolding and sacrificial foamboard formwork was superior in preserving the integrity of specimens. The other four

specimens with results not included were tested using only Bridge Diagnostics strain gauges and results from the strain gauges were inconsistent or inconclusive. It was decided that all final specimen tests be performed with foil gauges attached in the manner described in Section 3.3.3 to ensure consistent and reliable results.

Table 4.4 – Flexural compressive specimen results

Specimen Name	w/c	Age (days)	f'_c (ksi)	P ₁ (kip)	P ₂ (kip)	ϵ_{cu} ($\mu\epsilon$)	Depth (in.)	Width (in.)
0.36 BCSA-1	0.36	7	11.3	204.5	6.3	3906	5.54	5.53
0.36 BCSA-2		7	11.5	270.1	10.6	3162	6.08	6.12
0.36 BCSA-3		28	12.4	220.1	5.5	4245	5.58	5.52
0.36 BCSA-4		28	12.1	289.8	7.0	3785	6.03	6.07
0.42 BCSA-5	0.42	7	10.7	267.2	11.8	3195	6.13	6.12
0.42 BCSA-6		9	10.7	274.3	9.0	2212	6.16	6.11
0.42 BCSA-7		28	11.4	270.3	8.0	3604	6.14	6.12
0.42 BCSA-8		31	11.4	288.6	10.4	2794	6.11	6.12
0.48 BCSA-9	0.48	7	7.8	221.2	7.3	3385	6.04	6.05
0.48 BCSA-10		7	7.8	230.4	8.0	3285	6.03	6.02
0.48 BCSA-11		28	9.5	224.8	7.7	2480	6.01	6.00
0.48 BCSA-12		28	9.5	238.9	7.7	2866	6.11	6.13
0.42 PC-1	0.42	28	8.9	242.4	5.0	2806	6.10	6.09
0.42 PC-2		29	8.9	236.1	7.7	3800	6.11	6.12

Virtual strain gauge extensometers were used to monitor the specimen during testing. An example of 3 in. virtual gauges and strain distribution across the variable strain surface of a flexural compressive specimen can be seen in Figure 4.13. The top edge of the specimen in Figure 4.13 is in compression while the bottom edge is close to zero strain.

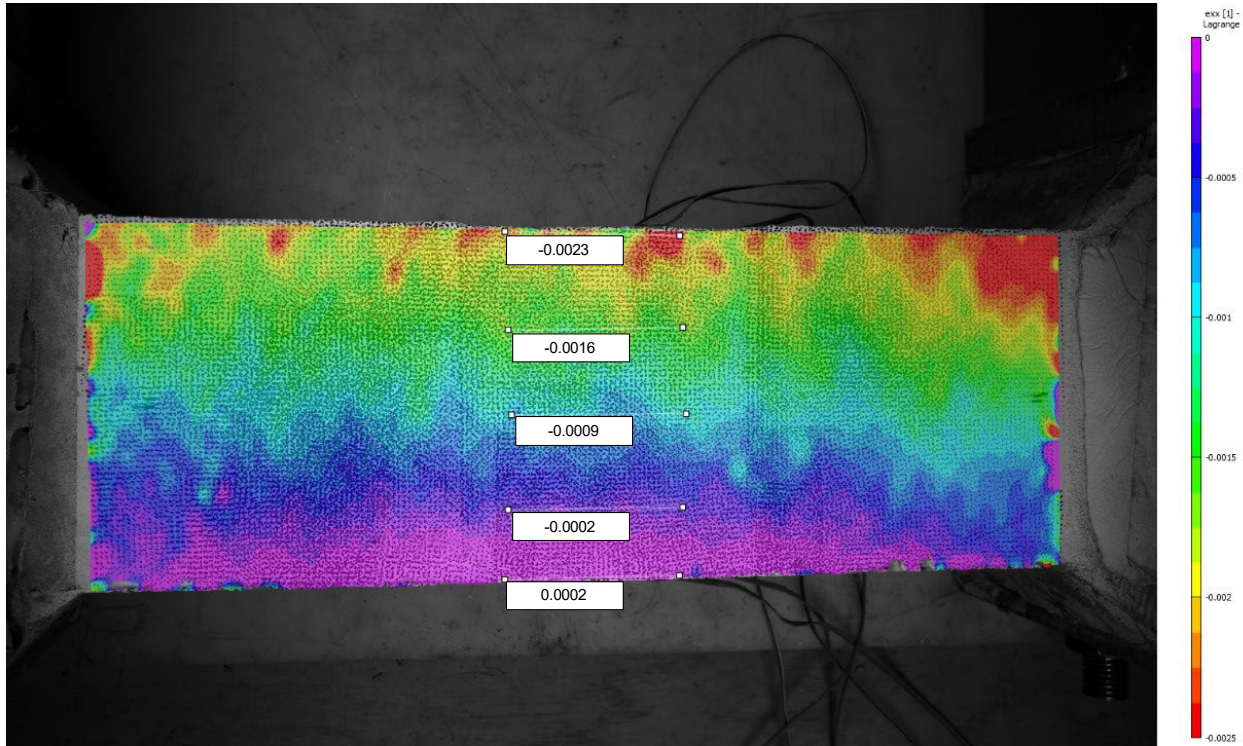


Figure 4.13 – Example of DIC strain gauge results prior to specimen failure

Some specimens experienced biaxial bending to varying degrees due to a lack of stiffness in the testing frame. During testing, increasing compression force P1 caused upward deflection of the spreader beams and slight rotation of the flanges which caused upward bending in the specimen. To account for this biaxial bending when calculating flexure design coefficients, the location and slope of the neutral axis of bending was calculated for each time iteration of testing. This was done by using interpolation between foil strain gauge measurement data to determine where on the specimen there is zero strain as shown in Figure 4.14. Strain values were calculated at each corner of the specimen before failure and are shown in Table 4.5.

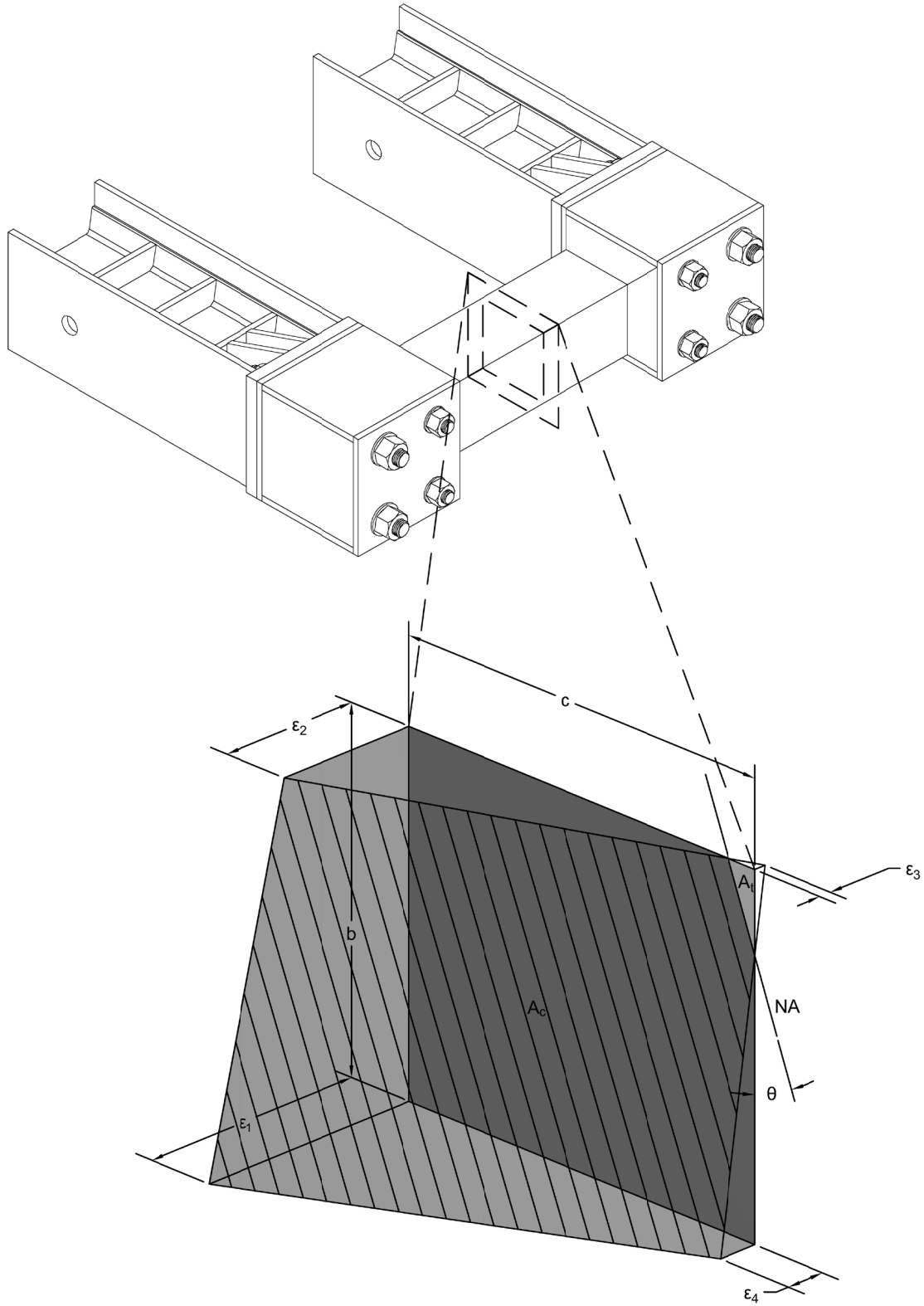


Figure 4.14 – Diagram of strain distribution in specimen before failure

Table 4.5 – Strains in each specimen before failure

Specimen Name	c (in.)	b (in.)	A _c (in. ²)	A _t (in. ²)	ε ₁ (με)*	ε ₂ (με)*	ε ₃ (με)*	ε ₄ (με)*	θ (degrees)
0.36 BCSA-1	5.54	5.53	29.13	1.51	-3906	-1268	765	-1643	44.7
0.36 BCSA-2	6.08	6.12	36.37	0.84	-3162	-1818	315	-748	27.2
0.36 BCSA-3	5.58	5.52	29.70	1.11	-4245	-1267	473	-1040	35.8
0.36 BCSA-4	6.03	6.07	36.02	0.60	-3785	-1930	334	-918	24.3
0.42 BCSA-5	6.13	6.12	37.18	0.38	-3195	-1997	167	-553	18.4
0.42 BCSA-6	6.16	6.11	37.46	0.18	-2212	-1678	145	-1054	31.1
0.42 BCSA-7	6.14	6.12	36.74	0.81	-3604	-1543	327	-963	34.5
0.42 BCSA-8	6.11	6.12	37.06	0.32	-2794	-1863	183	-748	24.5
0.48 BCSA-9	6.04	6.05	34.96	1.58	-3385	-1605	532	-996	35.6
0.48 BCSA-10	6.03	6.02	35.79	0.51	-3285	-2652	315	-878	21.9
0.48 BCSA-11	6.01	6.00	35.42	0.68	-2480	-1517	292	-1035	36.2
0.48 BCSA-12	6.11	6.13	37.17	0.24	-2866	-2161	171	-661	19.7
0.42 PC-1	6.10	6.09	35.87	1.28	-2806	-2086	612	-1139	29.5
0.42 PC-2	6.11	6.12	36.76	0.63	-3800	-1932	264	-768	22.5

* Negative microstrain represents compression strain

In Figure 4.14 and Table 4.5, c and b are non-deformed specimen dimensions. A_c and A_t represent the area of concrete in compression at failure and area of concrete in tension at failure, respectively. Strains values one through four correspond to linearly interpolated strain values at the corners of the specimen. And θ is the angle of the neutral axis with respect to the neutral strain specimen face in degrees.

Typical flexural compression specimen failure modes can be seen in Figure 4.15. The plan view (top) shows cracking throughout the section, with sliding plane cracks on the high compression side. Relatively unstressed concrete from the neutral axis face fractured in large pieces (middle). The result of biaxial bending can be seen as the specimen deflects upward but is greatly exaggerated by lens distortion of the camera (bottom).

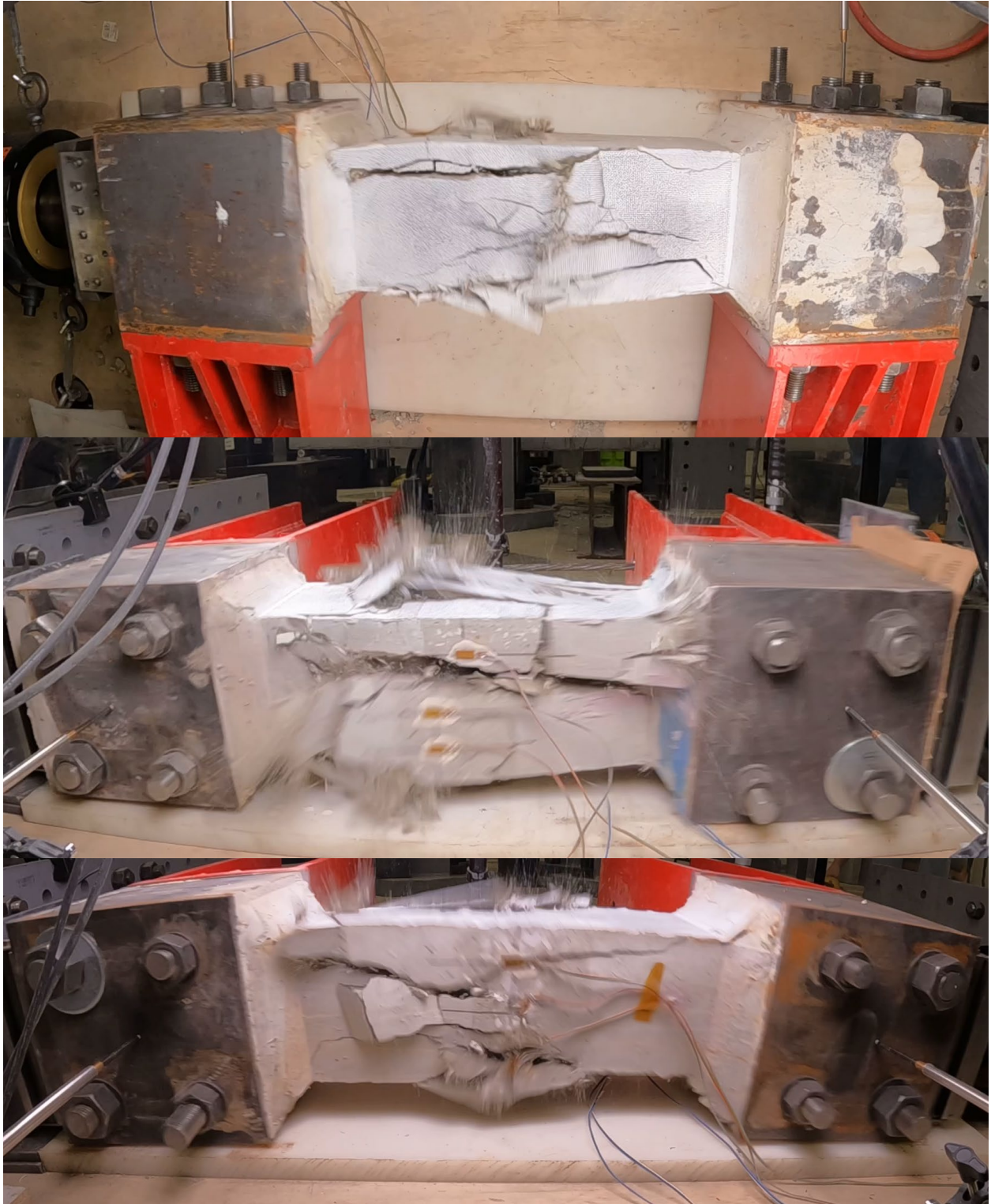


Figure 4.15 – Failure modes of flexural compressive specimens

Stress design parameters for each specimen were calculated as previously described in Section 3.3.5 and shown in Table 4.6. Due to a lack of adequate stiffness in the load frame and non-linear increase in strain, values of maximum stress, k_1 , and k_3 are directly affected by the results of the exponential smoothing techniques used to make the stress-strain relationship.

Table 4.6 – Flexural compressive specimen stress design parameter results

Specimen Name	f_c (ksi)	Max Stress (ksi)	ϵ_{cu} ($\mu\epsilon$)	k_1	k_2	k_3	k_1k_3	α_1	β_1
0.36 BCSA-1	11.32	9.93	3906	0.73	0.37	0.88	0.64	0.87	0.74
0.36 BCSA-2	11.54	11.11	3162	0.70	0.35	0.96	0.67	0.96	0.71
0.36 BCSA-3	12.36	11.88	4245	0.64	0.39	0.96	0.62	0.79	0.79
0.36 BCSA-4	12.09	11.94	3785	0.69	0.41	0.99	0.68	0.84	0.81
0.42 BCSA-5	10.68	12.54	3195	0.60	0.33	1.17	0.70	1.05	0.67
0.42 BCSA-6	10.68	12.60	2212	0.60	0.38	1.18	0.71	0.94	0.75
0.42 BCSA-7	11.37	11.00	3604	0.69	0.39	0.97	0.67	0.86	0.77
0.42 BCSA-8	11.37	12.41	2794	0.65	0.36	1.09	0.71	0.98	0.73
0.48 BCSA-9	7.80	9.04	3385	0.72	0.37	1.16	0.83	1.11	0.75
0.48 BCSA-10	7.84	9.72	3285	0.69	0.37	1.24	0.85	1.16	0.73
0.48 BCSA-11	9.53	10.10	2480	0.65	0.37	1.06	0.69	0.94	0.74
0.48 BCSA-12	9.48	10.42	2866	0.64	0.38	1.10	0.70	0.93	0.76
0.42 PC-1	8.93	8.83	2826	0.78	0.42	0.99	0.77	0.92	0.84
0.42 PC-2	8.93	8.52	3800	0.78	0.38	0.95	0.74	0.99	0.75

Ultimate strains were directly measured in the range of 0.0021 to 0.0035, however, these measured strains are not representative of the actual strains experienced in the extreme compression fiber of concrete. Linearly interpolated strain values from strain gauge measurements estimate ϵ_{cu} between 0.0022 and 0.0038. These strain values can be seen in Figure 4.16 as compared to historical data and code estimation equations as previously described in Section 2.4.3. Ultimate strain values fall mostly over the ACI estimate of 0.003 and all values for both BCSA cement concrete and PC specimens fall within the expected range when compared to historical data.

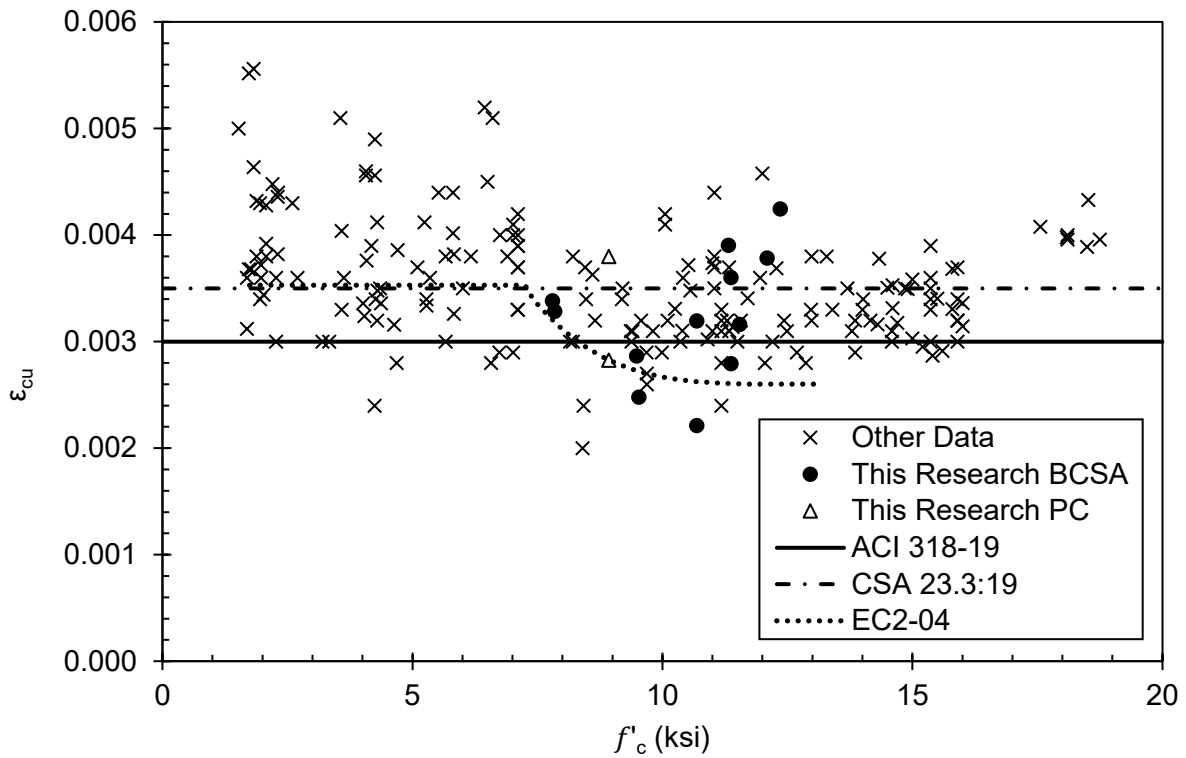


Figure 4.16 – Ultimate strain results ϵ_{cu}

Results of parameter k_1 or the ratio of average stress to maximum stress in the section is shown in Figure 4.17. These results ranged from 0.60 to 0.78 and are within the typical historical range of values presented in Figure 2.11. Because these results are within the typical historical range, this suggests that the general shape of compression stress distribution for BCSA cement concrete is similar to PC.

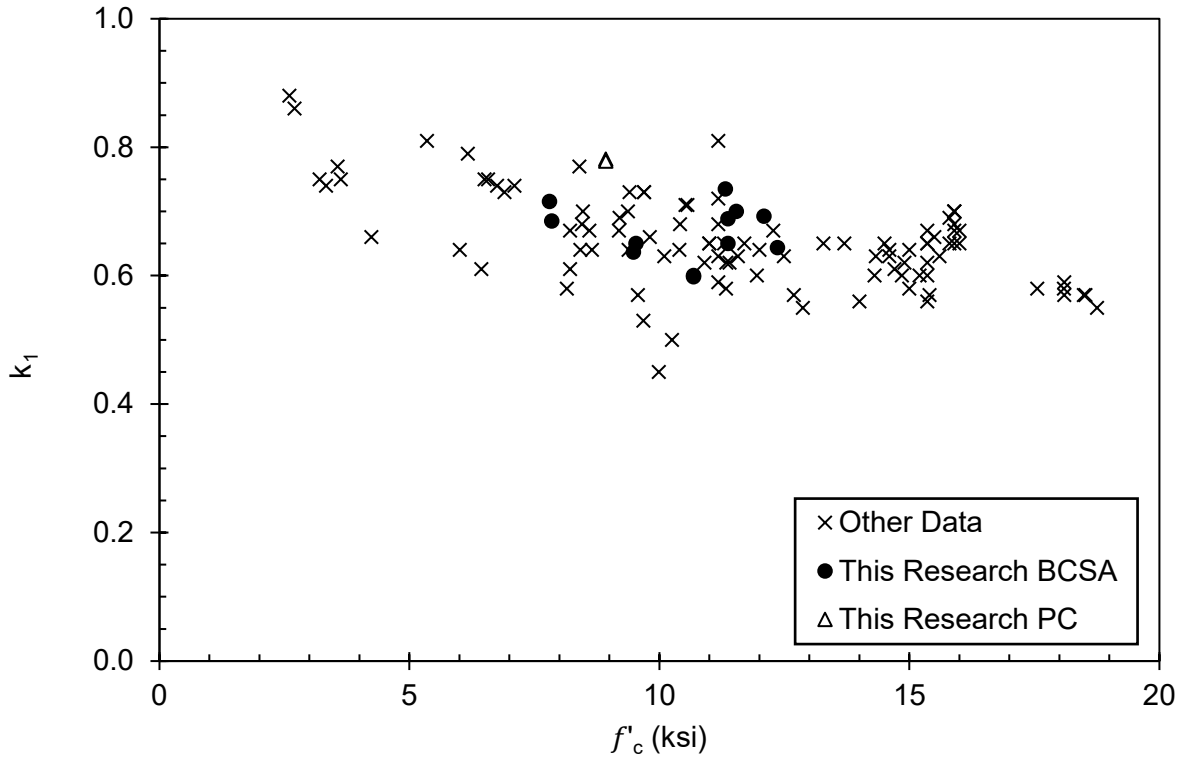


Figure 4.17 – Parameter k_1 results

Parameter k_2 results from flexural compression specimen data was calculated using Equation 3-2 and shown in Figure 4.18. Results ranged from 0.33 to 0.42 and was within the typical range of historical values previously established in Figure 2.12. Parameter k_2 is the ratio of depth of compression resultant force and depth of the neutral axis. It was observed for those concrete strengths (f'_c) between 7.8 and 12.4 ksi there is no significant increase or decrease in depth of resultant compression force. This is consistent with historical PC flexural compression specimens with a concrete strength greater than 7 ksi.

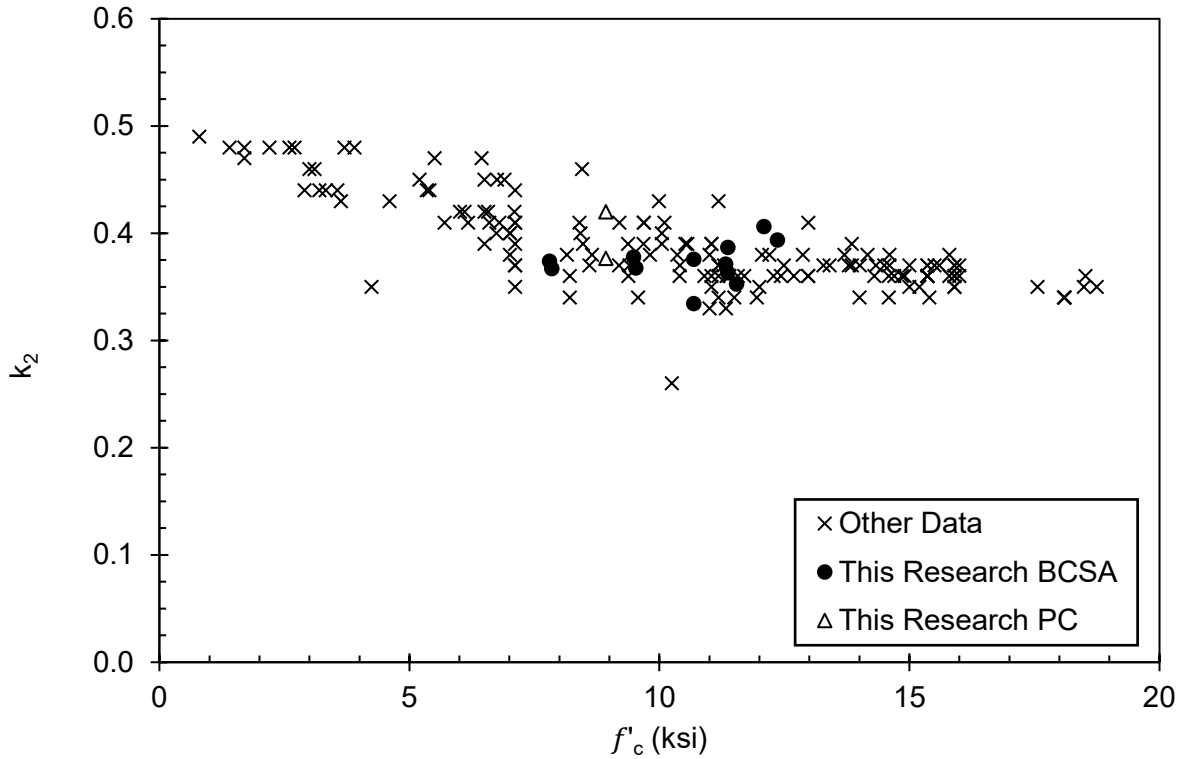


Figure 4.18 – Parameter k_2 results

Parameter k_3 results or the ratio between uniaxial concrete compressive strength (f'_c) and maximum compression stress in the flexural compression specimens is shown in Figure 4.19. These results were highly affected by data smoothing techniques used to produce the stress-strain relationships for each specimen as previously described in Section 3.3.5. However, results obtained for maximum stress ranged from 0.9 to 1.2 times f'_c and decreased with increasing f'_c . The values for BCSA cement concrete flexural compressive specimens are on the upper end of the range when compared with historical PC specimen results from Figure 2.13.

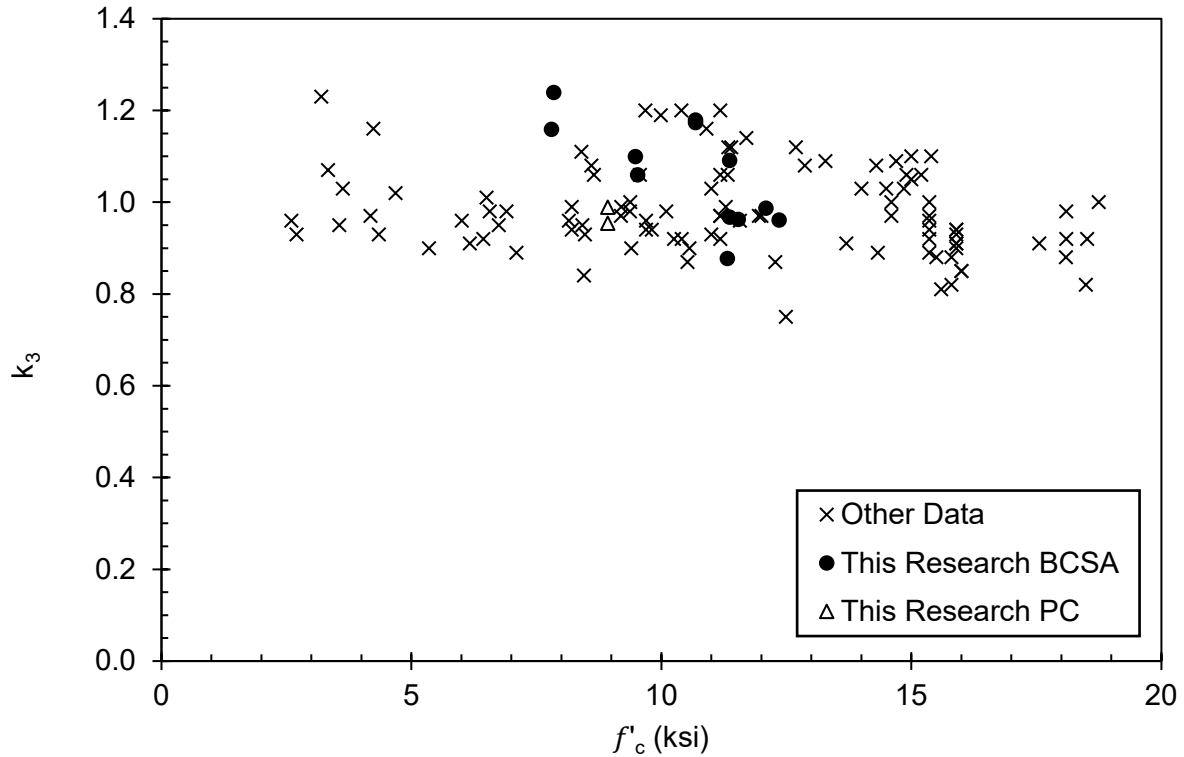


Figure 4.19 – Parameter k_3 results

The product of parameters k_1 and k_3 or α_1 and β_1 , modify the effect of f'_c on estimating the total compression force in flexural members. Results from both BCSA cement concrete and PC specimens can be seen in Figure 4.20 and are comparable to historically found values and concrete code estimations previously shown in Figure 2.14. All three code equations conservatively underestimate this value for BCSA, with EC2-04 [44] being the least conservative, closest estimate and ACI 318-19 [1] being the most conservative estimate.

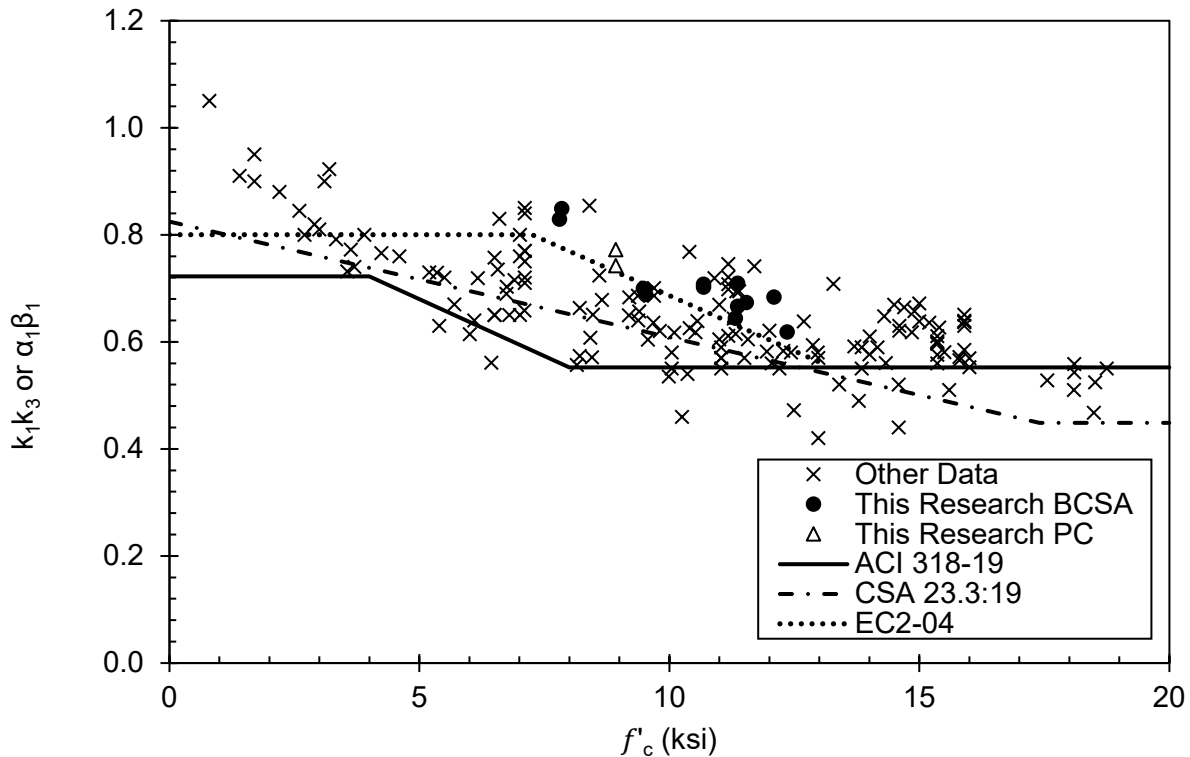


Figure 4.20 – Product of parameter k_1 and k_3 or α_1 and β_1 results

Design parameter α_1 results are shown in Figure 4.21 and are twice the value of parameter k_3 results. Parameter α_1 describes the magnitude of compression experienced by concrete in flexural compression members. Results for α_1 for BCSA cement concrete specimens fall within the upper range of historical PC values previously established in Figure 2.15. Results ranged from 1.16 to 0.84 for concrete strengths (f'_c) ranging from 7.8 to 12.4 ksi. Parameter α_1 results decrease as concrete strength increases. Code estimations of α_1 are conservative with EC2-04 [44] being the closest and least conservative, and CSA 23.3:19 [43] being the most conservative code estimate. Because the results of this parameter are in the upper range of values, this suggests that BCSA cement concrete flexural members could experience higher stress in compression concrete prior to failure, allowing for a smaller depth of compression overall, and higher strains in the tension steel which increases the ductility of flexural members.

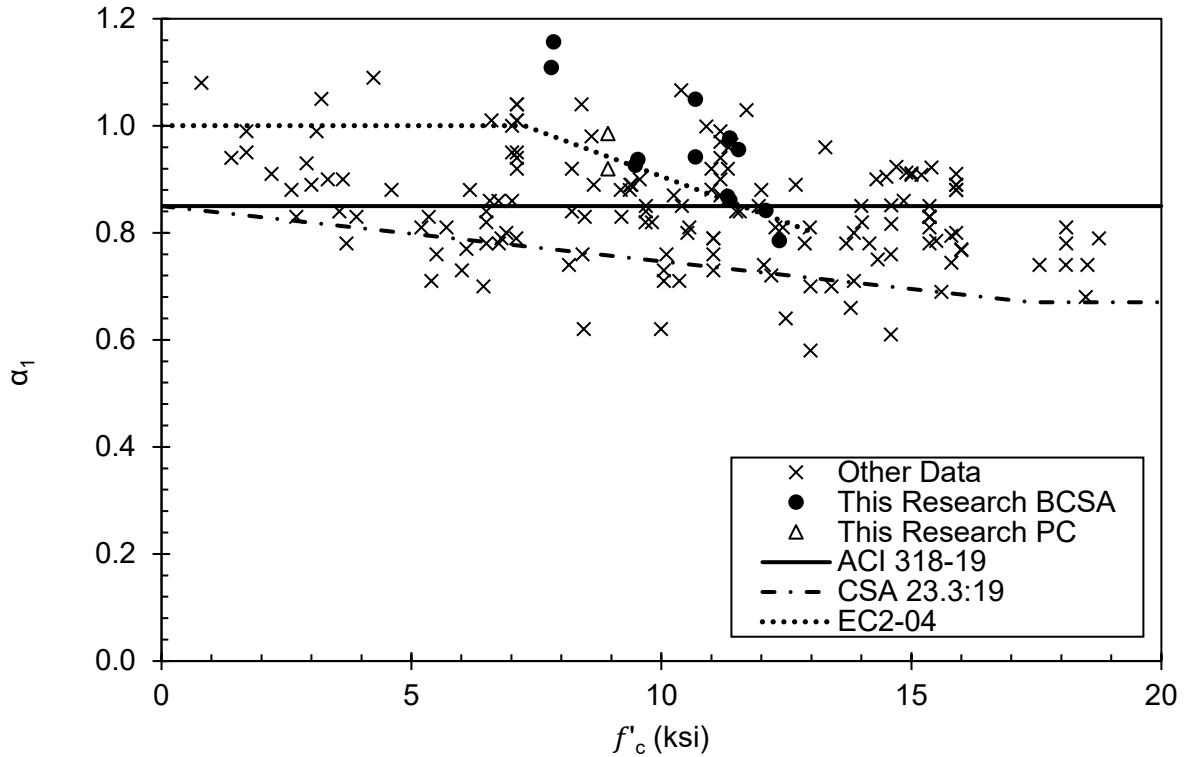


Figure 4.21 – Parameter α_1 results

Design parameter β_1 results are shown in Figure 4.22. β_1 is the ratio between the depth of compression and the depth of the neutral axis. Results for β_1 ranged from 0.67 to 0.84 and fell within the typical historical values for PC flexural compression specimen tests as previously shown in Figure 2.16. Values for β_1 did not significantly increase or decrease with increase in age or f'_c . For strengths ranging from 7.8 to 12.4 ksi, ACI 318-19 [1] is conservative in estimating β_1 . EC2-04 [44] estimates β_1 within the middle of found results and CSA 23.3:19 [43] slightly overestimates β_1 for BCSA cement concrete flexural compressive specimens. Results for β_1 suggest that the depth of compression in BCSA cement concrete relative to the neutral axis is similar to PC.

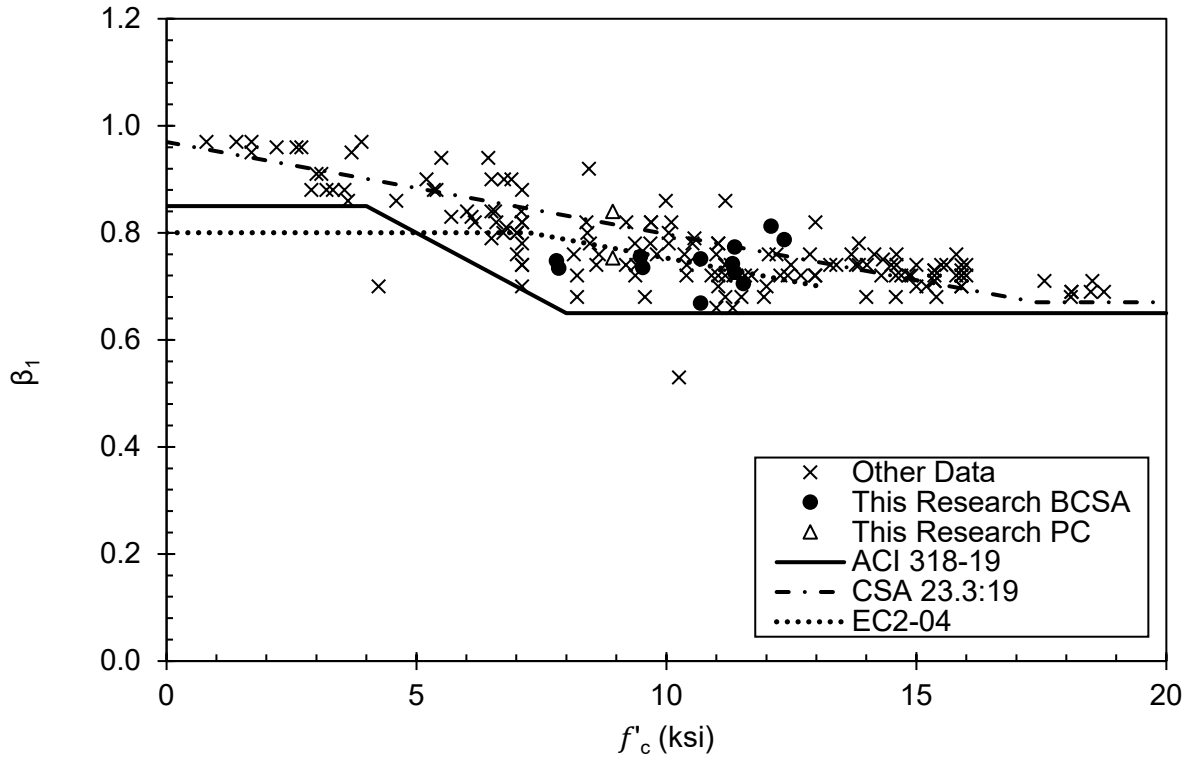


Figure 4.22 – Parameter β_1 results

Stress-strain relationships for flexural compression BCSA cement concrete members of various w/c are shown in Figure 4.23 through Figure 4.25. These stress-strain relationships were highly dependent on the rate of testing, discontinuity of testing, and stiffness of the load frame. Compounding noise resulting from using the sum of finite difference method and experimental sources of noise, required the use of exponential smoothing techniques as described in Section 3.3.5. The general shape of the stress-strain graph is represented, however, specific characteristics describing flexural compression stress-strain shape need further refinement through testing. Methods to produce smoother, more accurate stress-strain curves include using linearly increasing application of load P1, even application of load P2 which is directly tied to output strain values of the neutral strain face, adequately stiffened load frame, and using a load frame with unmoving, non-rotating platens.

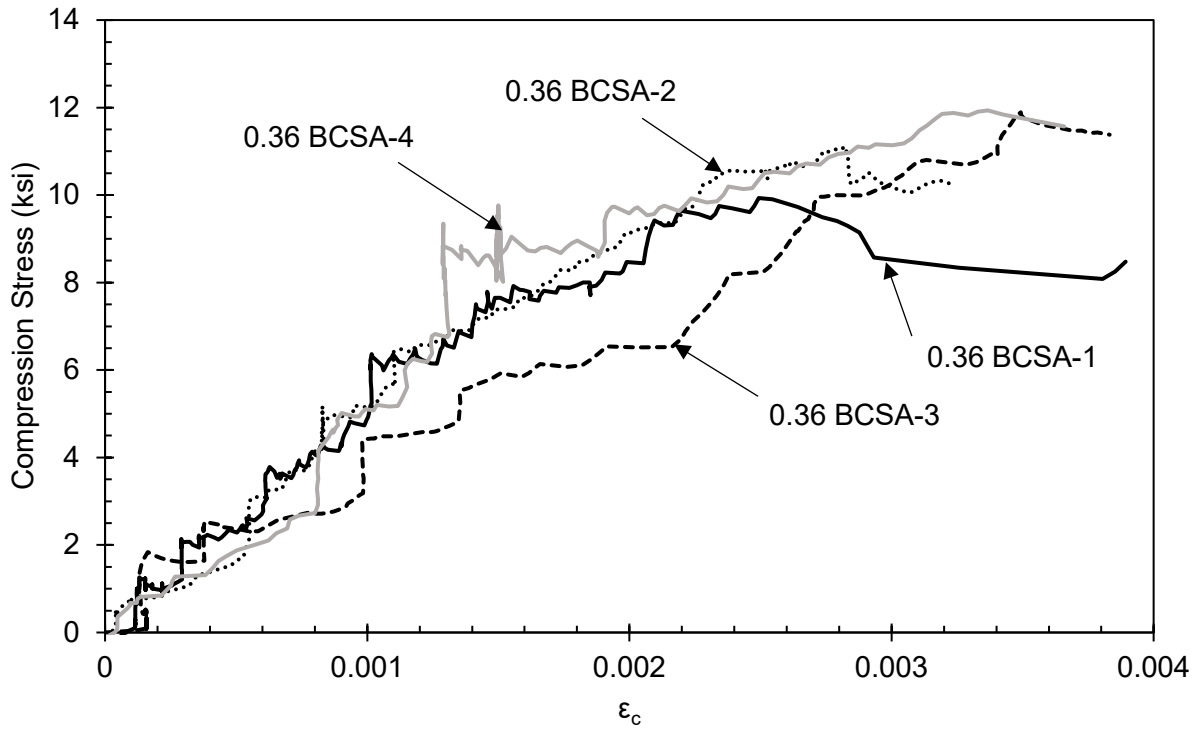


Figure 4.23 – Stress-strain relationship for 0.36 w/c BCSA flexural compressive specimens

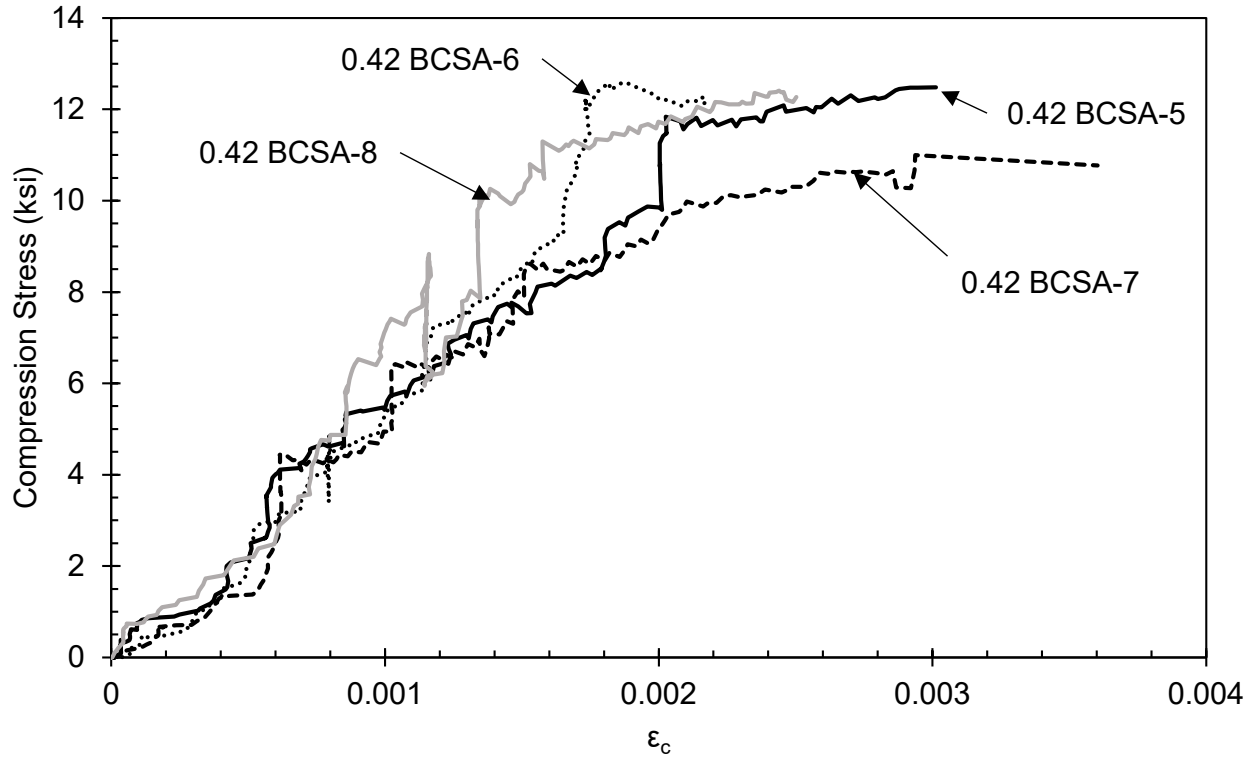


Figure 4.24 – Stress-strain relationship for 0.42 w/c BCSA flexural compressive specimens

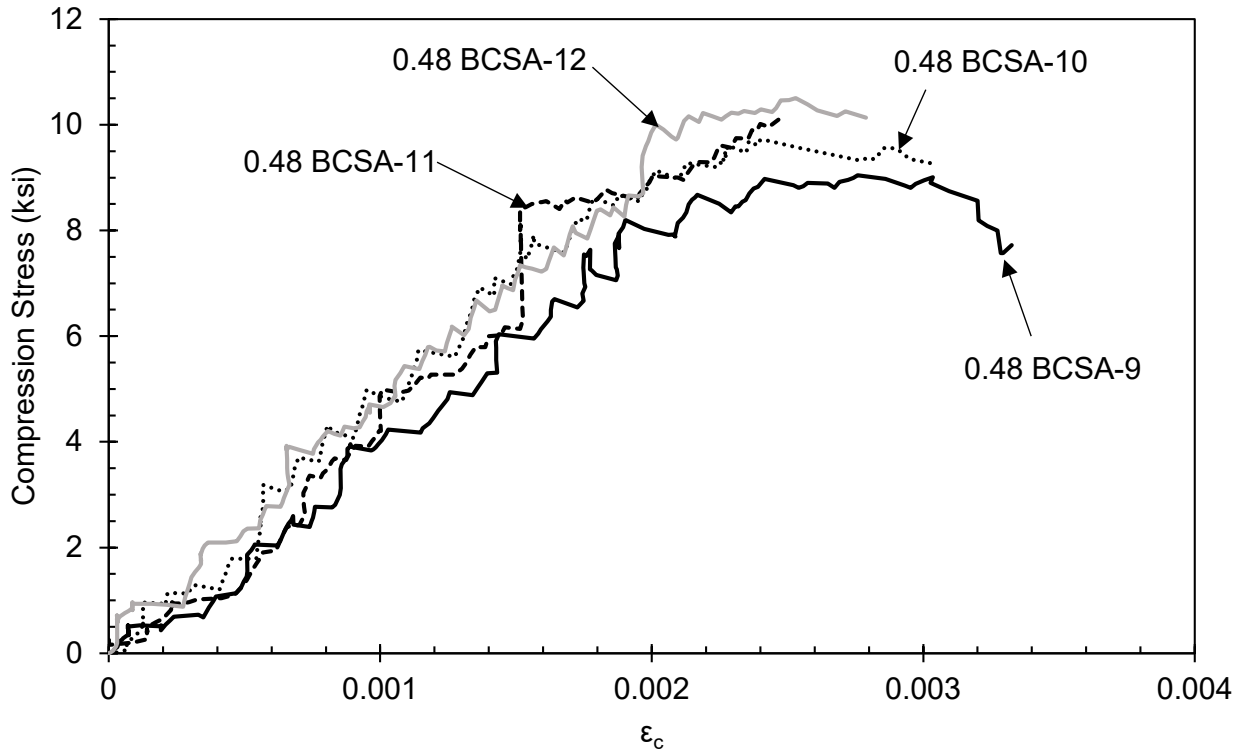


Figure 4.25 – Stress-strain relationship for 0.48 w/c BCSA flexural compressive specimens

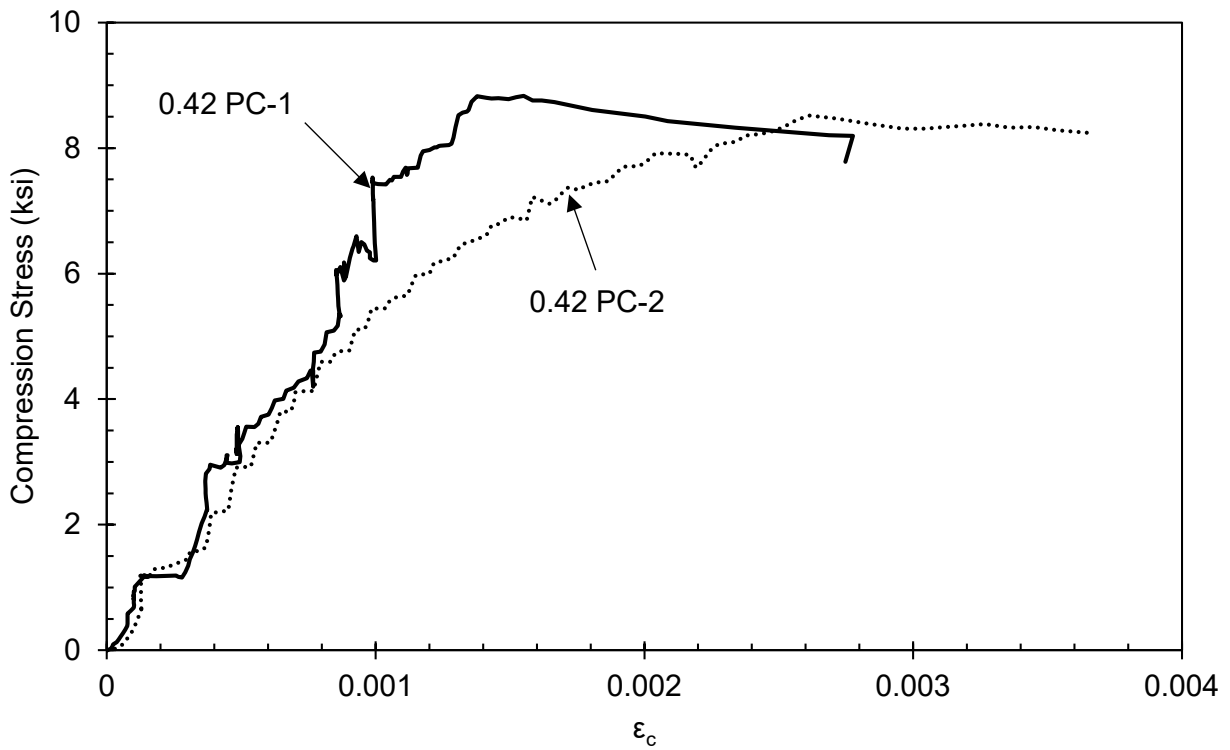


Figure 4.26 – Stress-strain relationship for 0.42 w/c PC flexural compressive specimens

5 Conclusions and Recommendations

This study evaluated both uniaxial compression and flexural compression performance of BCSA cement concrete for structural applications and design. Results from BCSA cement concrete specimens were compared with PC specimens, historical experimental results, and concrete design code estimations. 64 uniaxial compression tests were performed at various w/c (0.36, 0.42, and 0.48) and six different testing ages (3 hour, 1 day, 3 day, 7 day, 28 day, and 6 month). Results from uniaxial compression cylinders conclude:

- Static MOE of BCSA cement concrete cylinders was found to be slightly overestimated by ACI 318-19, EC2-04 and CSA 23.3:19 concrete design code equations for normal weight concrete. These results were also lower than one historical test presented using BCSA cement. The lower MOE results may be due to the type of coarse aggregate used in this study compared with other studies as the MOE of coarse aggregate has a substantial impact on the MOE of the concrete.
- Maximum uniaxial compression strain associated with maximum uniaxial compression stress (f'_c) in BCSA cement concrete cylinders was found to be comparable with historical values for PC cylinders with values ranging from 0.0014 to 0.0026. These results are also accurately represented by historical estimation and indicate that BCSA cement concrete can resist similar uniaxial strains when compared with PC.
- Uniaxial stress-strain results of BCSA cement concrete suggest that linearity of the stress-strain relationship is maintained for a larger portion of maximum stress than in PC. This is particularly evident in cylinders with a lower w/c. This may be caused by different crystalline structures in BCSA allowing for higher stresses before microcracking occurs.

14 Flexural compression specimen tests were performed with three different w/c (0.36, 0.42, 0.48) and two testing ages (7 days and 28 days) with f'_c strengths ranging from 7.8 to 12.4 ksi. Results from flexural compression specimens conclude:

- Ultimate concrete compressive strain (ϵ_{cu}) in BCSA cement concrete flexural members was found to fall within historical values for PC and code equations for estimating ϵ_{cu} . The ultimate strain value assumption of 0.003 proposed by ACI 318-19 [1] is adequate for estimating ϵ_{cu} in BCSA cement concrete specimens.
- All eccentric bracket specimens showed similar modes of failure with complete and rapid fracturing and crushing of the compression face. For specimens over roughly 7ksi cylinder strength (f'_c), fracturing planes through the coarse aggregate were observed which indicates that both the cement paste and the ITZ were stronger than the coarse aggregate.
- The assumption shape of stress distribution in the compression zone of flexural compression members is valid and applicable for BCSA cement concrete as indicated by the results from parameter k_1 .
- Depth of the compression block in BCSA cement concrete flexural members relative to the depth of the neutral axis is similar to PC flexural members indicated by results from parameter k_2 .
- Results from parameter k_3 suggest that compression concrete in BCSA cement concrete flexural members may experience higher maximum stress than PC flexural members of similar f'_c . This could be an explanation to higher ductility in BCSA flexural members as indicated by previous research [2], because the depth of compression can become smaller while the compression concrete has a higher capacity to resist crushing. However, these

results were highly dependent on data smoothing techniques to produce stress-strain relationships.

- All three concrete design code (ACI 318-19 [1], CSA 23.3:19 [43], and EC2-04 [44]) equations conservatively underestimate the product of parameters α_1 and β_1 for BCSA cement concrete flexural specimens. This implies nominal resultant compression force and moment capacity for flexural members calculated using these design codes will likely underestimate actual resultant compression force and moment capacity.
- The magnitude of BCSA cement concrete compression capacity in flexure specimens is within the upper range of historical data for flexure specimens as indicated by parameters k_3 and α_1 . All code equations (ACI 318-19 [1], CSA 23.3:19 [43], and EC2-04 [44]) conservatively underestimate design parameter α_1 with EC2-04 being the closest and least conservative estimate.
- Ratio between the depth of compression and the depth of the neutral axis (β_1) in BCSA cement concrete flexure members falls within historical values for PC. ACI 318-19 [1] conservatively estimates this design parameter while both CSA 23.3:19 [43] and EC2-04 [44] code estimates fall within the range of found results.
- Adequate testing frame stiffness, linearly increasing application of load, and accurate measurements of load and strain values are necessary to produce quality stress-strain relationships when using the sum of finite differences method for calculating concrete stresses based on measured strain.

It is recommended that results be replicated and verified using BCSA cement concrete flexural compressive members with strengths below 7 ksi and with testing ages prior to 7 days

and greater than 28 days. More complete results for a wider variety of strengths and ages of BCSA cement concrete in flexural compression is desired for validating adequacy of concrete design code equations. It is also recommended that flexural compression tests be performed using an adequately stiffened testing frame and a uniformly increasing loading scenario to produce more reliable stress-strain relationships for BCSA cement concrete in flexural compression.

6 References

- [1] ACI Committee 318, *Building Code Requirements for Structural Concrete and Commentary*. Farmington Hills, MI: American Concrete Institute, 2019.
- [2] G. W. Cook and C. D. Murray, “Behavior of Reinforced Concrete Made with Belitic Calcium Sulfoaluminate Cement at Early Ages,” *ACI Mater. J.*, vol. 117, no. 1, pp. 167–174, 2020.
- [3] H. Baji and H. R. Ronagh, “Reliability-Based Study on Ductility Measures of Reinforced Concrete Beams in ACI 318,” *ACI Struct. J.*, vol. 113, no. 2, pp. 373–382, 2016.
- [4] E. Hognestad, N. W. Hanson, and D. McHenry, “Concrete Stress Distribution in Ultimate Strength Design,” *ACI J. Proc.*, vol. 27, no. 4, pp. 455–479, 1955.
- [5] H. C. Mertol, S. Rizkalla, P. Zia, and A. Mirmiran, “Characteristics of Compressive Stress Distribution in High-Strength Concrete,” *ACI Struct. J.*, vol. 106, no. 4, pp. 626–633, 2008.
- [6] A. Klein, “Calcium aluminosulfate and expansive cement containing same,” *United States Pat. Off.*, vol. 58, no. 3, pp. 155–526, 1963.
- [7] B. OST, B. Schiefelbein, and J. M. Summerfield, “Very High Early Strength Cement,” 3860433, 1975.
- [8] M. B. Ali, R. Saidur, and M. S. Hossain, “A Review on Emission Analysis in Cement Industries,” *Renew. Sustain. Energy Rev.*, vol. 15, no. 5, pp. 2252–2261, 2011.
- [9] R. J. Thomas, A. D. Sorensen, I. Quezada, and M. Maguire, “Calcium Sulfoaluminate Cement,” *Concr. Int.*, vol. 40, no. 4, pp. 65–69, 2018.
- [10] T. Hanein, J. L. Galvez-Martos, and M. N. Bannerman, “Carbon footprint of calcium sulfoaluminate clinker production,” *J. Clean. Prod.*, vol. 172, no. November, pp. 2278–2287, 2018.
- [11] F. P. Glasser and L. Zhang, “High-performance cement matrices based on calcium sulfoaluminate-belite compositions,” *Cem. Concr. Res.*, vol. 31, no. 12, pp. 1881–1886, 2001.
- [12] E. Bescher, J. Stremfel, C. Ramseyer, and E. K. Rice, “The role of CSA in concrete sustainability,” *Twelfth International Conference on Recent Advances in Concrete Technology and Sustainability Issues*. pp. 612–632, 2012.
- [13] E. P. Bescher, J. Kim, K. Vallens, and C. Ramseyer, “Low Carbon Footprint Pavement: History of Use, Performance and New Opportunities for Belitic Calcium Sulfoaluminate,” in *13th International Symposium on Concrete Roads*, 2018, no. June, p. 15.
- [14] G. Jen, N. Stompinis, and R. Jones, “Chloride ingress in a belite-calcium sulfoaluminate

- cement matrix,” *Cem. Concr. Res.*, vol. 98, pp. 130–135, 2017.
- [15] H. Fujiwara, R. Tomita, T. Okamoto, A. Dozono, and A. Obatake, “Properties of High-Strength Porous Concrete,” Jun. 1998.
- [16] E. Bescher, E. K. Rice, C. Ramseyer, and S. Roswurm, “Sulfate Resistance of Calcium Sulphoaluminate Cement,” *J. Struct. Integr. Maint.*, vol. 1, no. 3, pp. 131–139, 2016.
- [17] R. J. Dillard, C. D. Murray, and R. A. Deschenes, “Belitic Calcium Sulfoaluminate Cement Subjected to Sulfate Attack and Sulfuric Acid,” *Constr. Build. Mater.*, vol. 343, no. January, pp. 1–10, 2022.
- [18] J. Péra and J. Ambroise, “New applications of calcium sulfoaluminate cement,” *Cem. Concr. Res.*, vol. 34, no. 4, pp. 671–676, 2004.
- [19] J. Han, D. Jia, and P. Yan, “Understanding the shrinkage compensating ability of type K expansive agent in concrete,” *Constr. Build. Mater.*, vol. 116, pp. 36–44, 2016.
- [20] N. Markosian, R. Tawadrous, M. Mastali, R. J. Thomas, and M. Maguire, “Performance Evaluation of a Prestressed Belitic Calcium Sulfoaluminate Cement (BCSA) Concrete Bridge Girder,” *Sustain.*, vol. 13, no. 14, 2021.
- [21] G. Ke and J. Zhang, “Effects of Retarding Admixture, Superplasticizer and Supplementary Cementitious Material on the Rheology and Mechanical Properties of High Strength Calcium Sulfoaluminate Cement Paste,” *J. Adv. Concr. Technol.*, vol. 18, no. 1, pp. 17–26, 2020.
- [22] J. Skocek, M. Zajac, F. Bullerjahn, and B. Haha, “Effect of retarders on the early performance of CSA-type cement,” *19. Int. Baustofftagung ibausil*, no. September, 2015.
- [23] I. Aguilar Rosero, “Effect of Citric Acid on Slump, Compressive Strength, and Setting Time of Belitic Calcium Sulfoaluminate Concrete,” University of Arkansas, 2020.
- [24] Y. Hu, W. Li, S. Ma, and X. Shen, “Influence of borax and citric acid on the hydration of calcium sulfoaluminate cement,” *Chem. Pap.*, vol. 71, no. 10, pp. 1909–1919, 2017.
- [25] L. E. Burris and K. E. Kurtis, “Influence of set retarding admixtures on calcium sulfoaluminate cement hydration and property development,” *Cem. Concr. Res.*, vol. 104, no. April 2017, pp. 105–113, 2018.
- [26] C. D. Murray, R. W. Floyd, and C. C. E. Ramseyer, “Using Belitic Calcium Sulfoaluminate Cement For Precast, Prestressed Concrete Beams,” *PCI J.*, vol. 64, no. 2, pp. 55–67, 2019.
- [27] N. A. Markosian, R. Thomas, M. Maguire, and A. Sorensen, “Calcium Sulfoaluminate Cement Concrete for Prestressed Bridge Girders: Prestressing Losses, Bond, and Strength Behavior,” Logan, Utah, 2019.

- [28] R. Maggenti, S. Gomez, and R. Luena, "Bridge Hinge Reconstruction," *Structure Magazine*, no. January, San Fransisco, pp. 30–32, Jan-2015.
- [29] T. M. Bowser, C. D. Murray, and R. W. Floyd, "Bond Behavior of 0.6 in. (15.2 mm) Prestressing Strand in Belitic Calcium Sulfoaluminate (BCSA) Cement Concrete," *ACI Struct. J.*, vol. 117, no. 1, pp. 43–52, 2020.
- [30] C. W. Chesnut and C. D. Murray, "Shear Capacity of Reinforced Concrete Made with Belitic Calcium Sulfoaluminate Cement," *ACI Struct. J.*, vol. 120, no. 1, pp. 177–186, 2023.
- [31] W. H. Peters and W. F. Ranson, "Digital Imaging Techniques In Experimental Stress Analysis," *Opt. Eng.*, vol. 21, no. 3, p. 213427, Jun. 1982.
- [32] B. Pan, "Digital Image Correlation for Surface Deformation Measurement: Historical Developments, Recent Advances and Future Goals," *Meas. Sci. Technol.*, vol. 29, no. 8, 2018.
- [33] M. A. Sutton and F. Hild, "Recent Advances and Perspectives in Digital Image Correlation," *Exp. Mech.*, vol. 55, no. 1, pp. 1–8, 2015.
- [34] T. M. Fayyad and J. M. Lees, "Application of Digital Image Correlation to Reinforced Concrete Fracture," *Procedia Mater. Sci.*, vol. 3, pp. 1585–1590, 2014.
- [35] S. Harenberg *et al.*, "Digital Image Correlation Strain Measurement of Ultra-High-Performance Concrete-Prisms Under Static and Cyclic Bending Tensile Stress," *Struct. Concr.*, vol. 20, pp. 1220–1230, 2019.
- [36] A. Ahmad and B. S. Firincioglu, "Utilizing DIC Technique for Visualizing the Failure Modes of Concrete Specimens," *Civ. Eng. Res. J.*, vol. 10, no. 2, pp. 28–34, 2020.
- [37] K. De Wilder, P. Lava, D. Debruyne, Y. Wang, G. De Roeck, and L. Vandewalle, "Experimental Investigation on the Shear Capacity of Prestressed Concrete Beams Using Digital Image Correlation," *Eng. Struct.*, vol. 82, pp. 82–92, 2015.
- [38] N. A. Hoult, W. Andy Take, C. Lee, and M. Dutton, "Experimental Accuracy of Two Dimensional Strain Measurements using Digital Image Correlation," *Eng. Struct.*, vol. 46, pp. 718–726, 2013.
- [39] ASTM C469/C469M, "Standard Test Method for Static Modulus of Elasticity and Poisson's Ratio of Concrete in Compression," *ASTM Stand. B.*, pp. 1–5, 2014.
- [40] S. Popovics, "A Review of Stress-Strain Relationships for Concrete," *J Amer Concr. Inst*, vol. 67, no. 3, pp. 243–248, 1970.
- [41] G. Giaccio, C. Rocco, D. Violini, J. Zappitelli, and R. Zerbino, "High-Strength Concretes Incorporating Different Coarse Aggregates," *ACI Mater. J.*, vol. 89, no. 3, pp. 242–246, 1992.

- [42] K. P. Mehta and P. J. M. Monteiro, *Concrete: Microstructure, Properties, and Materials*, 3rd ed. New York: McGraw-Hill Companies, 2006.
- [43] CSA Group, *CSA A23.3:19 Design of Concrete Structures*. Mississauga, Canada: Canadian Standards Association, 2019.
- [44] European Committee for Standardization, *Eurocode 2: Design of Concrete Structures*. Brussels: CEN, 2004.
- [45] T. A. H., A. Kienzle, and R. J. Thomas, “Engineering Properties and Setting Time of Belitic Calcium Sulfoaluminate (BCSA) Cement Concrete,” *Constr. Build. Mater.*, vol. 352, no. June, pp. 1–12, 2022.
- [46] M. R. A. van Vliet and J. G. M. van Mier, “Experimental Investigation of Concrete Fracture Under Uniaxial Compression,” *Mech. Cohesive-Frictional Mater.*, vol. 1, no. 1, pp. 115–127, 1996.
- [47] S. Kumar, T. Mukhopadhyay, S. A. Waseem, B. Singh, and M. A. Iqbal, “Effect of Platen Restraint on Stress–Strain Behavior of Concrete Under Uniaxial Compression: A Comparative Study,” *Strength Mater.*, vol. 48, no. 4, pp. 592–602, 2016.
- [48] M. Stredulova', D. Lisztwan, and J. Elias, “Friction Effects in Uniaxial Compression of Concrete Cylinders,” *Procedia Struct. Integr.*, vol. 42, pp. 1537–1544, 2022.
- [49] C. M. Sangha and R. K. Dhir, “Strength and Complete Stress-Strain Relationships for Concrete Tested in Uniaxial Compression Under Different Test Conditions,” *Mater. Struct. Constr.*, vol. 5, no. 30, pp. 361–370, 1972.
- [50] D. J. Carreira and Kuang-Han Chu, “Stress-Strain Relationship for Reinforced Concrete in Compression,” *ACI Struct. J.*, no. November-December, pp. 797–804, 1985.
- [51] S. G. M. and Y. L. E., “Ultimate Flexural Analysis Based on Stress-Strain Curves of Cylinders,” *ACI J. Proc.*, vol. 53, no. 12, 1956.
- [52] D. C. Jansen and S. P. Shah, “Effect of Length on Compressive Strain Softening of Concrete,” *J. Eng. Mech.*, vol. 123, no. 1, pp. 25–35, 1997.
- [53] P. Jiratprasot, “Mechanical Properties and Stress-Strain Behavior of High Performance Concrete under Uniaxial Compression,” New Jersey Institute of Technology, 2002.
- [54] K. Watanabe, J. Niwa, H. Yokota, and M. Iwanami, “Experimental Study on Stress-Strain Curve of Concrete Considering Localized Failure in Compression,” *J. Adv. Concr. Technol.*, vol. 2, no. 3, pp. 395–407, 2004.
- [55] S. Ahmad, K. Pilakoutas, Q. uz Z. Khan, and K. Neocleous, “Stress–Strain Model for Low-Strength Concrete in Uni-Axial Compression,” *Arab. J. Sci. Eng.*, vol. 40, no. 2, pp. 313–328, 2014.

- [56] ACI 318-14, *ACI 318-14 - Building Code Requirements for Structural Concrete*. 2014.
- [57] A. P. Fantilli, D. Ferretti, I. Iori, and P. Vallini, “Mechanical Model for Failure of Compressed Concrete in Reinforced Concrete Beams,” *J. Struct. Eng.*, vol. 128, no. 5, pp. 637–645, 2002.
- [58] H. C. Mertol, “Behavior of High-Strength Concrete Members Subjected to Combined Flexure and Axial Compression Loadings,” North Carolina State University, 2006.
- [59] J. K. Kim, S. T. Yi, and E. I. Yang, “Size Effect on Flexural Compressive Strength of Concrete Specimens,” *ACI Struct. J.*, vol. 97, no. 32, pp. 291–296, 2000.
- [60] Harrison F. Gonnerman, *Effect of Size and Shape of Test Specimen on Compressive Strength of Concrete*, vol. 1. Chicago, 1925.
- [61] J. K. Kim, S. T. Yi, and J. H. J. Kim, “Effect of Specimen Sizes on Flexural Compressive Strength of Concrete,” *ACI Struct. J.*, vol. 98, no. 40, pp. 416–424, 2001.
- [62] E. Hognestad, “A Study of Combined Bending and Axial Load in Reinforced Concrete Members,” *Univ. Illinois Bull.*, vol. 399, pp. 1–134, 1951.
- [63] C. S. Whitney, “Design of Reinforced Concrete Members Under Flexure or Combined Flexure and Direct Compression,” *Am. Concr. Inst.*, vol. 33, no. 3, pp. 483–498, 1937.
- [64] E. Hognestad, “Fundamental Concepts in Ultimate Load Design of Reinforced Concrete Members,” *ACI J. Proc.*, vol. 48, no. 6, pp. 809–830, 1952.
- [65] F. von Emperger, “Die Bulbeisendecke, System Pohlmann,” *Bet. und Eisen*, vol. 3, no. 3–4, pp. 159-163,234-235, 1904.
- [66] A. H. Mattock, L. B. Kriz, and E. Hognestad, “Rectangular Concrete Stress Distribution in Ultimate Strength Design,” *Am. Concr. Inst.*, vol. 57, no. 43, pp. 875–928, 1961.
- [67] M. Sargin, S. K. Ghosh, and V. K. Handa, “Effects of Lateral Reinforcement Upon the Strength and Deformation Properties of Concrete,” *Mag. Concr. Res.*, vol. 23, no. 75–76, pp. 99–110, 1971.
- [68] H. Nedderman, “Flexural Stress Distribution in Very-High Strength Concrete,” University of Texas at Arlington, 1973.
- [69] P. H. Kaar, N. W. Hanson, and H. T. Capell, “Stress-Strain Characteristics of High Strength Concrete,” in *Douglas McHenry International Symposium on Concrete and Concrete Structures*, 1978, vol. SP-55, pp. 161–185.
- [70] P. H. Kaar, A. E. Fiorato, J. E. Carpenter, and W. G. Corely, “Limiting Strains of Concrete Confined by Rectangular Hoops,” Skokie, IL, 1978.
- [71] S. E. Swartz, A. Nikaeen, N. Narayan Babu, H. D. Periyakaruppan, and T. M. E. Refai,

- “Structural Bending Properties of Higher Strength Concrete,” *High-Strength Concr.*, vol. 88, pp. 147–178, 1985.
- [72] J. A. Pastor, “High-Strength Concrete Beams,” Cornell University, 1986.
- [73] J. E. Schade, “Flexural Concrete Stress in High Strength Concrete Columns,” University of Calgary, 2008.
- [74] H. H. H. Ibrahim, “Flexural Behavior of High-Strength Concrete Columns,” University of Alberta, 1994.
- [75] T. H. Tan and N. B. Nguyen, “Flexural behavior of confined high-strength concrete columns,” *ACI Struct. J.*, vol. 102, no. 2, pp. 198–205, 2005.
- [76] H. H. H. Ibrahim and J. G. MacGregor, “Flexural behavior of laterally reinforced high-strength concrete sections,” *ACI Struct. J.*, vol. 93, no. 6, pp. 674–684, 1996.
- [77] ASTM C127, “Standard Test Method for Density, Relative Density (Specific Gravity), and Absorption of Coarse Aggregate,” *Annu. B. ASTM Stand.*, pp. 1–5, 2015.
- [78] ASTM C128, “Standard Test Method for Relative Density (Specific Gravity) and Absorption of Fine Aggregate,” *ASTM Int. West Conshohocken PA*, pp. 1–6, 2015.
- [79] ASTM C685/C685M, “Standard Specification for Concrete Made by Volumetric Batching and Continuous Mixing,” *Annu. B. ASTM Stand.*, pp. 1–9, 2017.
- [80] ASTM C143/C143M, “Standard Test Method for Slump of Hydraulic-Cement Concrete,” *Annu. B. ASTM Stand.*, pp. 1–4, 2020.
- [81] ASTM C1064/C1064M, “Standard Test Method for Temperature of Freshly Mixed Hydraulic-Cement Concrete,” *Annu. B. ASTM Stand.*, pp. 1–3, 2017.
- [82] ASTM C231/C231M, “Standard Test Method for Air Content of Freshly Mixed Concrete by the Pressure Method,” *Annu. B. ASTM Stand.*, pp. 1–10, 2022.
- [83] ASTM C192/C192M, “Standard Practice for Making and Curing Concrete Test Specimens in the Laboratory,” *Annu. B. ASTM Stand.*, pp. 1–8, 2019.
- [84] A. Klein and V. Bertero, “Effects of Curing Temperature and Creep Characteristics of Expansive Concretes.” University of California Berkley, Los Angeles, pp. 1008–1025, 1962.
- [85] L. E. Burris, P. Alapati, R. D. Moser, M. T. Ley, N. Berke, and K. E. Kurtis, “Alternative Cementitious Materials: Challenges and Opportunities,” *Am. Concr. Institute, ACI Spec. Publ.*, vol. 2015-Janua, no. SP 305, pp. 27.1-27.10, 2015.
- [86] ASTM C39/C39M, “Standard Test Method for Compressive Strength of Cylindrical Concrete Specimens,” *ASTM Stand. B.*, pp. 1–5, 2018.

- [87] M. A. Sutton, J.-J. Orteu, and H. W. Schreier, *Image Correlation for Shape, Motion and Deformation Measurements*. New York, NY, 2009.
- [88] I. Yoshitake, F. Rajabipour, Y. Mimura, and A. Scanlon, “A prediction method of Tensile young’s modulus of concrete at early age,” *Adv. Civ. Eng.*, no. January, 2012.

Appendix A: Historical Data Tables

Table A.1 – Historical MOE data for BCSA cement concrete

Adnan et al. 2022 (BCSA)						
w/c	3 Day		28 Day		> 253 Days	
	f'_c (ksi)	E_c (ksi)	f'_c (ksi)	E_c (ksi)	f'_c (ksi)	E_c (ksi)
0.5	4.75	3481	5.40	3996	6.47	4939
	4.71	3525	6.16	4105	6.48	4936
	4.67	3462	5.87	4208	5.50	5305
	4.61	3500	5.47	4338	5.58	4887
	4.60	3466	5.47	4080	7.25	5347
	4.27	3370	5.82	4168	5.75	5261
	4.29	4019	5.67	4044	7.85	5461
	4.62	3367	5.87	4540	5.88	5305
	4.31	3670	5.46	3973	7.87	5855
	4.16	3503	5.41	4358	7.63	5538
	4.23	3521	5.49	4095	7.13	5845
0.45	4.14	3207	5.70	4110	7.85	5547
	6.47	3719	8.18	4707	9.26	6312
	6.38	4113	7.68	4320	8.87	5900
	6.27	4122	7.92	4498	8.22	5813
	6.52	4281	7.72	4543	9.22	5795
	5.39	3479	8.13	4822	8.24	5783
	5.35	3567	8.43	4641	10.12	5878
	5.27	3760	8.57	4602	9.13	6246
	5.23	3747	8.15	4507	9.08	5750
	6.45	3979	7.92	4291	9.76	5751
	6.31	3925	7.87	4586	8.96	6060
0.4	6.48	3993	7.79	4592	9.60	5862
	6.31	3955	8.02	4643	9.65	6105
	7.19	4702	9.26	4844	9.78	5944
	6.75	4068	9.33	4837	10.16	6082
	7.09	4090	9.38	4860	10.55	6067
	6.98	4221	9.18	4928	9.97	6477
	7.65	4299	8.25	4595	10.00	5955
	7.82	4325	8.41	4814	10.18	5947
	7.39	4290	8.40	4735	8.17	6455
	7.55	4134	8.44	4420	9.19	5921
	7.59	4423	9.39	4727	10.25	6093
7.76	4266	9.43	4694	8.86	6156	
7.72	4200	9.38	4675	12.91	6455	
7.67	4293	9.16	4982	12.45	6668	

Table A.2 – Historical PC uniaxial cylinder stress-strain data

Source	f'_c (ksi)	ϵ'_c	Source	f'_c (ksi)	ϵ'_c	Source	f'_c (ksi)	ϵ'_c
Hognestad et al. (1955) [4]	1.55	0.0015	Watanabe et al. (2004) [54]	7.06	0.0023	Ahmad et al. (2014) [55]	3.97	0.0021
	2.90	0.0019		6.89	0.0022		4.02	0.0020
	5.05	0.0022		5.70	0.0026		4.07	0.0021
	6.80	0.0021		4.09	0.0018		3.99	0.0020
	7.60	0.0020		4.26	0.0021		1.75	0.0015
Smith and Young (1956) [51]	4.44	0.0020		4.39	0.0015		1.44	0.0013
	3.05	0.0020		3.18	0.0013		1.73	0.0016
	2.56	0.0017		3.26	0.0013		1.75	0.0016
	2.23	0.0017		0.80	0.0014		1.70	0.0016
Jansen and Shah (1997) [52]	6.21	0.0020		1.07	0.0010		1.57	0.0018
	8.06	0.0022	1.25	0.0013	1.78	0.0012		
	6.39	0.0021	1.51	0.0012	1.52	0.0011		
	8.03	0.0023	1.02	0.0012	1.75	0.0015		
	7.26	0.0021	0.91	0.0011	1.48	0.0014		
	6.63	0.0020	0.99	0.0014	1.57	0.0013		
	7.45	0.0021	0.90	0.0014	1.62	0.0015		
	6.25	0.0019	0.78	0.0013	2.51	0.0018		
	6.79	0.0019	0.94	0.0009	2.60	0.0019		
	6.77	0.0019	2.18	0.0013	2.91	0.0018		
	6.84	0.0020	2.00	0.0011	2.51	0.0020		
	6.64	0.0019	2.15	0.0012	2.49	0.0024		
	6.58	0.0018	2.31	0.0017	2.49	0.0025		
	13.18	0.0024	1.80	0.0015	3.58	0.0017		
	13.50	0.0024	2.20	0.0016	3.31	0.0016		
	12.83	0.0024	2.19	0.0012	3.39	0.0016		
	12.77	0.0023	1.93	0.0011	3.25	0.0018		
	13.51	0.0025	2.04	0.0016	3.87	0.0019		
	13.17	0.0025	1.97	0.0017	3.36	0.0016		
	13.06	0.0025	1.87	0.0017	1.74	0.0015		
	13.43	0.0026	1.68	0.0013	1.87	0.0013		
	12.79	0.0024	2.18	0.0009	2.28	0.0014		
	12.85	0.0024	2.04	0.0014	2.41	0.0020		
	13.20	0.0025	3.03	0.0017	1.96	0.0013		
	13.05	0.0020	2.89	0.0017	2.39	0.0016		
	13.06	0.0025	2.70	0.0016	2.06	0.0016		
Jiratatprasot (2002) [53]	5.10	0.0017	2.96	0.0019	2.68	0.0015		
	5.62	0.0017	2.65	0.0015	2.44	0.0014		
	10.08	0.0024	2.78	0.0014	1.94	0.0014		
	10.40	0.0023	3.60	0.0019				
	10.99	0.0024	3.41	0.0015				

Table A.3 – Historical PC flexural compression specimen data

Source	Specimen ID	f'_c	ϵ_{cu}	k_1	k_2	k_3	k_1k_3	α_1	β_1
Hognestad (1951) [62]	A1a*	5.28	0.0034						
	A1b*	5.66	0.0038						
	B1a*	4.25	0.0049						
	B1b*	4.07	0.0046						
	C1a*	2.27	0.0036						
	C1b*	2.02	0.0034						
	A2a*	5.28	0.0033						
	A2b*	5.83	0.0033						
	B2a*	4.25	0.0046						
	B2b*	4.07	0.0046						
	C2a*	2.27	0.0030						
	C2b*	1.97	0.0036						
	A3a*	5.66	0.0030						
	A3b *	5.83	0.0038						
	B3a*	4.63	0.0032						
	B3b*	4.29	0.0032						
	C3a*	1.88	0.0038						
	C3b *	1.69	0.0036						
	C4a*	1.69	0.0031						
	C4b*	1.73	0.0037						
	C5a*	2.31	0.0044						
	C5b*	1.77	0.0037						
	A7a*	5.24	0.0041						
	A7b*	5.81	0.0044						
	B7a*	4.08	0.0038						
	B7b*	4.04	0.0032						
	C7a*	1.97	0.0037						
	C7b*	1.52	0.0050						
	A8a*	5.52	0.0044						
	A8b*	5.81	0.0040						
	B8a*	4.70	0.0039						
	B8b*	4.26	0.0034						
	C8a*	1.82	0.0046						
	C8b*	1.82	0.0056						
B9b*	4.37	0.0034							
C9a*	1.88	0.0043							
C9b*	1.73	0.0055							
B12a*	4.30	0.0035							

Table A.3 – Historical PC flexural compression specimen data (cont.)

Source	Specimen ID	f'_c	ϵ_{cu}	k_1	k_2	k_3	k_1k_3	α_1	β_1
Hognestad (1951) [62]	BI2b*	4.01	0.0034						
	C12a*	2.30	0.0038						
	C12b*	2.20	0.0045						
	B13a*	3.58	0.0040						
	B13b*	4.29	0.0041						
	C13a*	2.30	0.0044						
	C13b*	2.07	0.0038						
	A14b*	5.10	0.0037						
	B14a*	3.58	0.0033						
	C14a*	1.95	0.0043						
	C14b*	2.07	0.0039						
	C15a*	1.95	0.0034						
	C15b*	2.07	0.0043						
Hognestad et al. (1955) [4]	1	0.80			0.49		1.05	1.08	0.97
	2	1.40			0.48		0.91	0.94	0.97
	3	1.70			0.48		0.95	0.99	0.97
	4	1.70			0.47		0.90	0.95	0.95
	5	2.20			0.48		0.88	0.91	0.96
	6	2.90			0.44		0.82	0.93	0.88
	7	3.00			0.46		0.81	0.89	0.91
	8	3.10			0.46		0.90	0.99	0.91
	9	3.70			0.48		0.74	0.78	0.95
	10	3.90			0.48		0.80	0.83	0.97
	11	4.60			0.43		0.76	0.88	0.86
	12	5.20			0.45		0.73	0.81	0.90
	13	5.40			0.44		0.63	0.71	0.88
	14	5.50			0.47		0.72	0.76	0.94
	15	5.70			0.41		0.67	0.81	0.83
	16	6.10			0.42		0.64	0.77	0.83
	17	6.50			0.39		0.65	0.82	0.79
	18	6.50			0.42		0.65	0.78	0.84
	19	6.80			0.41		0.65	0.79	0.81
Sargin et al. (1971) [67]	PE-1	4.35	0.0035			0.93			
	PE-2	4.68	0.0028			1.02			
	PE-3	4.18	0.0039			0.97			
Nedderman (1973) [68]	2	13.85	0.0032		0.37		0.59	0.80	0.74
	4	13.85	0.0029		0.39		0.55	0.71	0.78
	5	14.01	0.0034		0.37		0.61	0.82	0.74

Table A.3 – Historical PC flexural compression specimen data (cont.)

Source	Specimen ID	f'_c	ϵ_{cu}	k_1	k_2	k_3	k_1k_3	α_1	β_1
Nedderman (1973) [68]	6	14.16	0.0032		0.38		0.59	0.78	0.76
	7	11.50	0.0030		0.34		0.57	0.84	0.68
	9	12.97	0.0033		0.36		0.58	0.81	0.72
	10	12.43	0.0032		0.36		0.58	0.81	0.72
	11	12.05	0.0028		0.38		0.56	0.74	0.76
	12	12.20	0.0030		0.38		0.55	0.72	0.76
Kaar et al. (1978a) [69]	A6	6.50	0.0045	0.75	0.45	1.01	0.76	0.84	0.90
	A6P	6.90	0.0038	0.73	0.45	0.98	0.72	0.80	0.90
	A8	8.47	0.0034	0.70	0.39	0.93	0.65	0.83	0.78
	AI0	10.41	0.0036	0.68	0.37	0.92	0.63	0.85	0.74
	AI0P	9.38	0.0030	0.64	0.36	1.00	0.64	0.89	0.72
	A12	11.34	0.0031	0.62	0.36	1.12	0.69	0.96	0.72
	A14	14.00	0.0033	0.56	0.34	1.03	0.58	0.85	0.68
	A14P	13.28	0.0038	0.65	0.37	1.09	0.71	0.96	0.74
	D6	6.57	0.0028	0.75	0.42	0.98	0.74	0.86	0.84
	D6P	7.10	0.0033	0.74	0.42	0.89	0.66	0.79	0.84
	D8	8.42	0.0024	0.64	0.40	0.95	0.61	0.76	0.80
	D10	9.81	0.0031	0.66	0.38	0.94	0.62	0.82	0.76
	D10P	10.10	0.0032	0.63	0.41	0.98	0.62	0.76	0.82
	D12	11.18	0.0032	0.59	0.36	1.20	0.71	0.99	0.72
	D14	12.87	0.0028	0.55	0.38	1.08	0.59	0.78	0.76
	D14P	14.85	0.0035	0.60	0.36	1.03	0.62	0.86	0.72
	FI0	11.29	0.0032	0.65	0.37	0.99	0.64	0.86	0.74
	F12	12.69	0.0029	0.57	0.36	1.12	0.64	0.89	0.72
	F14	13.70	0.0035	0.65	0.38	0.91	0.59	0.78	0.76
	E4	4.24	0.0024	0.66	0.35	1.16	0.77	1.09	0.70
	E6	6.44	0.0052	0.61	0.47	0.92	0.56	0.70	0.94
	E8	8.21	0.0038	0.67	0.36	0.99	0.66	0.92	0.72
	E8P	8.45	0.0037	0.68	0.46	0.84	0.57	0.62	0.92
	E10	11.33	0.0037	0.58	0.33	1.06	0.61	0.92	0.66
	E12	12.49	0.0031	0.63	0.37	0.75	0.47	0.64	0.74
	E12P	11.95	0.0036	0.60	0.34	0.97	0.58	0.85	0.68
	C4	3.63	0.0036	0.75	0.43	1.03	0.77	0.90	0.86
	C4P	3.56	0.0051	0.77	0.44	0.95	0.73	0.84	0.88
	C6	6.01	0.0035	0.64	0.42	0.96	0.61	0.73	0.84
	C8	8.21	0.0030	0.61	0.34	0.94	0.57	0.84	0.68
C8P	8.15	0.0030	0.58	0.38	0.96	0.56	0.74	0.76	
C10	9.57	0.0032	0.57	0.34	1.06	0.60	0.90	0.68	

Table A.3 – Historical PC flexural compression specimen data (cont.)

Source	Specimen ID	f'_c	ε_{cu}	k_1	k_2	k_3	k_1k_3	α_1	β_1
Kaar et al. (1978a) [69]	C12	9.68	0.0029	0.53	0.39	1.20	0.64	0.82	0.78
	C12P	9.99	0.0029	0.45	0.43	1.19	0.54	0.62	0.86
Kaar et al. (1978b) [70]	12	3.33	0.0030	0.74	0.44	1.07	0.79	0.90	0.88
	20	3.20	0.0030	0.75	0.44	1.23	0.92	1.05	0.88
	17	6.75	0.0040	0.74	0.45	0.95	0.70	0.78	0.90
Swartz et al. (1985) [71]	1	8.40	0.0020	0.77	0.41	1.11	0.85	1.04	0.82
	2	9.40	0.0031	0.73	0.37	0.90	0.66	0.89	0.74
	3B	9.69	0.0027	0.73	0.41	0.96	0.70	0.85	0.82
	3C	9.69	0.0026	0.73	0.41	0.94	0.69	0.84	0.82
	4A	11.18	0.0033	0.81	0.43	0.92	0.75	0.87	0.86
	4B	11.18	0.0031	0.72	0.37	0.97	0.70	0.94	0.74
	4C	11.18	0.0028	0.68	0.37	1.06	0.72	0.97	0.74
Pastor (1986) [72]	SP-1	2.60	0.0043	0.88	0.48	0.96	0.84	0.88	0.96
	SP-2	2.70	0.0036	0.86	0.48	0.93	0.80	0.83	0.96
	SP-3	5.35	0.0036	0.81	0.44	0.90	0.73	0.83	0.88
	SP-4	6.17	0.0038	0.79	0.41	0.91	0.72	0.88	0.82
	SP-8	8.65	0.0032	0.64	0.38	1.06	0.68	0.89	0.76
	SP-9	9.19	0.0034	0.67	0.37	0.97	0.65	0.88	0.74
	SP-10	9.20	0.0035	0.69	0.41	0.99	0.68	0.83	0.82
	SP-11	9.37	0.0031	0.70	0.39	0.98	0.69	0.88	0.78
	SP-12	11.00	0.0031	0.65	0.33	0.93	0.60	0.92	0.66
	SP-13	11.57	0.0032	0.63	0.36	0.96	0.60	0.84	0.72
Schade (1992) [73]	col 1	15.36	0.0030	0.56	0.36	1.00	0.56	0.78	0.71
	col 2	15.36	0.0034	0.62	0.36	0.97	0.60	0.85	0.71
	col 3	15.36	0.0033	0.60	0.36	0.96	0.58	0.81	0.71
	col 4	15.36	0.0036	0.65	0.37	0.94	0.61	0.83	0.73
	col 5	15.36	0.0035	0.65	0.36	0.92	0.60	0.83	0.72
	col 6	15.36	0.0039	0.67	0.37	0.89	0.60	0.83	0.73
	col 7	15.90	0.0032	0.68	0.35	0.94	0.64	0.91	0.70
	col 8	15.90	0.0032	0.67	0.35	0.94	0.63	0.89	0.70
	col 9	15.90	0.0037	0.70	0.37	0.93	0.65	0.88	0.74
	col 10	15.90	0.0030	0.70	0.36	0.91	0.64	0.89	0.72
	col 11	15.90	0.0032	0.70	0.36	0.91	0.64	0.88	0.72
	col 12	15.90	0.0034	0.65	0.37	0.90	0.59	0.80	0.73
Ibrahim (1994) [74]	V1	10.25	0.0033	0.50	0.26	0.92	0.46	0.87	0.53
	V2	12.00	0.0046	0.64	0.35	0.97	0.62	0.88	0.70
	V4	10.56	0.0035	0.71	0.39	0.90	0.64	0.81	0.79

Table A.3 – Historical PC flexural compression specimen data (cont.)

Source	Specimen ID	f'_c	ϵ_{cu}	k_1	k_2	k_3	k_1k_3	α_1	β_1
Ibrahim (1994) [74]	V5	18.10	0.0040	0.59	0.34	0.92	0.54	0.78	0.69
	V6	14.33	0.0038	0.63	0.37	0.89	0.56	0.75	0.75
	V7	12.28	0.0037	0.67	0.36	0.87	0.58	0.81	0.72
	V5	18.75	0.0040	0.55	0.35	1.00	0.55	0.79	0.69
	V11	18.49	0.0039	0.57	0.35	0.82	0.47	0.68	0.69
	V12	17.56	0.0041	0.58	0.35	0.91	0.53	0.74	0.71
	V13	10.52	0.0037	0.71	0.39	0.87	0.62	0.80	0.78
	V14	18.09	0.0040	0.58	0.34	0.88	0.51	0.74	0.68
	V15	18.10	0.0040	0.57	0.34	0.98	0.56	0.81	0.69
	V16	8.60	0.0036	0.67	0.37	1.08	0.72	0.98	0.74
	V17	18.52	0.0043	0.57	0.36	0.92	0.52	0.74	0.71
	T1	11.75		0.71	0.53	1.01	0.72	0.48	1.06
	T2	12.97		0.70	0.55	1.07	0.75	0.48	1.10
	T3	12.18		0.74	0.55	1.01	0.75	0.50	1.11
	T4	18.72		0.64	0.52	1.09	0.70	0.43	1.03
	T5	18.94		0.64	0.50	0.99	0.63	0.41	1.00
	T6	17.09		0.67	0.53	0.92	0.62	0.38	1.07
Tan et al. (2005) [75]	S40-A-N2	6.74	0.0029		0.40		0.69	0.86	0.80
	S40-A-N3	7.01	0.0029		0.38		0.65	0.86	0.76
	S40-B-N3	7.01	0.0040		0.40		0.76	0.95	0.80
	S40-B-N4	7.11	0.0037		0.39		0.72	0.92	0.78
	S40-B-N5	7.11	0.0033		0.37		0.75	1.01	0.74
	S40-C-N1	6.60	0.0051		0.41		0.83	1.01	0.82
	S40-C-N2	7.01	0.0041		0.40		0.80	1.00	0.80
	S70-A-N	10.36	0.0030		0.38		0.54	0.71	0.76
	S70-B-N1	10.05	0.0041		0.39		0.55	0.71	0.78
	S70-B-N2	11.04	0.0044		0.39		0.59	0.76	0.78
	S70-C-N	10.05	0.0042		0.40		0.58	0.73	0.80
	S90-B-N	12.98	0.0038		0.41		0.57	0.70	0.82
	S90-B-N1	12.98	0.0032		0.36		0.42	0.58	0.72
	S90-B-N2	14.59	0.0031		0.36		0.44	0.61	0.72
	S90-E-N1	13.79	0.0031		0.37		0.49	0.66	0.74
	S90-E-N2	13.40	0.0033		0.37		0.52	0.70	0.74
	S90-E-N3	14.59	0.0030		0.34		0.52	0.76	0.68
	S40-B-E20/2*	7.11	0.0039		0.44		0.84	0.95	0.88
	S40-B-E40/1*	7.11	0.0042		0.37		0.77	1.04	0.74
	S40-B-E40/2*	7.11	0.0039		0.41		0.85	1.04	0.82
S40-B-E60/1*	7.11	0.0037		0.35		0.71	1.01	0.70	

Table A.3 – Historical PC flexural compression specimen data (cont.)

Source	Specimen ID	f'_c	ε_{cu}	k_1	k_2	k_3	k_1k_3	α_1	β_1
Tan et al. (2005) [75]	S40-B-E60/2*	7.11	0.0040		0.41		0.77	0.94	0.82
	S70-B-E20*	11.04	0.0038		0.35		0.55	0.79	0.70
	S70-B-E40*	11.04	0.0037		0.36		0.57	0.79	0.72
	S70-B-E60*	11.04	0.0035		0.39		0.57	0.73	0.78
Mertol et al. (2009) [5]	10EB1	11.00	0.0037	0.65	0.38	1.03	0.67	0.88	0.76
	10EB2	11.40	0.0031	0.62	0.36	1.12	0.69	0.96	0.72
	10EB3	11.70	0.0034	0.65	0.36	1.14	0.74	1.03	0.72
	10EB4	10.40	0.0031	0.64	0.36	1.20	0.77	1.07	0.72
	10EB5	10.90	0.0030	0.62	0.36	1.16	0.72	1.00	0.72
	14EB1	14.60	0.0033	0.63	0.37	1.00	0.63	0.85	0.74
	14EB2	14.30	0.0032	0.60	0.36	1.08	0.65	0.90	0.72
	14EB3	14.70	0.0032	0.61	0.36	1.09	0.66	0.92	0.72
	14EB4	15.00	0.0030	0.58	0.35	1.10	0.64	0.91	0.70
	14EB5	15.40	0.0029	0.57	0.34	1.10	0.63	0.92	0.68
	14EB6	15.20	0.0030	0.60	0.35	1.06	0.64	0.91	0.70
	18EB1	15.80	0.0037	0.69	0.38	0.82	0.57	0.74	0.76
	18EB2	16.00	0.0034	0.67	0.37	0.85	0.57	0.77	0.74
	18EB3	15.60	0.0029	0.63	0.37	0.81	0.51	0.69	0.74
	18EB4	15.80	0.0033	0.65	0.36	0.88	0.57	0.79	0.72
	18EB5	16.00	0.0031	0.65	0.36	0.85	0.55	0.77	0.72
	18EB6	15.50	0.0034	0.66	0.37	0.88	0.58	0.78	0.74
	18EB7	15.00	0.0036	0.64	0.37	1.05	0.67	0.91	0.74
	18EB8	14.50	0.0035	0.65	0.37	1.03	0.67	0.90	0.74
	18EB9	14.90	0.0035	0.62	0.36	1.06	0.66	0.91	0.72
18EB10	14.60	0.0035	0.64	0.38	0.97	0.62	0.82	0.76	

Appendix B: Uniaxial Compression Cylinder Data

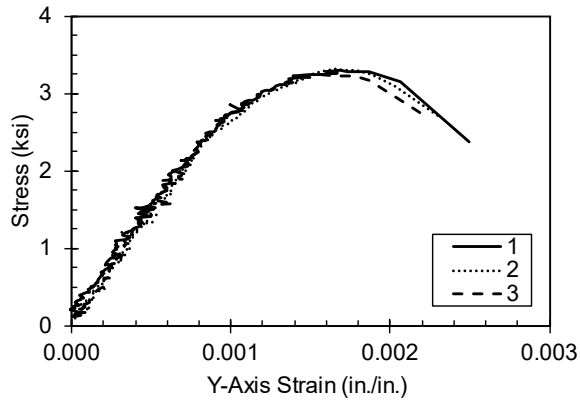


Figure 2.1 – Uniaxial compression strain
0.48 w/c 3 hour BCSA

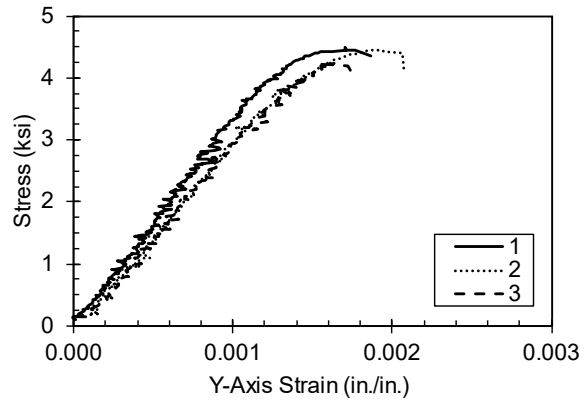


Figure 2.2 – Uniaxial compression strain
0.48 w/c 1 day BCSA

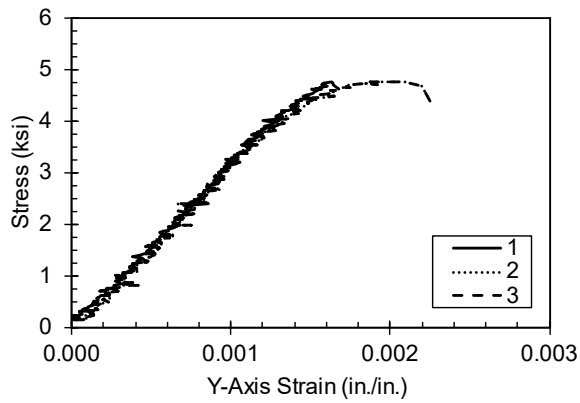


Figure 2.3 – Uniaxial compression strain
0.48 w/c 3 day BCSA

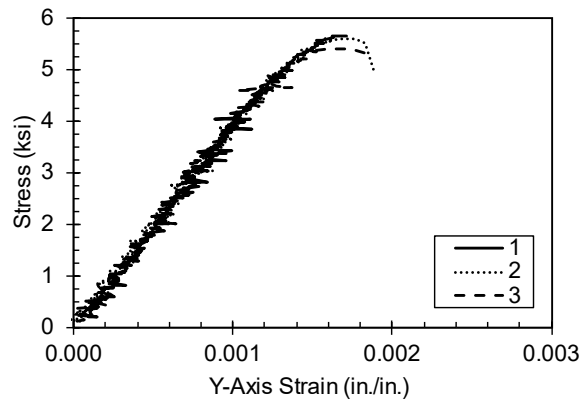


Figure 2.4 – Uniaxial compression strain
0.48 w/c 7 day BCSA

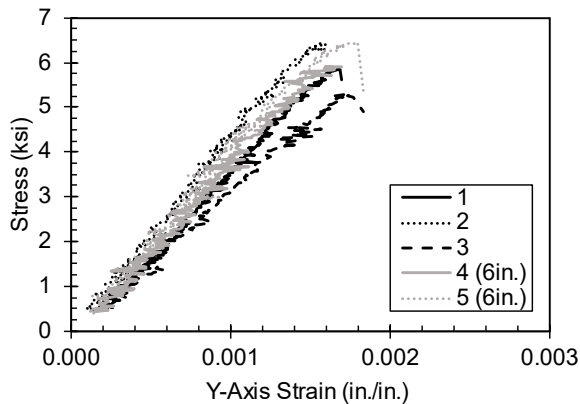


Figure 2.5 – Uniaxial compression strain
0.48 w/c 28 day BCSA

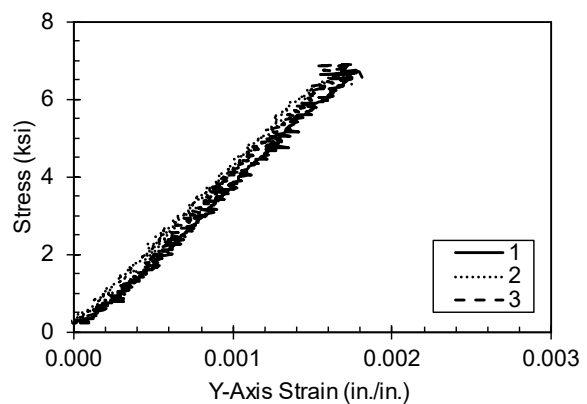


Figure 2.6 – Uniaxial compression strain
0.48 w/c 6 month BCSA

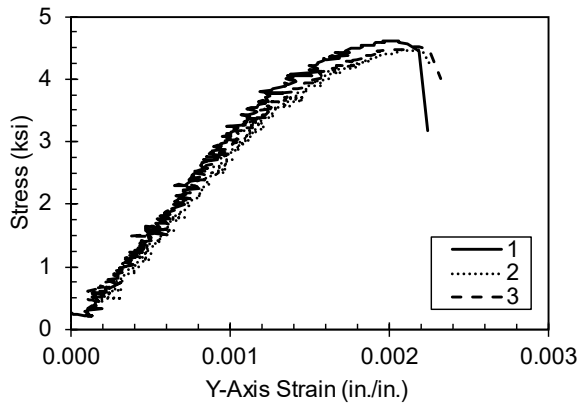


Figure 2.7 – Uniaxial compression strain
0.42 w/c 3 hour BCSA

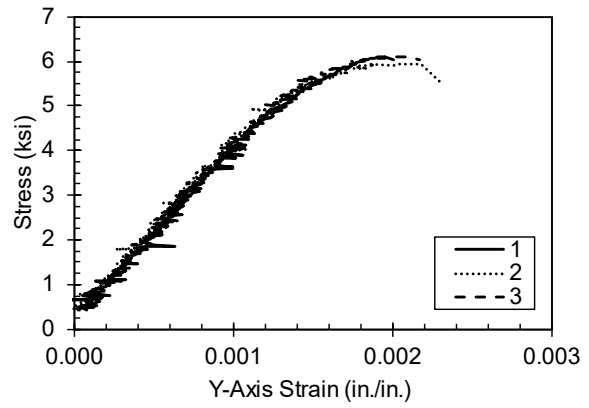


Figure 2.8 – Uniaxial compression strain
0.42 w/c 1 day BCSA

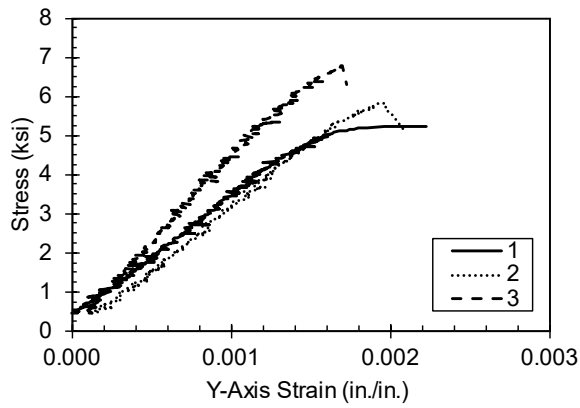


Figure 2.9 – Uniaxial compression strain
0.42 w/c 3 day BCSA

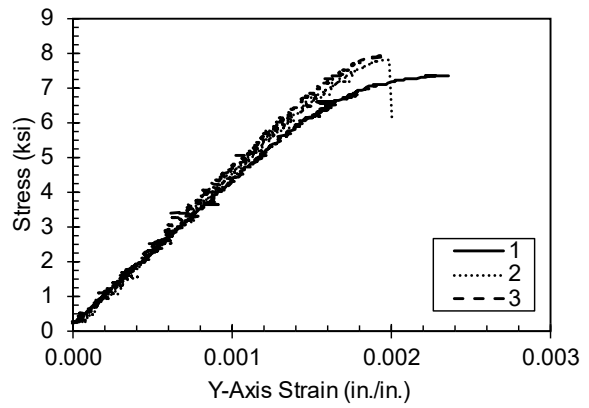


Figure 2.10 – Uniaxial compression strain
0.42 w/c 7 day BCSA

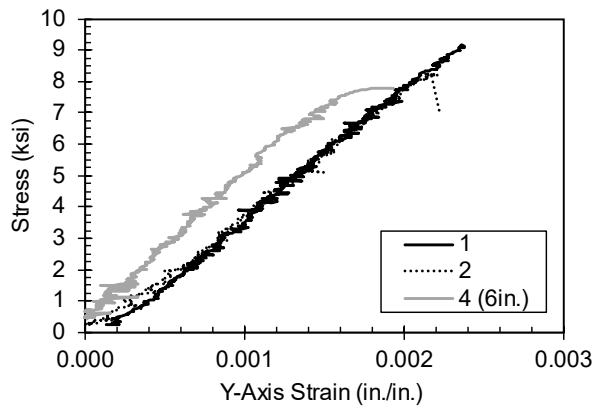


Figure 2.11 – Uniaxial compression strain
0.42 w/c 28 day BCSA

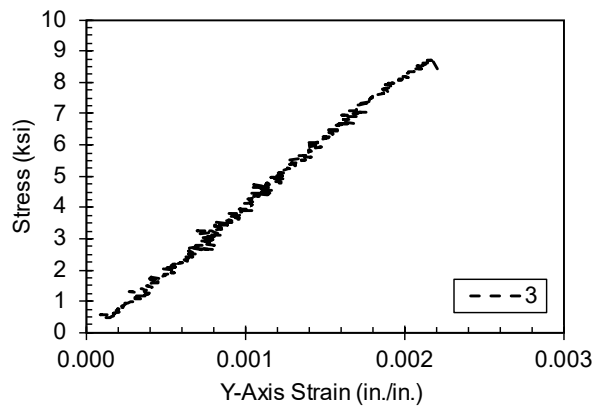


Figure 2.12 – Uniaxial compression strain
0.42 w/c 6 month BCSA

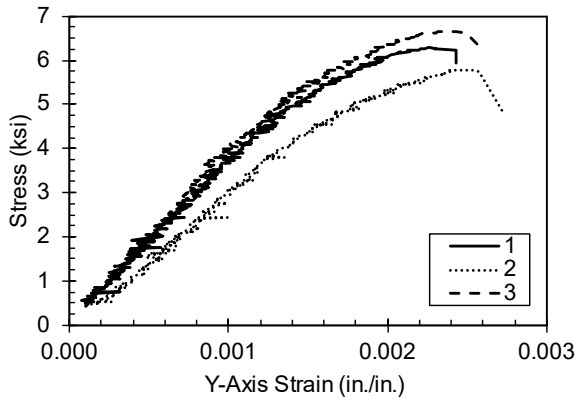


Figure 2.13 – Uniaxial compression strain
0.36 w/c 3 hour BCSA

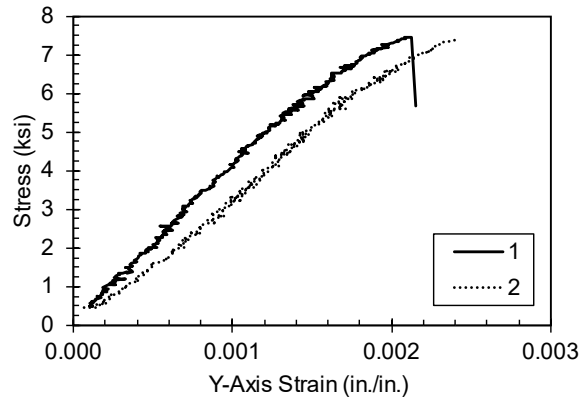


Figure 2.14 – Uniaxial compression strain
0.36 w/c 1 day BCSA

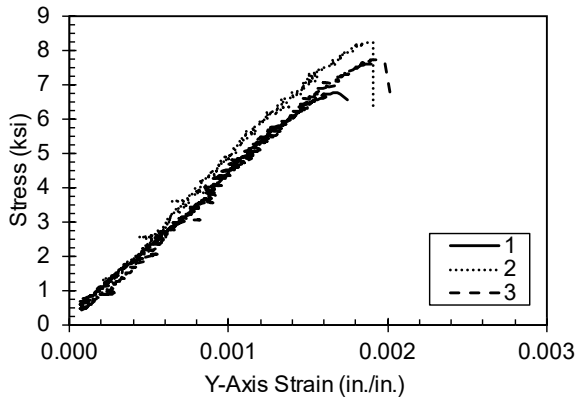


Figure 2.15 – Uniaxial compression strain
0.36 w/c 3 day BCSA

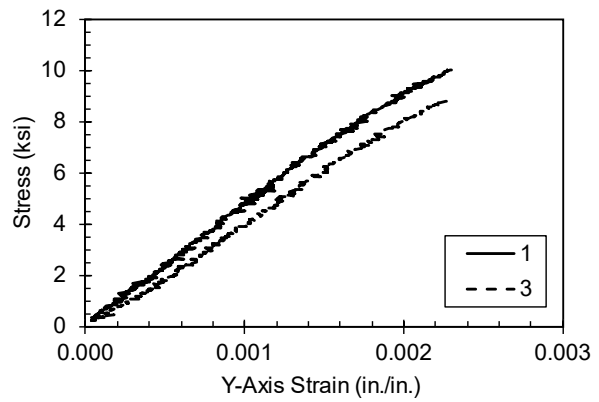


Figure 2.16 – Uniaxial compression strain
0.36 w/c 7 day BCSA

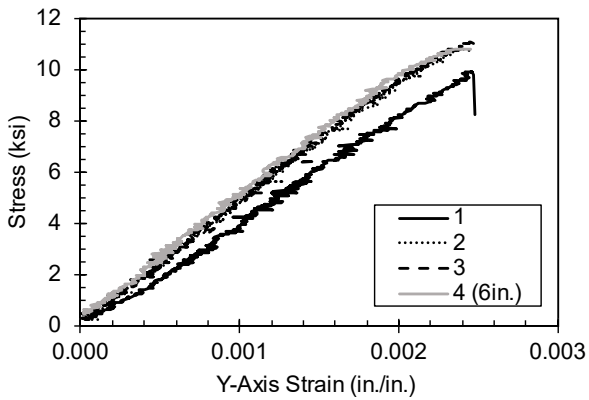


Figure 2.17 – Uniaxial compression strain
0.36 w/c 28 day BCSA

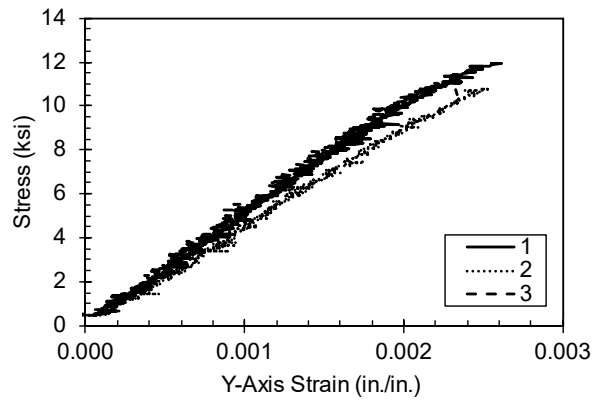


Figure 2.18 – Uniaxial compression strain
0.36 w/c 6 month BCSA

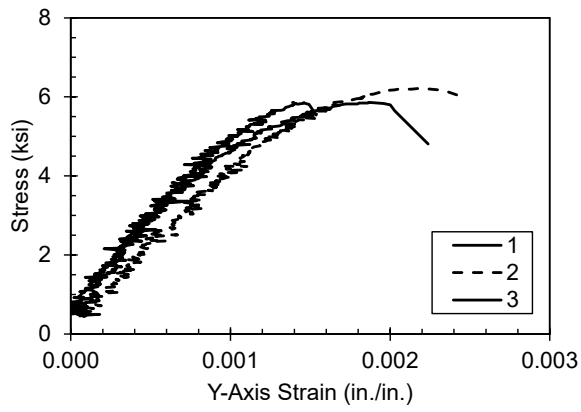


Figure 2.19 – Uniaxial compression strain
0.42 w/c 7 day PC

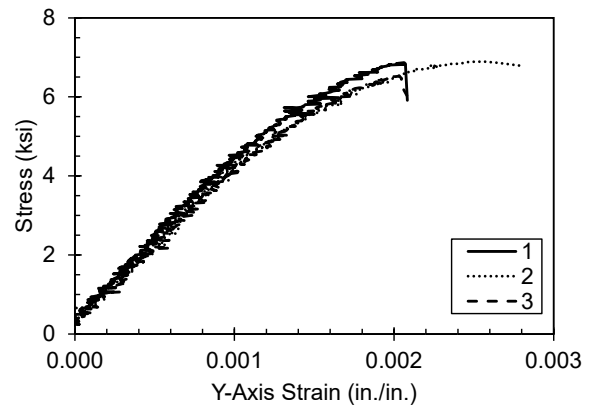


Figure 2.20 – Uniaxial compression strain
0.42 w/c 28 day PC

Table 2.4 – All uniaxial compression cylinder data

w/c	Age	f'_c (psi)	ϵ'_c	E_{ACI} (ksi)	E_c (ksi)	Comments
0.36 BCSA	3 Hour	6296	0.0024	4523	3787	
		5786	0.0027	4336	2812	
		6665	0.0026	4654	3826	
	1 Day	7472	0.0022	4927	3911	
		7385	0.0024	4898	2893	
		7903	-	5067	-	DIC Stopped taking pictures
	3 Day	6778	0.0018	4693	3944	
		8238	0.0019	5174	4631	
		7738	0.0020	5014	4182	
	7 Day	9996	0.0023	5699	4558	
		9702	-	5614	-	DIC Stopped taking pictures
		8843	0.0023	5360	3798	
	28 Day	9931	0.0025	5680	3771	
		10806	0.0024	5925	4803	
		11079	0.0025	6000	4839	
		10801	0.0024	5924	5438	6in. Diameter
	6 Month	11936	0.0026	6227	5099	
		10813	0.0025	5927	4516	
11139		0.0023	6016	5088		
0.42 BCSA	3 Hour	4623	0.0025	3876	2994	
		4471	0.0023	3811	2788	
		4514	0.0023	3830	3013	
	1 Day	6107	0.0020	4454	3458	
		5955	0.0023	4399	3887	
		6098	0.0022	4451	4003	
	3 Day	6101	0.0018	4452	3850	
		5819	0.0021	4348	2838	
		6782	0.0017	4694	4622	
	7 Day	7432	0.0024	4914	4110	
		7872	0.0020	5057	4498	
		7933	0.0020	5077	4490	
	28 Day	9173	0.0025	5459	3757	
		8915	-	5382	-	DIC Stopped taking pictures
		8267	0.0022	5183	3082	
		8745	0.0019	5330	4944	6in. Diameter
	6 Month	9002	-	5408	4240	No good strain data after 6 ksi
		8431	-	5234	3976	No good strain data after 5 ksi
8782		0.0022	5341	3892		

Table 2.1 – All uniaxial compression cylinder data (cont.)

w/c	Age	f'_c (psi)	ϵ'_c	E_{ACI} (ksi)	E_c (ksi)	Comments
0.48 BCSA	3 Hour	3291	0.0025	3270	3160	
		3314	0.0023	3281	3151	
		3249	0.0022	3249	3453	
	1 Day	4488	0.0019	3819	3441	
		4459	0.0021	3806	2944	
		4242	0.0018	3713	3265	
	3 Day	4749	0.0022	3928	2997	
		4776	0.0022	3939	3160	
		4724	0.0022	3918	3242	
	7 Day	5667	0.0017	4291	3905	
		5615	0.0019	4271	3891	
		5402	0.0019	4189	4189	
	28 Day	5857	0.0017	4362	3490	3409 ksi (From MOE Collar)
		6426	0.0016	4569	4411	3696 ksi (From MOE Collar)
		5292	0.0018	4147	3034	3519 ksi (From MOE Collar)
		5931	0.0017	4390	3985	6in. Diameter
		6449	0.0018	4577	4053	6in. Diameter
	6 Month	6736	0.0020	4678	3612	
		6682	0.0018	4659	4047	
		6908	0.0018	4738	3942	
0.42 PC	7 Day	5871	0.0015	4367	4928	
		6219	0.0025	4495	4502	
		5862	0.0022	4364	4339	
	28 Day	6868	0.0021	4724	4474	
		6892	0.0028	4732	3834	
		6927	0.0021	4744	4092	

Appendix C: Uniaxial Compression Cylinder Stress Analysis Code

The code shown below was used to reconcile the difference in sampling rates between the Forney cylinder testing machine and DIC software. This script was written to create uniaxial stress-strain relationships and to calculate MOE. It was written and executed using MATLAB R2017b as a “script program”. Any file that this script needs to access was placed in the same folder with this script to run properly. This can be avoided by inputting the entire read file address and domain into the “Filename” variable definition. The first three comment lines were executed independently in the command window if pathing to the file was broken. The script first cleared all variables, cleared cache, terminated all running instances of Excel, and read an Excel file containing timestamp and raw stress values. The script then calculated the rate of loading of the Forney by isolating a linear portion of the stress-time relationship and estimated a slope using the “polyfit” function. Each timestamp was checked and if a frequency of 0.5s, 1.0s, 1.5s, etc. fell between two timestamps, then a linear interpolation of the two timestamps before and after desired time was calculated and used to modify the stress value. In this way, the stress data was transformed from a non-uniform, nonlinear sample rate to a linear, uniform rate of 2 hertz to match DIC data. All other stress data, not transformed in this way were truncated. Data from DIC is imported from the same previously established Excel file and definitions for low strain (starting strain of MOE calculation), 40% stress value, and ACI318-19 MOE were defined. High strain value for MOE calculation was estimated using expected MOE based on ACI318-19 since a stress-strain relationship was not yet established. Strains within the MOE slope range were smoothed using a running average of 5 points method. This was deemed acceptable because load rate and sample rate can be characterized by a linear relationship. MOE was then calculated using the smoothed strain data and stress data in two ways. First, using the slope between two points method required by ASTM C469. And second, by using the slope of first

degree “polyfit” function approximation. MOE data was plotted visually for verification, and all relevant results are written to a new “.csv” file and output to the desired location.

```
% >> restoredefaultpath
% >> rehash toolboxcache
% >> savepath
clc
clear all
clear var
% system('taskkill /F /IM EXCEL.EXE');

%Recall data files
Filename = 'raw_data_file_name';
x = xlsread(Filename,1,'A4:A20000');
y = xlsread(Filename,1,'C4:C20000')/1000;

%Rate of loading of Forney
xtrim = x(1:int32(floor(0.75 * numel(x))));
ytrim = y(1:int32(floor(0.75 * numel(y))));
LRate = polyfit(xtrim,ytrim,1);
LoadRate = LRate(1);

%Linear Interpolation
freq = 0.5;
stx = round(x(1))+1;

i = 1;
for i = 1:(numel(x)-1)
    %statement to check if frequency index falls between test data
values
    if (stx > x(i))&&(stx <= x(i+1))
        %set new x values as multiples of new frequency
        u(i)=stx;
        %index frequency
        stx = stx+freq;
    else
        u(i)=0;
    end
end

i = 1;
for i = 1:(numel(u))
    if (u(i) > 0)
        %Linear Interpolation for new Y values
        v(i) = (((u(i)-x(i-1)) * (y(i)-y(i-1))) / (x(i)-x(i-1))) + y(i-1));
    else
        v(i)=0;
    end
end
```

```

%Remove all zero values from arrays
xn = nonzeros(u);
yn = nonzeros(v);

%Calculate MOE
xyyraw = xlsread(Filename,1,'R2:R1500')*-1;
%Range for developing modulus
strainlow = .0002;
TMOE = 57*sqrt(max(yn)*1000);
MOEstress = 0.4*max(yn);
strainhigh = MOEstress/TMOE;
%Restricting data to the range

%Smooth xyyraw
i = 1;
for i = 1:(numel(xyyraw))
    if or(i == 1 , i == numel(xyyraw))
        xyysmooth(i) = xyyraw(i);
    elseif or(i == 2 , i == numel(xyyraw)-1)
        xyysmooth(i) = mean(xyyraw(i-1:i+1));
    else
        xyysmooth(i) = mean(xyyraw(i-2:i+2));
    end
end

i = 1;
for i = 1:(numel(xyysmooth))
    if or((xyysmooth(i) < strainlow), (xyysmooth(i) > strainhigh))
        xyyM(i) = 0;
    else
        xyyM(i) = xyysmooth(i);
    end
end
xyyM = nonzeros(xyyM);
i = 1;
for i = 1:(numel(xyyM))
    ynM(i) = yn(i);
end
ynM = ynM';
linM = polyfit(xyyM, ynM, 1);
plot(xyyM, ynM, 'o')
MOE = linM(1);
LRateMOE = (numel(ynM)*LoadRate*freq) / (max(xyyM)-strainlow);

%MOE points to match stress Strain at 40%
fourtystrain = MOEstress/MOE;

%Export Data
newfile = 'desired_output_file_location';
xlswrite(newfile, xn, 'A1:A2000');
xlswrite(newfile, yn, 'B1:B2000');

```

```
xport =  
[TMOE,MOE,LRateMOE, strainlow, strainhigh,MOEstress, fourtystrain]';  
    xlswrite(newfile,xport,'c1:c7');  
%Open Results  
winopen(newfile)  
winopen(Filename)  
% plot(x,y,xn,yn,'o')
```

Appendix D: Flexural Compression Specimen Stress Analysis Code

To account for movements in load P1 and P2 and tension force in the specimen, the MATLAB script listed below used measurement data (P1, P2, LVDT displacements, and strain data) at each timestamp of testing to calculate stresses used in creating a stress-strain relationship model for each specimen. The first seven lines cleared all values, variables, and open instances of excel as previously described in Appendix C. All data recorded from Catman software and DIC were imported and defined. Data from LVDTs and DIC displacements were converted to inches. All geometric calculations were performed using the assumption that if there is a cross sectional view of the middle of the specimen, ϵ_1 (Figure 4.14) is the origin and the max strain face of the specimen falls along the positive y-axis. First the program determined which two faces the neutral axis crosses or if there is no neutral axis. It accomplished this by comparing the interpolated strain values from each corner of the specimen. If two compared strains are of opposite sign, then the script assumed that the neutral axis crosses that face. After it found two crossing points for the neutral axis for each time iteration of data, the slope, y intercept for the neutral axis was calculated. Using DIC y-axis displacement of P1, and LVDT displacements of P1 and P2, load point locations at each timestep iteration were calculated. The script used geometric information about the neutral axis to calculate the perpendicular distance the neutral axis and load points (P1 and P2), max compressive strain, and the max tension strain locations. To calculate tension strain, a tetrahedral stress distribution was assumed and calculated using measured tensile strains correlated with MOE values determined previously in Section 4.1. Using Riemannian geometry's Gram matrix, to find the volume of a tetrahedron, the volume of strain tension was found and multiplied by E_c to find tension stress. Compression stress and tension stress computed from axial and moment forces were performed and exported along with all other relevant calculated data.

```

% >> restoredefaultpath
% >> rehash toolboxcache
% >> savepath
clc
clear all
clear var
% system('taskkill /F /IM EXCEL.EXE');

%Import data from excel file
Filename = 'Filename.xlsx';
%Negative Strain is compression
st1 = xlsread(Filename,1,'A2:A10000'); %Strain 1 (in/in)
st2 = xlsread(Filename,1,'B2:B10000'); %Strain 2 (in/in)
st3 = xlsread(Filename,1,'C2:C10000'); %Strain 3 (in/in)
st4 = xlsread(Filename,1,'D2:D10000'); %Strain 4 (in/in)
LVDT1 = xlsread(Filename,1,'E2:E10000')/25.4; % LVDT 1 (in)
LVDT2 = xlsread(Filename,1,'F2:F10000')/25.4; % LVDT 2 (in)
DICy = xlsread(Filename,1,'G2:G10000')/25.4; % DIC y direction
(in)
P1 = xlsread(Filename,1,'H2:H10000'); % Main ram force (kips)
P2 = xlsread(Filename,1,'I2:I10000'); % Eccentric ram force
(kips)
c = xlsread(Filename,1,'J2'); %absolute measured width of section
(in)
b = xlsread(Filename,1,'K2'); %absolute measured depth of section
(in)
Ec = xlsread(Filename,1,'L2'); %Estimated MOE (ksi)

%NA Intersection Calculations
%All calculations assume strain 1 (st1) is the origin as looking at a
section view of the specimen
i = 1;
for i = 1:(numel(st1))
    %if NA Crosses top and NA side
    if (st2(i)<0)&&(st3(i)>0)&&(st4(i)<0)&&(st1(i)<0)
        NAcross(i) = 1;
        x1(i) = c*(st2(i)/(st2(i)-st3(i)));
        y1(i) = b;
        x2(i) = c;
        y2(i) = b*(st4(i)/(st4(i)-st3(i)));
        At(i) = abs((x1(i)*(b-y2(i))+c*(y2(i)-
y1(i))+x2(i)*(y1(i)-b))/2);
        Ac(i) = c*b-At(i);

        %Tension Force
        Tstress(i) =
Ec*(1/6)*abs(det([x1(i),c,c,x2(i);y1(i),b,b,y2(i);0,0,st3(i)*0.000001
,0;1,1,1,1]));
        T(i) = Tstress(i)*At(i);

        %CG of tension tetrahedron

```

```

        ctx(i) = (1/4)*(x1(i)+x2(i)+c*2);
        cty(i) = (1/4)*(y1(i)+y2(i)+b*2);

%NA Crosses top and bottom
elseif (st2(i)<0)&&(st3(i)>0)&&(st4(i)>0)&&(st1(i)<0)
    NAcross(i) = 2;
    x1(i) = c*(st2(i)/(st2(i)-st3(i)));
    y1(i) = b;
    x2(i) = c*(st1(i)/(st1(i)-st4(i)));
    y2(i) = 0;
    Ac(i) = 0.5*abs(x1(i)*(0-b))+0.5*abs(x2(i)*(0-b));
    At(i) = 0;

    %Tension Force
    Tstress(i) = (1/2)*((c-x1(i))*(st3(i)/2)+(c-
x2(i))*(st4(i)/2))*b;
    T(i) = Tstress(i)*At(i);

    %CG of triangular tension prism
    ctx(i) = (1/6)*(x1(i)+x2(i)+c*4);
    cty(i) = (1/6)*(y1(i)+y2(i)+0*2+b*2);

%NA Crosses NA side and Bottom
elseif (st2(i)<0)&&(st3(i)<0)&&(st4(i)>0)&&(st1(i)<0)
    NAcross(i) = 3;
    x1(i) = c;
    y1(i) = b*(st3(i)/(st4(i)-st3(i)));
    x2(i) = c*(st1(i)/(st1(i)-st4(i)));
    y2(i) = 0;
    At(i) = abs((x1(i)*(0-y2(i))+c*(y2(i)-
y1(i))+x2(i)*(y1(i)-0))/2);
    Ac(i) = c*b-At(i);

    %Tension Force
    Tstress(i) =
Ec*(1/6)*abs(det([x1(i),c,c,x2(i);y1(i),0,0,y2(i);0,0,st4(i)*0.000001
,0;1,1,1,1]));
    T(i) = Tstress(i)*At(i);

    %CG of tension tetrahedron
    ctx(i) = (1/4)*(x1(i)+x2(i)+c+c);
    cty(i) = (1/4)*(y1(i)+y2(i)+b+b);

%No NA (Entire section in compression)
else
    NAcross(i) = 4;
    x1(i) = c*(1-(c/(st2(i)-st3(i))));
    y1(i) = b;
    x2(i) = c*(1-(c/(st1(i)-st4(i))));
    y2(i) = 0;
    Ac(i) = b*c;

```

```

        At(i) = 0;

        %Tension Force
        Tstress(i) = 0;
        T(i) = 0;
        ctx(i) = 0;
        cty(i) = 0;
        ct(i) = 0;
    end

    %slope angle of NA
    slope(i) = (y2(i)-y1(i))/(x2(i)-x1(i));
    yint(i) = -1*(slope(i)*x1(i)-y1(i));
    angleNA(i) = (tan(slope(i))^-1);

    %Location of load P1 and P2 after displacement
    P1x(i) = c/2+((LVDT1(i)+LVDT2(i))/2)); %x movement of P1
    P1y(i) = b/2-DICy(i); %y movement of P1
    P2x(i) = P1x(i)-24; %x Location of P2
    P2y(i) = b/2; %assumes no vertical displacement of P2

    %perpendicular distance of P1, P2, max comp. strain location to
    NA
    a1(i) = (abs(-1*slope(i)*P1x(i)+1*P1y(i)+-1*yint(i)))/sqrt((-
    1*slope(i))^2+1^2);
    a2(i) = (abs(-1*slope(i)*P2x(i)+1*P2y(i)+-1*yint(i)))/sqrt((-
    1*slope(i))^2+1^2);
    cnew(i) = (abs(-1*slope(i)*0+1*0+-1*yint(i)))/sqrt((-
    1*slope(i))^2+1^2);
    ct(i) = (abs(-1*slope(i)*ctx(i)+1*cty(i)+-1*yint(i)))/sqrt((-
    1*slope(i))^2+1^2);

    %Perpendicular distance between max tension strain and NA
    if NAcross(i) == 1
        tstdist(i) = (abs(-1*slope(i)*c+1*b+-1*yint(i)))/sqrt((-
    1*slope(i))^2+1^2);
    elseif NAcross(i) == 2
        if st3(i) > st4(i)
            tstdist(i) = (abs(-1*slope(i)*c+1*b+-1*yint(i)))/sqrt((-
    1*slope(i))^2+1^2);
        else
            tstdist(i) = (abs(-1*slope(i)*c+1*0+-1*yint(i)))/sqrt((-
    1*slope(i))^2+1^2);
        end
    elseif NAcross(i) == 3
        tstdist(i) = (abs(-1*slope(i)*c+1*0+-1*yint(i)))/sqrt((-
    1*slope(i))^2+1^2);
    else
        tstdist(i) = 0;
    end
end

```

```

%fo stress from axial load
foc(i) = (P1(i)+P2(i))/Ac(i);
fot(i) = Tstress(i);

%mo compression stress from moment load
moc(i) = (P1(i)*a1(i)+P2(i)*a2(i))/(Ac(i)*cnew(i));
mot(i) = ((T(i)*ct(i))/(At(i)*tstdist(i)));
end

%Export Data file
newfile = 'output_file_location.xlsx';
%Write headers and export data
headers = ["NAcross", "Slope of NA", "angle of
NA", "Ac", "At", "T", "Tstress", "a1", "a2", "cnew", "tstdist", "foc", "moc", "f
ot", "mot"];
xlswrite(newfile, headers, 'A1:O1');
xport =
[NAcross', slope', angleNA', Ac', At', T', Tstress', a1', a2', cnew', tstdist',
foc', moc', fot', mot'];
xlswrite(newfile, xport, 'A2:O10000');

%Open Results
winopen(newfile)
winopen(Filename)

```

Appendix E: Fabrication Drawings

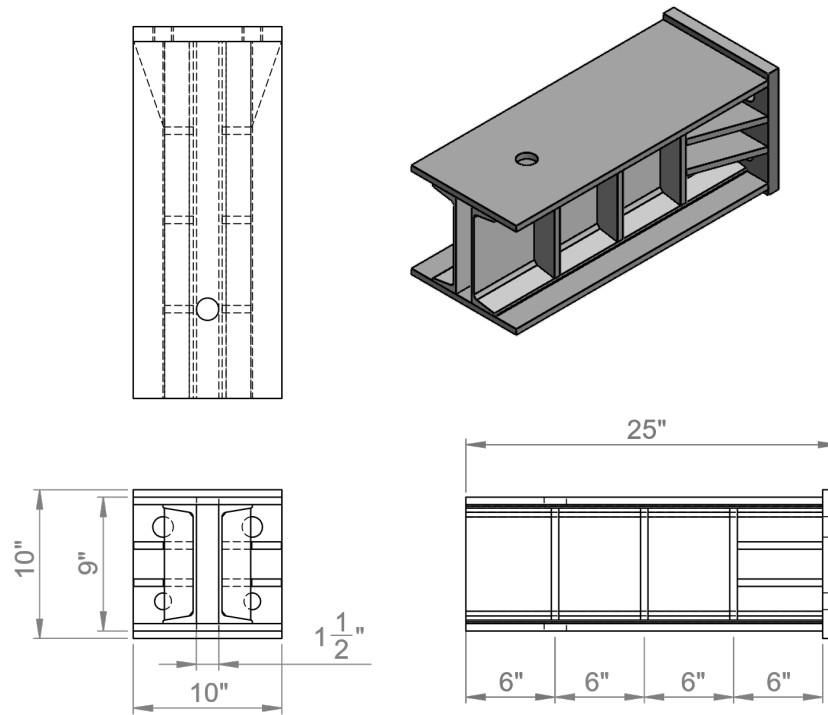


Figure E.21 – Moment arm assembly

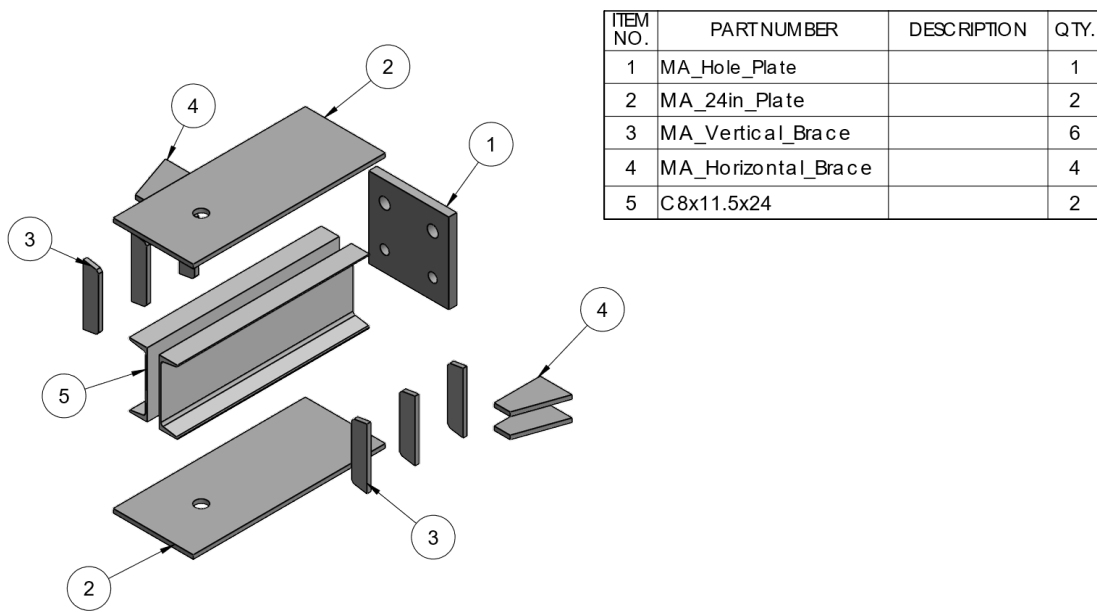


Figure E.22 – Moment arm assembly (exploded)

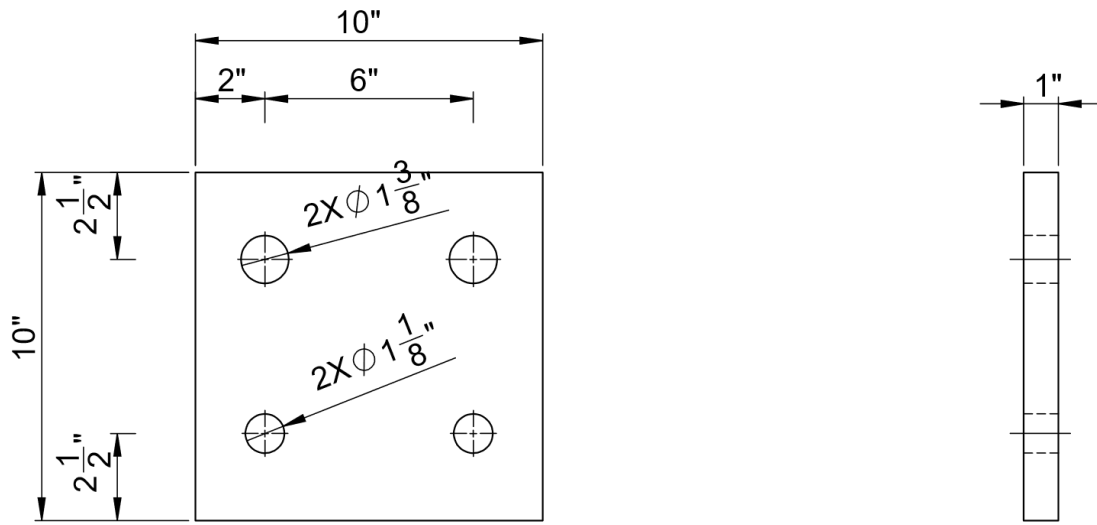


Figure E.23 – Moment arm back plate

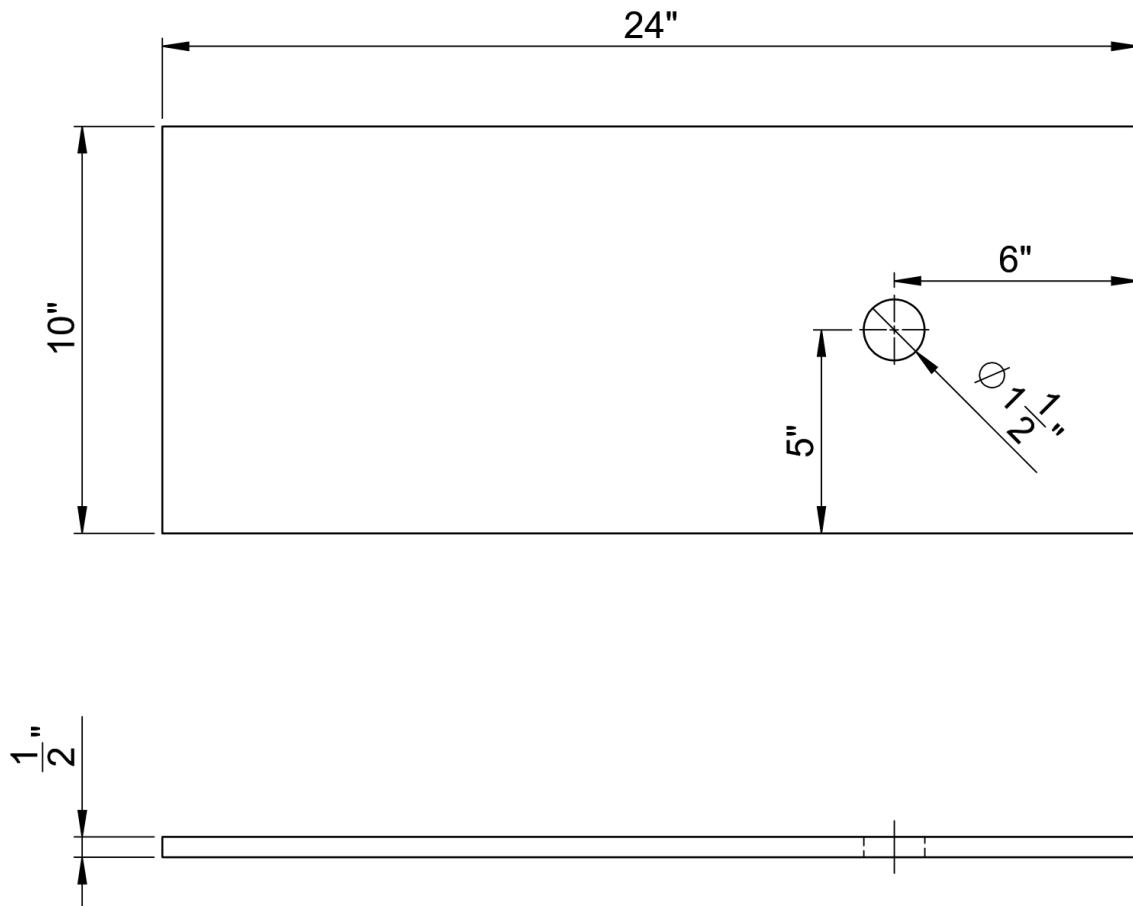


Figure E.24 – Moment arm top and bottom plate

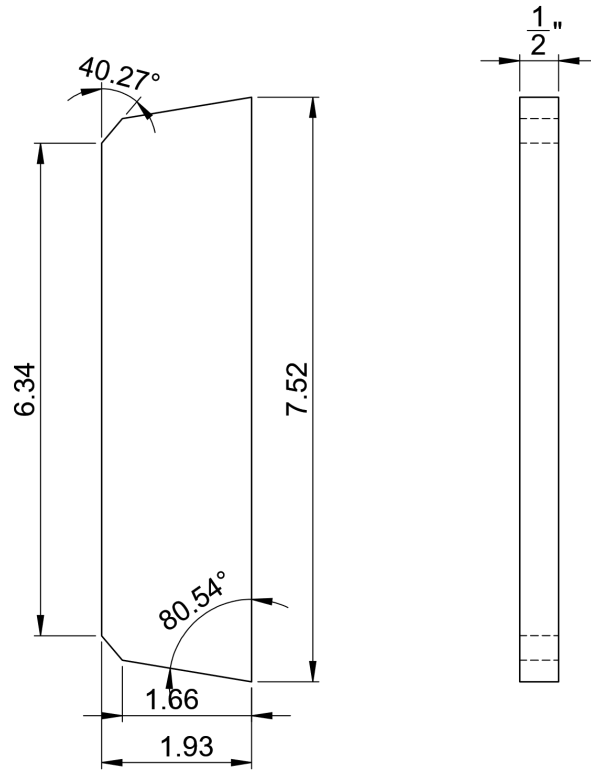


Figure E.25 – Moment arm web stiffeners

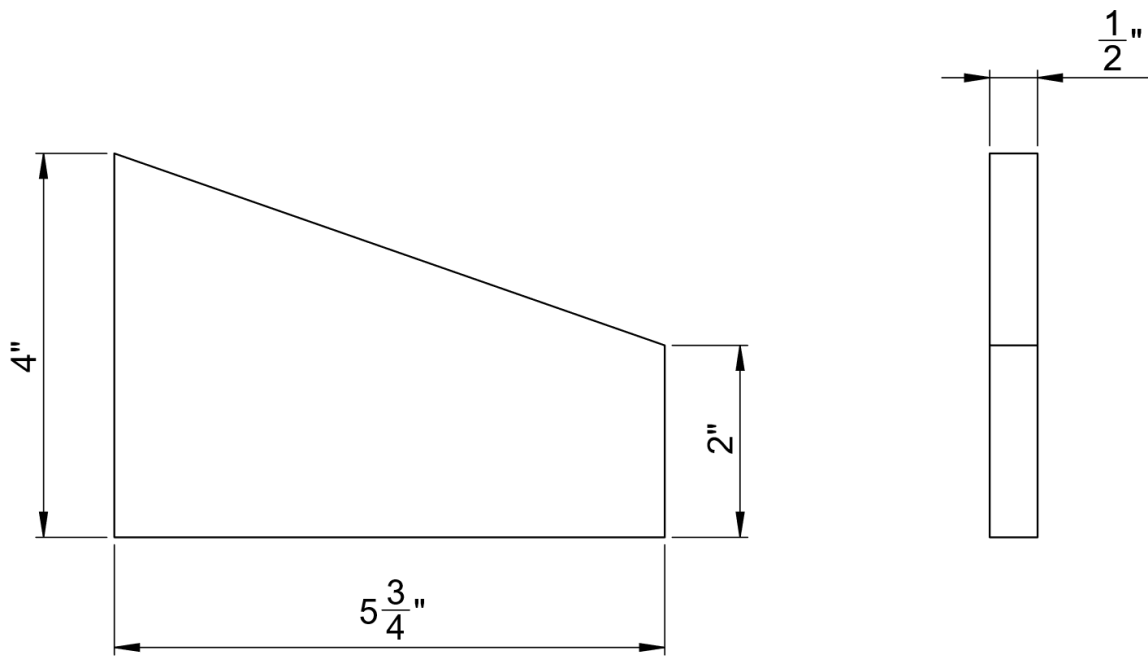


Figure E.26 – Moment arm back plate stiffeners

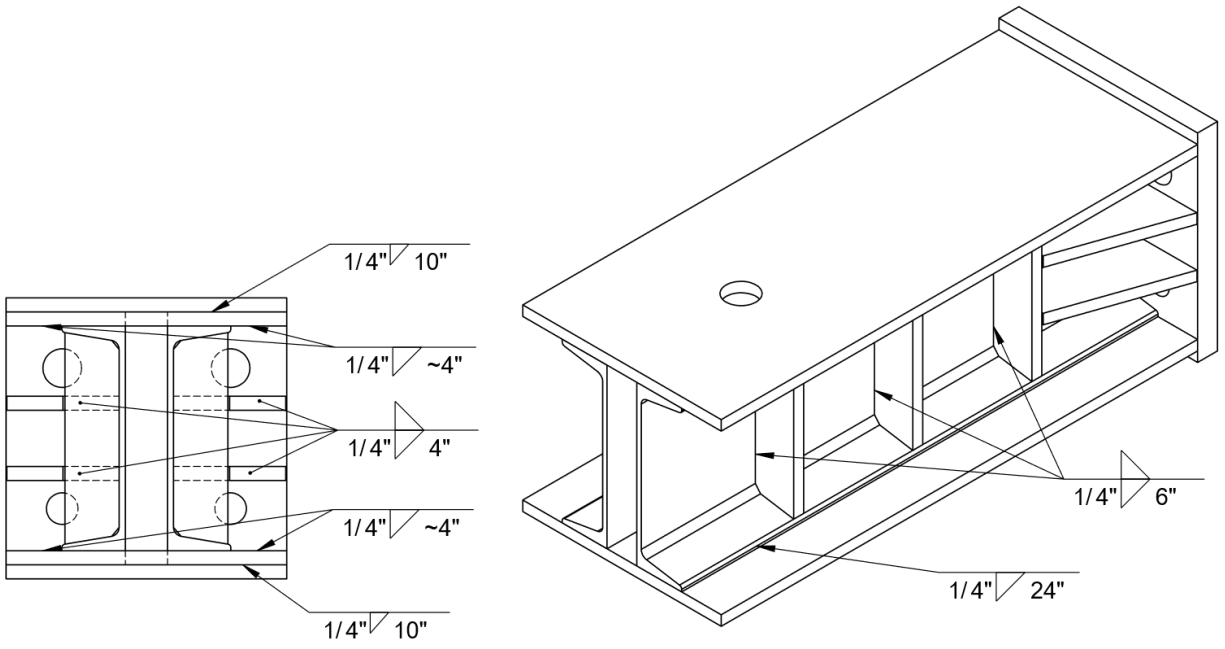
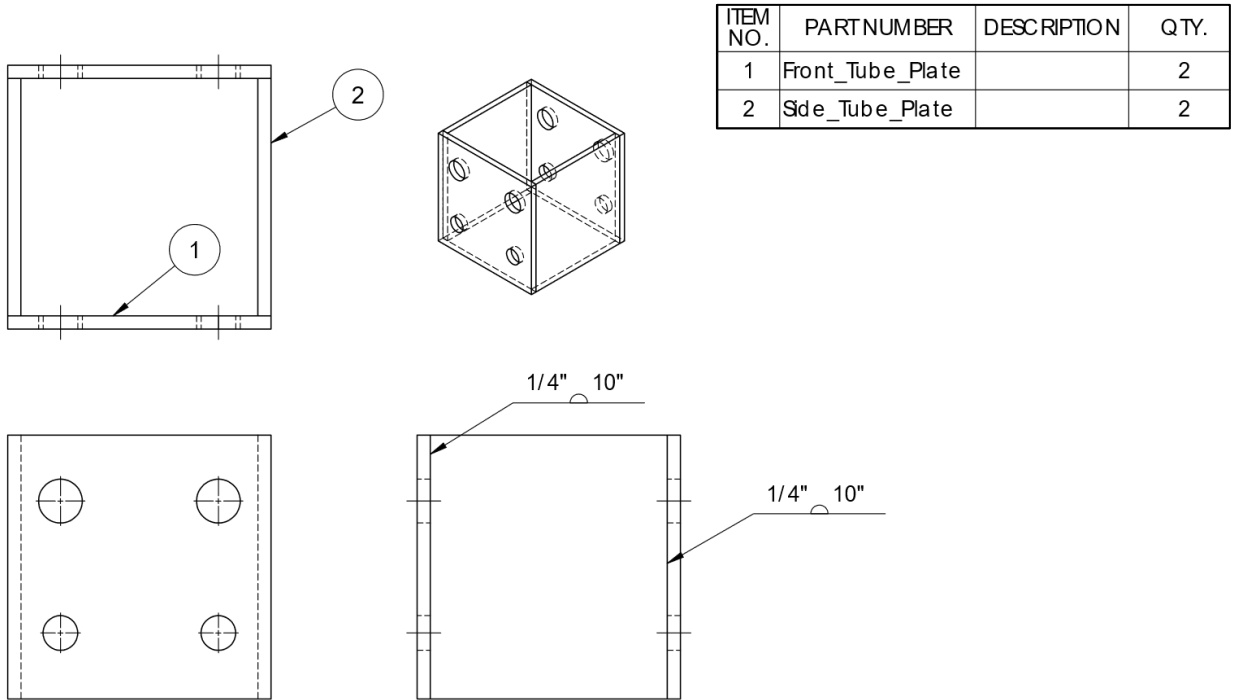


Figure E.27 – Moment arm welding schematics



ITEM NO.	PART NUMBER	DESCRIPTION	QTY.
1	Front_Tube_Plate		2
2	Side_Tube_Plate		2

Figure E.28 – Steel box assembly

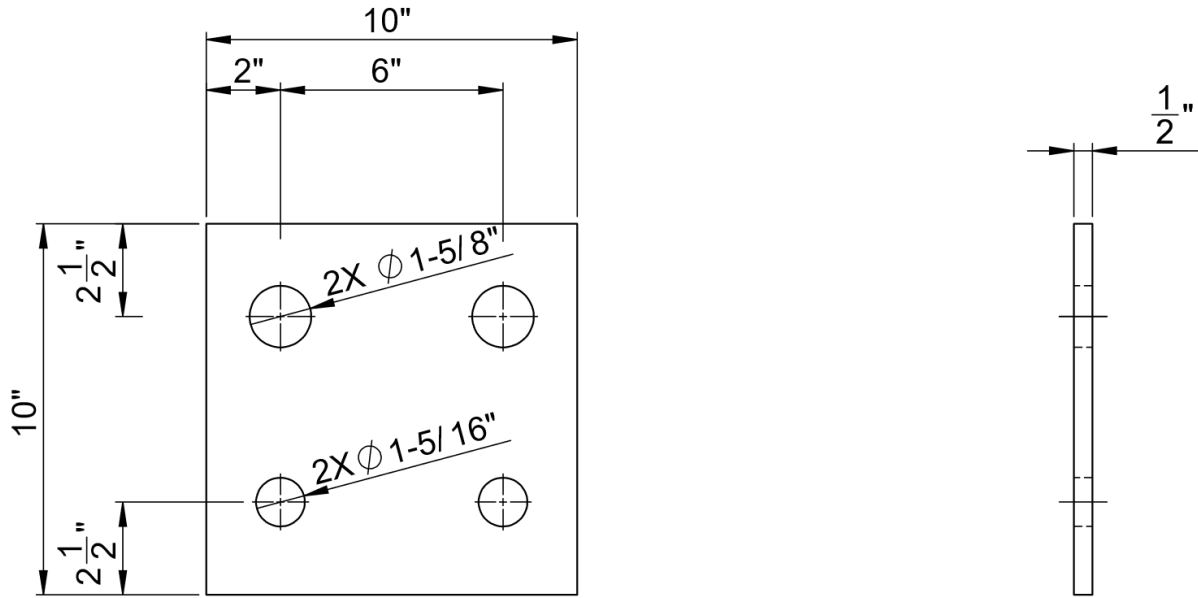


Figure E.29 – Steel box front plate

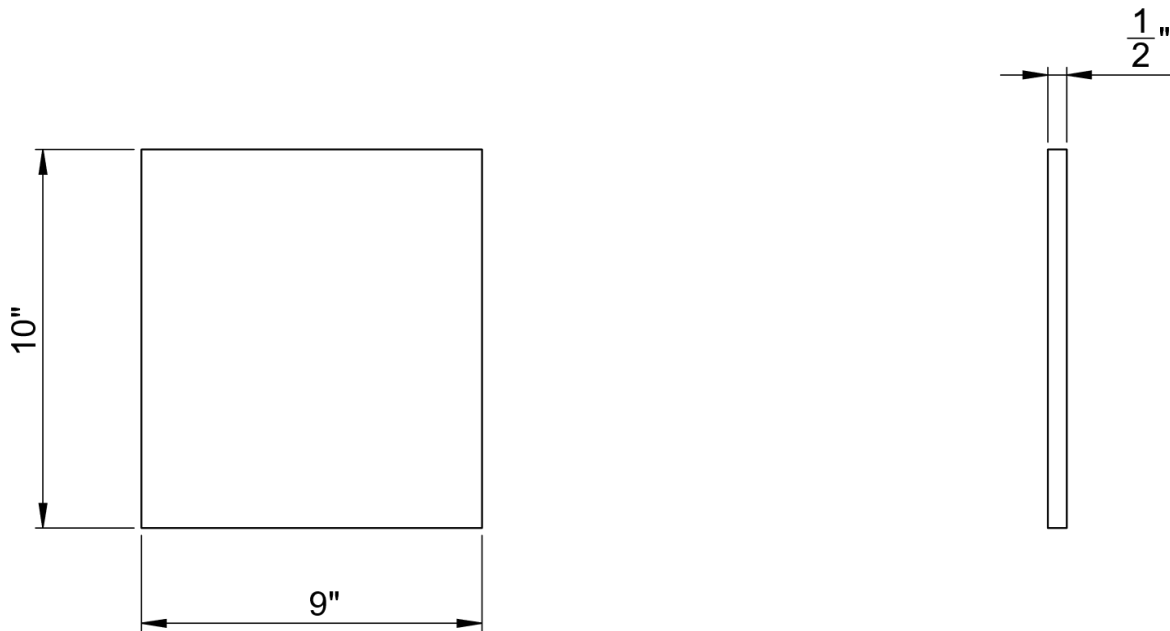


Figure E.30 – Steel box side plate

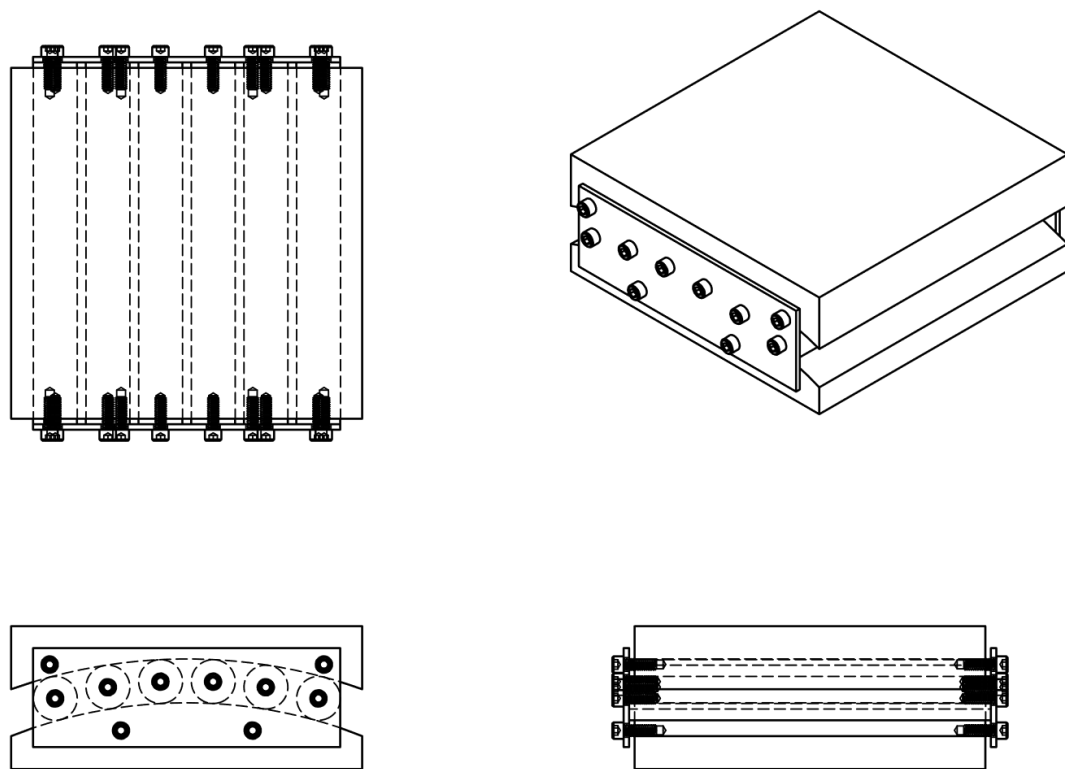


Figure E.31 – Roller assembly

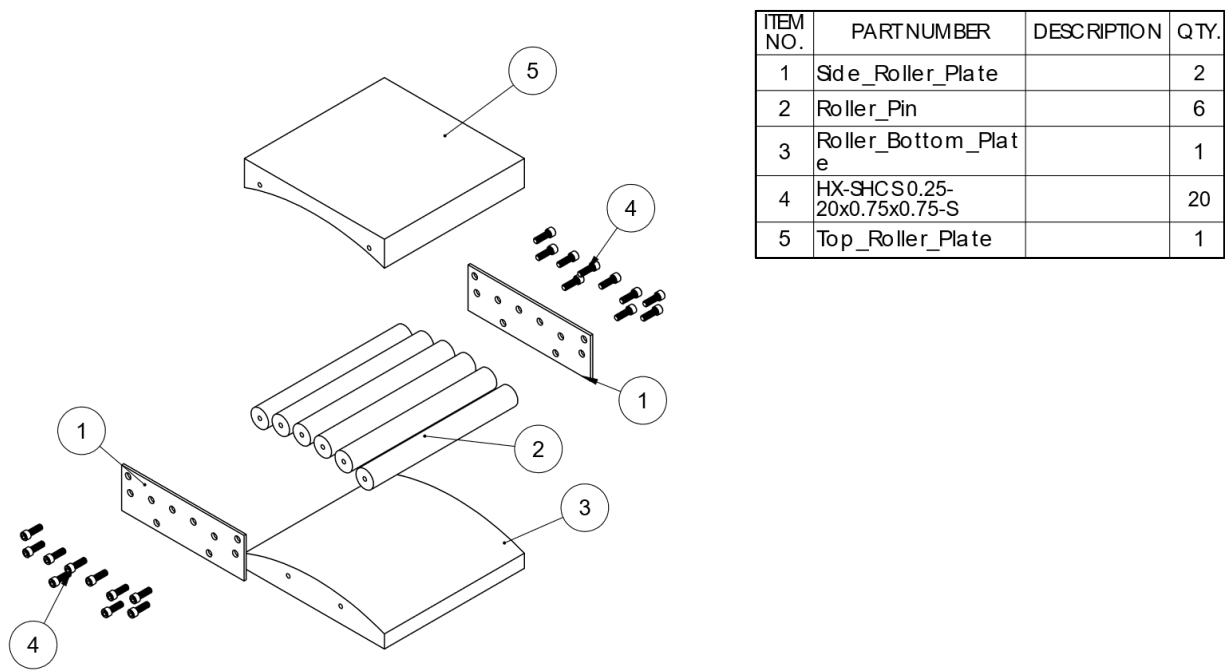


Figure E.32 – Roller assembly (exploded)

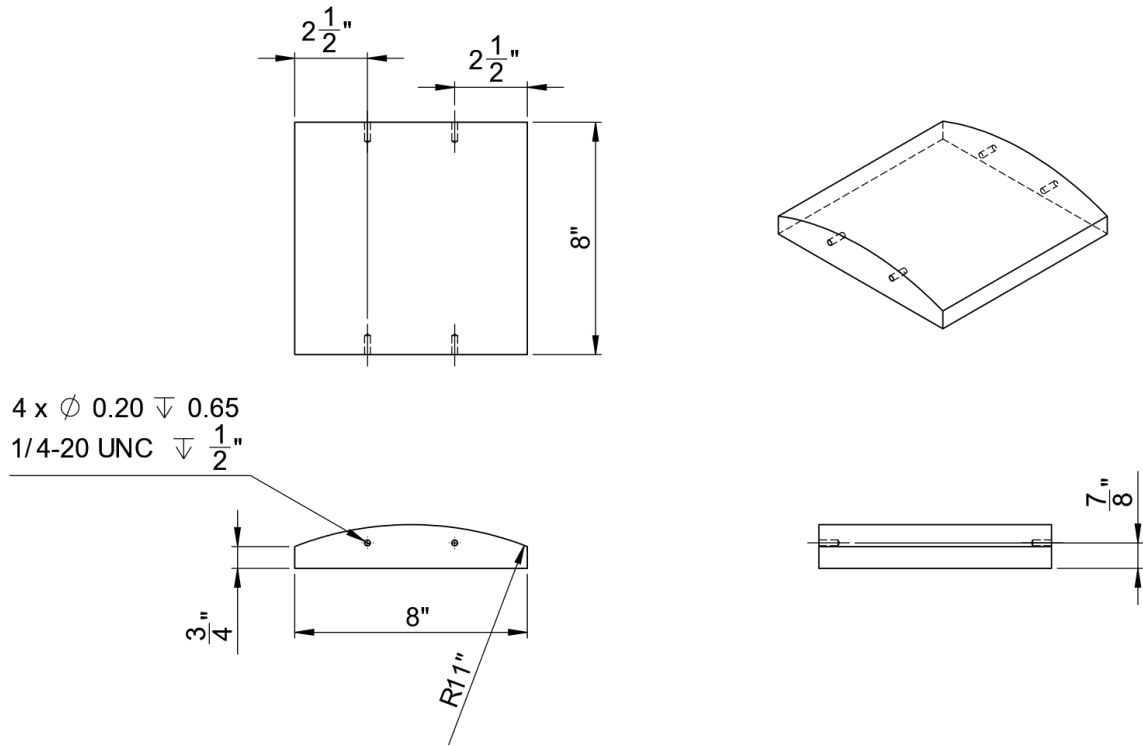


Figure E.33 – Roller top plate

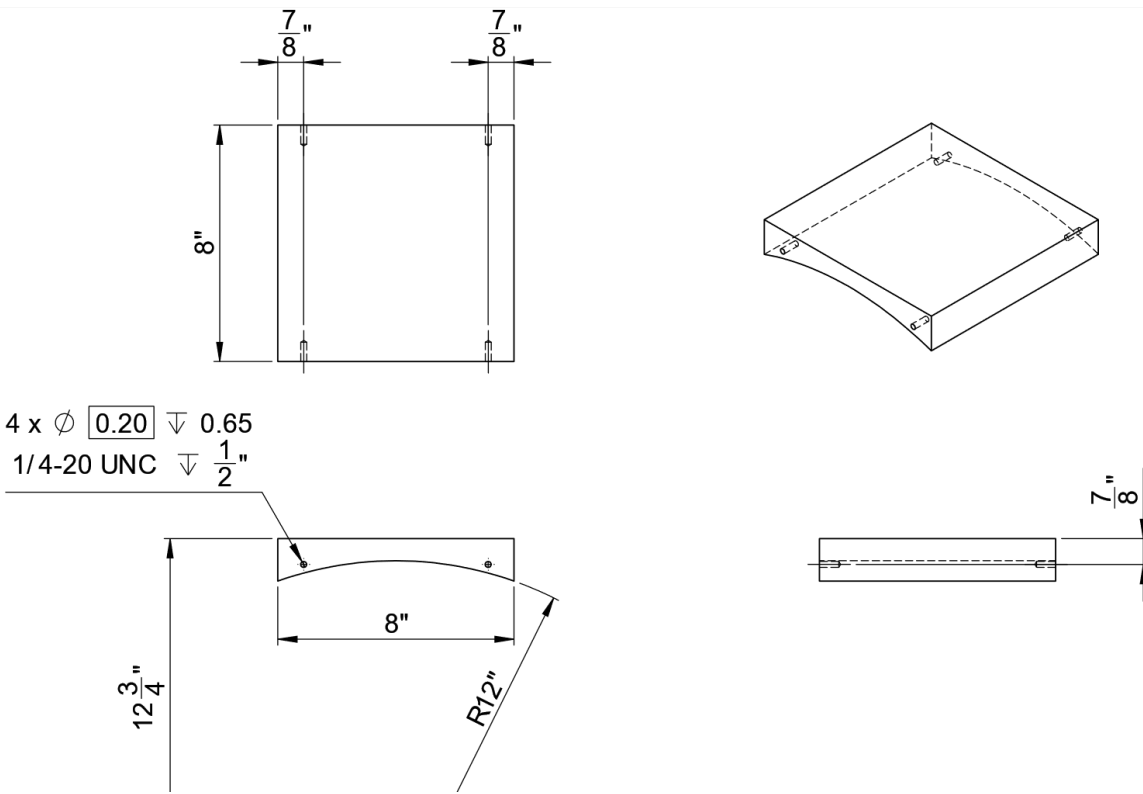


Figure E.34 – Roller bottom plate

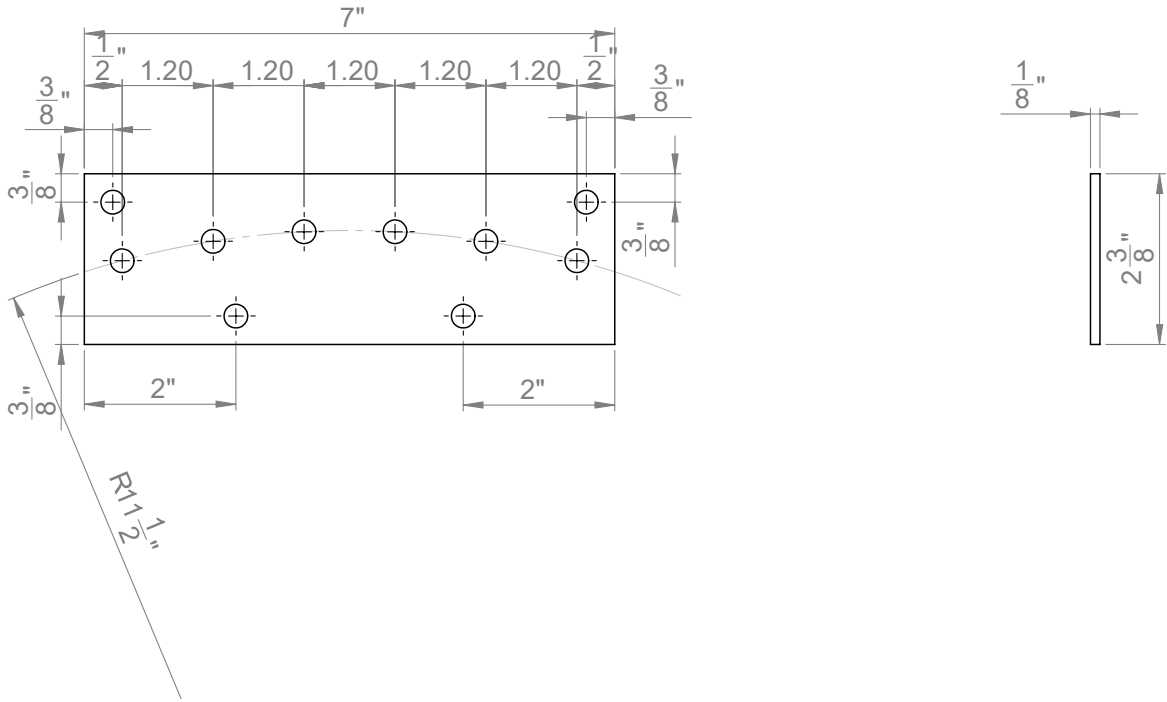


Figure E.35 – Roller side plate

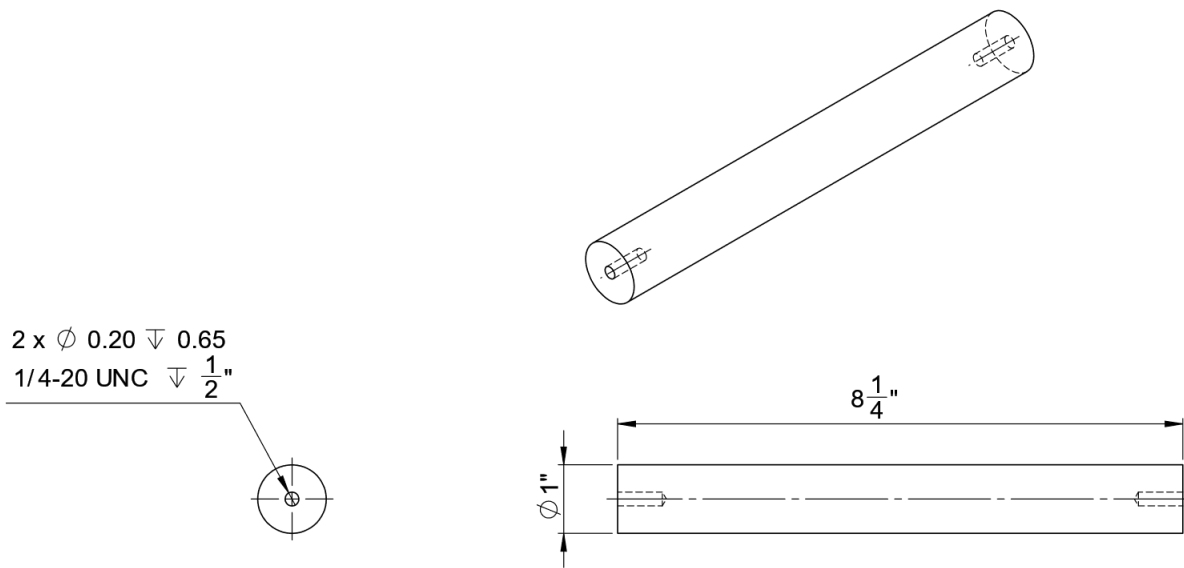


Figure E.36 – Roller pin